

APPLICATION OF COHERENT RADAR USING
STEPPED FREQUENCY MODULATION:
AN EVALUATION OF A PRACTICAL,
NARROWBAND DESIGN

DEAN FRANCIS ROWSELL



APPLICATION OF COHERENT RADAR USING STEPPED FREQUENCY
MODULATION: AN EVALUATION OF A PRACTICAL, NARROWBAND DESIGN

By

© Dean Francis Rowsell, B. Eng, P. Eng.

A thesis submitted to the
School of Graduate Studies
in partial fulfillment of the
requirements for the degree of
Master of Engineering

Faculty of Engineering and Applied Science
Memorial University of Newfoundland

July, 2008

St. John's

Newfoundland

APPLICATION OF COHERENT RADAR USING STEPPED FREQUENCY
MODULATION: AN EVALUATION OF A PRACTICAL, NARROWBAND DESIGN

By

© Dean Francis Rowsell, B. Eng, P. Eng.

A thesis submitted to the
School of Graduate Studies
in partial fulfillment of the
requirements for the degree of
Master of Engineering

Faculty of Engineering and Applied Science
Memorial University of Newfoundland

July, 2008

St. John's

Newfoundland

Abstract

Coherent radar is poised to supersede traditional (typically magnetron-based) radar in a vast array of applications, that until recently could not bear the high cost of coherence. The reason for this is that the wireless communications age has accelerated the development of enabling technologies and tremendously improved associated costs.

Coherent radar systems are capable of equaling or exceeding the performance of traditional radar, at power levels reduced by up to several orders of magnitude. To accomplish this, an equivalent energy is distributed over time using special modulation schemes, such as stepped-frequency-modulation (SFM). SFM is a multi-parameter waveform, so much of the understanding of the effects of different parameter sets can be attained through simulation and investigation of ambiguity responses. Such investigation led to the development of generalized ambiguity patterns for SFM that provide a reference for understanding the impact of changing the waveform parameters. SFM can also be inherently exploited in receiver design since its bandwidth is linearly distributed over time. Therefore, a receiver can be dynamically and synchronously tuned so that instantaneous reception is over a narrow bandwidth—effecting cost savings in the digitizing hardware. An algorithm has been developed, called an *isomorphic matched filter*, to support this method.

To investigate the practical aspects of coherent radar, a research program was launched at C-CORE to design and implement a radar prototype and conduct a field assessment. This research program yielded a working prototype that was subjected to a variety of field exercises. The results showed that the performance, in terms of range and Doppler resolutions, predicted by theory and simulation was indeed realizable, and with a radar platform constructed for moderate cost.

An SFM-based, scanning, coherent radar carries many configuration possibilities. A simple model was developed to consider various parameter sets associated with the SFM waveform and the scanning platform. The model predicts achievable resolutions and range constraints in particular. One interesting finding is that the SFM waveform does not lend itself, simultaneously, to target detection at both short range and long range, and that the signal parameters can only be optimized for one or the other. Operationally, this

implies that if both near range and far range data is needed, strategies must be decided upon to render such data to the user (e.g., alternate the parameter set in successive scans).

While the radar prototype was well-suited to fulfilling the objectives of the research program, it is not in a form suitable for demonstration in real operational scenarios. To accommodate this, the next design iteration must incorporate the following elements: azimuth scanning; a much higher level of integration in the hardware; and, support for real-time processing and rendering of the radar output. This research provides a sound foundation for further development and commercial exploitation of SFM-based coherent radar. It is recommended that such development focus on producing a prototype that can be placed in real operational scenarios in order to fully assess the utility of the technology.

Acknowledgements

The research conducted in support of this thesis would certainly not have been possible were it not for the benefit of having concurrently executed a coherent radar research project at C-CORE. C-CORE not only provided a vehicle for funding this research, but as well, the facilities to support hardware development, software development and field deployment. C-CORE also provided a technical knowledge base to draw upon throughout the development. I am very grateful to have been provided this opportunity.

I would like to thank my co-supervisor, Mr. Desmond Power, who was largely responsible for the initiation of coherent radar research at C-CORE, and whose extensive practical background in radar design and testing was an invaluable aid to my learning process. I would also like to thank my co-supervisors, Dr. Eric Gill and Dr. Charles Randell, for their detailed reviews of my thesis and the guidance and edits they provided. Finally, I would like to thank my colleague, Mr. Stefan Tarrant, who bore the responsibility for S/W development for the prototype coherent radar, and was an indispensable resource in successfully producing the working prototype and executing the field program.

There were several agencies that funded coherent radar research at C-CORE, which I would like to acknowledge as follows: the Regional Citizens' Advisory Council (RCAC) in Valdez, Alaska; the National Search and Rescue Secretariat New Initiative Fund (NIF); the Canadian Coast Guard, Newfoundland and Labrador Region; and the National Research Council Canada Industrial Research Assistance Program (NRC-IRAP).

Last, but most importantly, I would like to thank my family—my wife LoriLynn, and my daughter Lindsey—for their patience and understanding with respect to the time I needed to commit to finishing this work. Certainly, everything I do is in their best interest, and I hope I did my best to keep their needs at the forefront; though, I realize that was not always possible.

Table of Contents

Abstract.....	i
Acknowledgements.....	iii
List of Figures.....	vii
List of Tables.....	xi
List of Examples.....	xii
List of Symbols.....	xiii
1. Introduction.....	1
2. Background.....	5
2.1 Radar Fundamentals.....	5
2.2 Range and Velocity Resolution.....	6
2.3 The Complex Envelope.....	8
2.4 Radar Ambiguity Function.....	12
2.5 Constant Frequency Pulse.....	14
2.6 Linear Frequency Modulation.....	15
2.7 Ambiguity Function Rendering.....	17
2.8 Pulse Compression.....	22
3. Stepped Frequency Modulation.....	29
3.1 SFM Analytical Representations.....	32
3.2 SFM Parameter Sets.....	34
3.3 SFM Ambiguity Response.....	36
3.4 Signal Orthogonality in SFM.....	41
3.5 Practical considerations for SFM.....	49
3.6 Multi-Cycle SFM.....	52
3.7 Sidelobe Reduction in SFM.....	56
3.8 Isomorphic Matched Filter.....	60
3.8.1 Single Pulse Case (Pulsed Radar).....	61
3.8.1.1 Matched Filter.....	62
3.8.1.2 Isomorphic Matched Filter using a Mixer.....	63
3.8.2 Multi-Pulse Case (SFM).....	64

3.8.2.1	Matched Filter	64
3.8.2.2	Isomorphic Matched Filter using a Mixer	67
4.	SFM-Based Radar Design.....	70
4.1	Coherency in Radar Design	70
4.2	Phase Noise Effects on SFM.....	74
4.2.1	Phase Noise Background	74
4.2.2	Phase Noise Simulation	78
4.3	Narrow-Band Coherent Radar Prototype Hardware	84
4.3.1	Clock Reference/Synthesizer	88
4.3.2	Signal Synthesizer.....	90
4.3.3	Transmit/Receive Multiplexer	92
4.3.4	Gate	93
4.3.5	IF Filter	95
4.3.6	Demodulator	97
4.3.7	Digitizer	99
4.3.8	Signal Processor.....	100
4.3.9	Controller	100
4.3.10	Antenna	100
4.4	Processing Algorithms	107
4.4.1	Main Functional Elements	109
4.4.1.1	Doppler Frequency Modification.....	109
4.4.1.2	Complex Envelope Formation	111
4.4.1.3	Correlation	111
4.4.1.4	Bandwidth Recovery.....	111
4.4.1.5	Accumulation.....	111
4.4.2	Implementation	111
5.	Experimental Data	114
5.1	Methodology	114
5.2	Study Areas.....	114
5.2.1	Large Target Site.....	115
5.2.2	Frozen Lake Site	117
5.2.3	Exposed Bay Site	119

5.3	Objectives	121
5.4	Experimental Results	122
5.4.1	Operational Test—Portugal Cove.....	122
5.4.2	Standard Target Assessment—Paddy’s Pond.....	124
5.4.3	Ocean Evaluation.....	132
6.	Considerations for an Operational Coherent Radar	138
6.1	Element of an Operational Radar.....	138
6.1.1	Antenna Scanning.....	138
6.1.2	Integrated Transceiver	140
6.1.3	Real-Time Processing Platform	141
6.2	Analysis of Radar Parameters.....	142
7.	Conclusions and Recommendations	148
	Bibliography	153
	Appendix A: Derivations	155
	Appendix A.1: Correlation function derivation for a simple pulse.	156
	Appendix A.2: Correlation function derivation for pulsed linear FM.	158
	Appendix B: Device Specifications	161
	Appendix B.1: OXCO Specification.....	162
	Appendix B.2: DDS Specification.....	163

List of Figures

Figure 2-1: General Radar Block Diagram.....	6
Figure 2-2: (a) Amplitude spectrum of real signal, $s(t)$. (b) Amplitude spectrum of pre-envelope of $s(t)$. (c) Amplitude spectrum of complex envelope of $s(t)$. (Adapted from [10]).....	11
Figure 2-3: Constant-Frequency Pulsed Waveform	14
Figure 2-4: LFM Waveform	16
Figure 2-5: Surface Uncertainty Diagram for LFM Waveform, $\tau_p=1s$, $\alpha=5$ Hz/s.....	17
Figure 2-6: Contour Uncertainty Diagram for LFM Waveform, $\tau_p=1s$, $\alpha=5$ Hz/s.....	18
Figure 2-7: Contour Ambiguity for LFM Waveform, $\tau_p=1$ s, $\alpha=5$ Hz/s, Threshold=0.5.	19
Figure 2-8: Generalized LFM Contour Ambiguity Diagram (adapted from [16]).....	20
Figure 2-9: Contour Ambiguity for Pulsed Sinusoidal, $\tau_p=1s$, $\alpha=0$ Hz/s, Threshold=0.5	20
Figure 2-10: Uncertainty Function at frequency=0 for LFM Waveform, $\tau_p=1$ s, $\alpha=5$ Hz/s	21
Figure 2-11: Uncertainty Function at time=0 for LFM Waveform, $\tau_p=1$ s, $\alpha=5$ Hz/s	21
Figure 2-12: Uncertainty Function at frequency=0 for LFM Waveform, $\tau_p=1$ s, $\alpha=20$ Hz/s	23
Figure 2-13: Hamming Window.....	25
Figure 2-14: Uncertainty Function at $f=0$ for LFM Waveform, $\tau_p=1$ s, $\alpha=20$ Hz/s	25
Figure 2-15: Uncertainty Function at time=0 for LFM Waveform, $\tau_p=1$ s, $\alpha=20$ Hz/s ...	26
Figure 2-16: 13-bit Barker Coded Sinusoid, $f=10$ Hz.....	27
Figure 2-17: Uncertainty Function at time=0 for 13-bit Barker Coded Sinusoid, $f=10$ Hz	28
Figure 2-18: Uncertainty Surface 13-bit Barker Coded Sinusoid, $f=10$ Hz.....	28
Figure 3-1: Time domain representation of a SFM waveform	30
Figure 3-2: Linear FMCW, FMICW and SFM radar waveforms.....	31
Figure 3-3: Matched Filter Response for SFM with Random and Linear Frequency Assignments, $\tau_p=10$, $B=1$ MHz, $N_p=11$	32
Figure 3-4: LFM Ambiguity Response.....	36
Figure 3-5: FMCW Ambiguity Response.....	37
Figure 3-6: FMICW Ambiguity Response	37

Figure 3-7: SFM Ambiguity Response	38
Figure 3-8: SFM Ambiguity Contour (zoomed).....	38
Figure 3-9: Generalized SFM Contour Ambiguity Diagram	41
Figure 3-10: Response for Parameters $\{N_p=5, T_f=2 \text{ s}\}$	45
Figure 3-11: Response for Parameters $\{N_p=8, T_f=1.25 \text{ s}\}$	45
Figure 3-12: Response for Parameters $\{N_p=10, T_f=1 \text{ s}\}$	46
Figure 3-13: Response for Parameters $\{N_p=12, T_f=0.867 \text{ s}\}$	46
Figure 3-14: Response (zoomed) for Parameters $\{N_p=5, T_f=2 \text{ s}\}$	47
Figure 3-15: Response (zoomed) for Parameters $\{N_p=8, T_f=1.25 \text{ s}\}$	47
Figure 3-16: Response (zoomed) for Parameters $\{N_p=10, T_f=1 \text{ s}\}$	48
Figure 3-17: Response (zoomed) for Parameters $\{N_p=12, T_f=0.867 \text{ s}\}$	48
Figure 3-18: Ambiguity for Practical SFM.....	50
Figure 3-19: Ambiguity for Practical SFM - Zoomed	51
Figure 3-20: Ambiguity Response for Single-Cycle SFM Waveform	53
Figure 3-21: Ambiguity Response for a Two-Cycle SFM Waveform	53
Figure 3-22: Ambiguity a Five-Cycle SFM Waveform.....	54
Figure 3-23: Ambiguity for a Five-Cycle SFM Waveform—Zoomed.....	54
Figure 3-24: Generalized Multi-Cycle SFM Contour Ambiguity Diagram	55
Figure 3-25: 10-Point Hamming Window	57
Figure 3-26: Ambiguity for Practical SFM w/ Hamming Window	57
Figure 3-27: Application of Hamming Window to Multi-Cycle Waveform	58
Figure 3-28: Multi-Cycle Ambiguity with Time Domain Dominant Window.....	59
Figure 3-29: Multi-Cycle Ambiguity with Frequency Domain Dominant Window	60
Figure 3-30: Matched Filter Output for Single Pulse	63
Figure 3-31: $m_s(\tau)$ for $N_p=7, \Delta f=1/\tau_p$	66
Figure 3-32: $m_s(\tau)$ for $N_p=7, \Delta f=\text{arbitrary}$	66
Figure 3-33: $m_s(\tau)$ for $N_p=29, \Delta f=1/\tau_p$	67
Figure 3-34: Mixing Signal.....	67
Figure 4-1: OCXO Phase Noise (© 2008 Greenray Frequency Control Solutions).....	75
Figure 4-2: Computation of Total Phase Noise from Single-Sided PSD.....	77
Figure 4-3: Ambiguity Response for Case 1: $\phi_N=0 \text{ rad}_{\text{RMS}}$	80

Figure 4-4: Phase Ambiguity Response for Case 2: $\phi_N=0.25 \text{ rad}_{\text{RMS}}$	80
Figure 4-5: Phase Ambiguity Response for Case 3: $\phi_N=0.5 \text{ rad}_{\text{RMS}}$	81
Figure 4-6: Ambiguity Response for Case 4: $\phi_N=0.75 \text{ rad}_{\text{RMS}}$	81
Figure 4-7: Matched Filter Response for Case 1: $\phi_N=0 \text{ rad}_{\text{RMS}}$	82
Figure 4-8: Matched Filter Response for Case 2: $\phi_N=0.25 \text{ rad}_{\text{RMS}}$	83
Figure 4-9: Matched Filter Response for Case 3: $\phi_N=0.5 \text{ rad}_{\text{RMS}}$	83
Figure 4-10: Matched Filter Response for Case 4: $\phi_N=0.75 \text{ rad}_{\text{RMS}}$	84
Figure 4-11: Radar Block Diagram.....	86
Figure 4-12: Radar Protoytype Front Panel	87
Figure 4-13: Radar Operational Configuration.....	87
Figure 4-14: Clock Generation Block Diagram.....	90
Figure 4-15: DDS Block Diagram	91
Figure 4-16: 4-Port Circulator Configuration	93
Figure 4-17: Carrier Feed-Through Effects	94
Figure 4-18: Multi-IF-Filter Design.....	97
Figure 4-19: Demodulator Block Diagram (©2006 Analog Devices)	98
Figure 4-20: Slotted Waveguide Antenna.....	101
Figure 4-21: Antenna Radiator	102
Figure 4-22: Field Deployment of Antenna.....	102
Figure 4-23: Antenna VSWR.....	103
Figure 4-24: Antenna Calibration Field Set-up	104
Figure 4-25: Open Field Site (Calibration Antenna in Foreground).....	105
Figure 4-26: Field Site (Antenna and Stepper Motor Configuration).....	105
Figure 4-27: Antenna Calibration Results	106
Figure 4-28: Waveform Transformations	108
Figure 4-29: Core Processing Algorithm Flowchart.....	110
Figure 4-30: Matched Filter Output – Simulated Data (Example 5)	113
Figure 4-31: Matched Filter Output – Real Data (Example 5)	113
Figure 5-1: Lunberg Lens	115
Figure 5-2: Annotated Map of Relative Locations of Field Sites.....	115
Figure 5-3: Antenna Configuration—Portugal Cove Field Site	116

Figure 5-4: Annotated Map of Portugal Cove Field Site.....	116
Figure 5-5: Annotated Map of Paddy's Pond Field Site	117
Figure 5-6: Standard Target (Lunberg Lens) with Tripod Configuration.....	118
Figure 5-7: Radar Shelter and Working Quarters	118
Figure 5-8: Annotated Map of Motion Bay Field Site.....	119
Figure 5-9: ORT Buoy / Lunberg Lens Configuration	120
Figure 5-10: Motion Bay Radar Site.....	121
Figure 5-11: Radar Output for Bell Island and Bell Island Ferry	122
Figure 5-12: Radar Response for Bell Island Ferry (Zoomed)	123
Figure 5-13: Paddy's Pond Data with Various Targets.....	125
Figure 5-14: Paddy's Pond Data with Power Line Structure at Boresight	126
Figure 5-15: Paddy's Pond Data with Power Line Structure outside Boresight	126
Figure 5-16: Lunberg Lens at 575 m, Pulse Width 1 μ s.....	128
Figure 5-17: Range Resolution Illustration (Figure 5-16 Zoomed).....	128
Figure 5-18: Radar Data Showing a Person Standing near Standard Target.....	129
Figure 5-19: Range-Doppler Response for Stationary Target	130
Figure 5-20: Range-Doppler Response for Moving Target (frame 1).....	130
Figure 5-21: Range-Doppler Response for Moving Target (frame 2).....	131
Figure 5-22: Range-Doppler Response for Moving Target (frame 3).....	131
Figure 5-23: Typical Range-Doppler Response for Moored Target.....	133
Figure 5-24: A Second Range-Doppler Response for Moored Target	134
Figure 5-25: Range-Doppler Response with Two Fishing Vessels in Background	135
Figure 5-26: Multi-Cycle Response from Moored Target.....	136
Figure 5-27: Multi-Cycle Response from Moored Target w/ Velocity Error.....	137
Figure 6-1: Commercial Coherent Radar Concept	141

List of Tables

Table 2-1: Comparison between LFM waveforms— $\alpha=5$ and $\alpha=20$	23
Table 3-1: SFM Signal Design Considerations	35
Table 4-1: Tabularized One-Sided Phase Noise PSD Corresponding to Figure 4-1	75
Table 4-2: Parameters and Results for Phase Noise Scenarios.....	79
Table 4-3: Radar Prototype Signal Specifications.....	88
Table 4-4: Antenna Specifications.....	106
Table 6-1: SFM Parameter Spreadsheet	145

List of Examples

Example 1: LFM, FMCW, FMICW and SFM Comparison.....	36
Example 2: Orthogonality in SFM Waveforms	43
Example 3: Realistic Signal Parameters for SFM.....	50
Example 4: Orthogonality in SFM Waveforms	52
Example 5: Simulated and Real Data Comparison.....	112

List of Symbols

α	Quadratic phase constant or chirp rate
ψ_a	Antenna scan rate
τ_b	Baseline pulse width
Δf	Frequency step
Δf_d	Doppler frequency resolution
ϕ_n	Phase offset of n^{th} pulse
τ_p	Pulse width
Δr	Range resolution
Δt	Temporal resolution
Δv	Velocity resolution
B	Bandwidth
c	Speed of light
E	Energy
F	Improvement factor
f_c	Carrier frequency
G_p	Processing gain
N_c	Number waveform cycles per complete waveform
N_p	Number of pulses per waveform cycle
N_T	Number of pulses per complete waveform
P_b	Baseline Peak Power
P_o	Output Power
prf	Pulse repetition frequency
R_{blank}	Blanking range
R_{max}	Maximum range
T_c	Cycle period
T_f	Pulse repetition period

T_{il}	Illumination time
T_s	Signal duration
v_r	Target radial velocity
Λ	Triangle function
λ	Wavelength

1. Introduction

Radio detection and ranging, or *radar*, has been in widespread use for well over one-half of a century. Advancements in radar were kick-started in the 1930's by preparations for the Second World War. Most equipment produced during this age was limited to VHF and UHF frequencies below 1 GHz. But the need for greater bandwidths to achieve higher resolution necessitated a shift into microwave frequencies (above 1 GHz). One of the significant early challenges in the evolution of microwave radar was the difficulty in efficiently transmitting large amounts of power, owing to the limitations of tube and solid-state electronics at microwave frequencies. One of the first solutions to this problem was the magnetron, which allowed engineers to build compact, yet high power, mobile radar sets. During the 1940's and 1950's, the area of coherent system operation and Doppler signal processing saw many significant advances [1]. Coherency enables enhanced processing of radar returns to resolve both target range and target velocity with fine detail. The magnetron is not a frequency stable device and exhibits a random pulse-to-pulse starting phase. To achieve coherency in a magnetron-based design additional circuitry was employed to track the frequency and phase of each outgoing pulse—but with limited accuracy. So another technology—the klystron tube amplifier—became widely adopted in coherent radar design.

The klystron tube belongs to the category of microwave amplifiers that amplify a highly stable low-power reference signal to produce a correspondingly stable high-power output. The klystron produces, as an output, an electromagnetic wave, that is sent through a waveguide to the antenna aperture; this may not be physically or mechanically suitable for many applications. More recently, the traveling-wave tube amplifier (TWTA), which produces an electrical output to a coaxial feed, has gained acceptance in coherent designs as it can yield tens of kilowatts of power, over an octave in bandwidth, up to frequencies of 50GHz. However, the solid-state amplifier is by far the best for maintaining gain flatness and phase linearity—unfortunately it has not evolved to the point where it can compete with the TWTA for applications requiring significant power at high frequencies. In time, the solid-state amplifiers will chip away at the TWTA's dominance as the most cost-effective source of microwave power for high-frequency

high-power applications [2]. But currently, other means must be employed to economically produce high performance coherent radar.

The major advantage of the amplifier type of transmitter is its inherent stability and linearity, which allows for the exploitation of *pulse compression* [1]. In pulse compression radar, a relatively long pulse is transmitted, while the receiver, utilizing knowledge of the transmitted frequency and phase, reduces the response width and increases the signal-to-noise ratio (SNR) of the uncompressed response of a scatterer [3]. The appeal of pulse compression is found in spreading energy over a longer duration, and significantly relaxing the output power requirements of the transmitter, thereby allowing the designer to exploit low-power amplifiers, such as solid-state, without compromising performance. The performance of coherent radar is affected by amplitude and phase contamination in the system [4]; the inherent linearity associated with solid-state amplifiers minimizes these contaminants.

Currently, coherent radar finds its place mostly in very expensive scientific or military applications. For example synthetic aperture radar (SAR) strongly relies upon coherency to achieve high resolution (< 1 metre) from satellite-borne radar orbiting the earth. Expensive high-power amplifiers can be afforded in such applications, but pulse compression is still a necessity in order to recover the weak signals scattered from the earth from large distances. Other examples of scientific coherent radar are: the IPIX X-band radar, described by Haykin [5], for studying the ocean environment; and, a 150MHz coherent radar system, described by Moore [6], for sounding the Antarctic ice cap. However, commercial exploitation of coherent radar is virtually non-existent, owing to the associated high non-recurring engineering and production costs.

The evolution of coherent radar has faced challenges other than those associated with the power amplifier. Pulse compression theory has been well-established for decades, but the processing power has evolved more slowly. The wireless revolution has brought about several technological advances that enable the realization of economical commercial coherent radar, including:

1. Digital Signal Processors (DSP): The real-time processing power available through DSP hardware is perhaps the most significant advance. Pulse

compression is a mathematically intensive process, so cheap processing power is very beneficial.

2. **Microwave Devices:** Microwave devices have improved greatly over the past decade. Factors that would have otherwise introduced contaminants into the system have been minimized. For example, only recently has the application of I/Q modulators been practical due the precision with which the signal and local oscillator inputs can be balanced, which serves to reduce unwanted mixer products to suitable levels.
3. **Direct Digital Synthesizers (DDS):** DDSs generate fully synthesized, digitally controlled output signals with precise control of frequency, phase, and amplitude, and maintains coherence while changing these parameters [3]. By driving the DDS with a highly stable oscillator, these parameters can be controlled with great precision, since they are digitally derived. DDS technology also provides incredible flexibility that can allow an easy re-configuration of signals generated by the radar.

The widespread adoption of the above technologies in wireless applications has brought about significant economies of scale that can be exploited by designers to develop low-cost coherent radar, which is the motivation for this thesis. The research was supported by a project involving the design and construction of a coherent radar prototype, by the author, at C-CORE. The coherent radar prototype was built both to investigate the practicality of constructing low-cost coherent radar and to investigate the application of coherent radar to real detection problems with slow-moving ocean targets.

This thesis first explores the foundations on which the coherent radar prototype is based, through a review of relevant literature and theory. Next, stepped frequency modulation (SFM) is given considerable treatment so as to justify the choice of this modulation scheme for the prototype. In particular, a considerable original analysis of ambiguity responses associated various SFM waveforms is presented, and generalizations are derived in graphical format as a tool for waveform design. Achieving wide-band performance with SFM from narrow-band hardware, through a method devised by the author called *isomorphic matched filtering*, is given particular focus. The design and

construction of the narrow-band coherent SFM radar is then presented. Since coherency is intimately dependant on good control over signal phase, a brief study of the effects of phase noise on SFM-based coherent detection is presented. This is followed by descriptions of the hardware design and signal processing algorithms. Finally, results from real experimental data acquired from the coherent radar prototype are presented and compared with the theoretical performance estimates. Conclusions drawn from this research highlight the advantages and challenges associated with the commercialization of coherent radar, and summarize the constraints that must be fully understood to adopt coherent radar in practical applications. These constraints are quite different from those of conventional non-coherent radar.

To narrow the scope, this thesis explores only the theoretical foundation and design of the coherent radar prototype, and does not address the propagation effects and target characteristics that affect or manipulate the backscatter in a real environment, except where such factors play a role in the design of the radar itself. The thesis captures elements from both the associated research project executed by the author at C-CORE and additional research and simulation carried out during and following completion of this project targeted specifically for this thesis that were not within the scope of the research project, but critical for future development and commercialization efforts. Accordingly, this thesis is intended as a single reference in which future development can be rooted.

2. Background

To completely understand the radar design developed in this thesis a number of fundamentals need to be understood. The background material presented in this section begins with general radar fundamentals, followed by an introduction to pulse compression. Wide-band techniques that provide pulse compression are presented next, with SFM explored in detail. The ambiguity response of SFM waveforms are then investigated, along with techniques for improving the ambiguity response. Finally, a method is proposed for implementing the ambiguity function on data acquired from a narrow-band radar architecture.

2.1 Radar Fundamentals

The basic form of a radar comprises a radio transmitter and receiver pair, whereby the transmitter, through an antenna, emits electromagnetic energy in the form of a signal, $s(t)$, that propagates through some channel (usually the atmosphere) and is reflected by physical objects, or *targets*. The receiver, through either a common or separate antenna, senses the presence of reflected waves, $r(t)$, from which the radar can determine the existence of the targets [7]. A general block diagram of a radar is shown in Figure 2-1, where the range to a single target is given as R . In this case, a common antenna is used for transmit and receive, multiplexed through a duplexer. The transmitter and receiver are normally synchronized through a controller, and a processing unit is required to interpret the signals detected by the receiver. The general form of a radar does not differ between non-coherent and coherent systems; while there is a significant difference in the detailed design, all radars obey certain fundamentals.

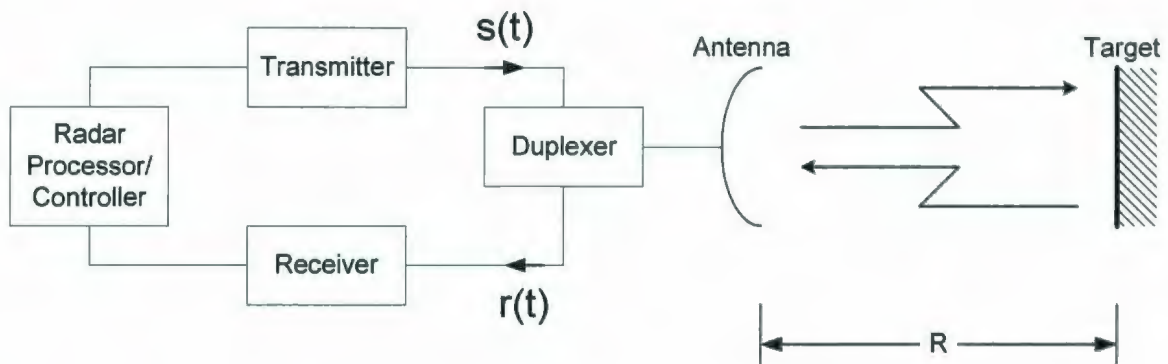


Figure 2-1: General Radar Block Diagram

2.2 Range and Velocity Resolution

Two parameters of particular interest in radar applications are range resolution and velocity (or Doppler) resolution. Range resolution refers to the closeness to which two targets can be distinguished in range while instantaneously traveling at the same radial velocity with respect to the radar. Velocity resolution refers to the closeness to which two targets can be distinguished by velocity while instantaneously occupying the same radial position with respect to the radar. One of the motivations for the development of coherent radar is the achievement of high range and velocity resolutions. This not only provides differentiation of targets, but enhances the ability to identify targets in the presence of clutter. For example, sea clutter exhibits a velocity or Doppler profile due to Bragg scattering, whereby the frequency of the peak in the Doppler spectrum is consistent with phase velocity of the waves resonant with the radar frequency [8]. This fact can be exploited to distinguish stationary targets from sea clutter.

Range resolution is directly related to temporal resolution. The temporal resolution is most easily understood by considering a simple pulsed carrier of pulse-width τ_p . Two closely spaced targets will appear as a single target if the radar pulse reflecting off the further target reaches the closer target before the closer target has completely reflected the original pulse. Due to the two-way travel associated with radar radio waves, the point of separation, which is the temporal resolution, is given by

$$\Delta t = \frac{\tau_p}{2} \quad (2-1)$$

Range resolution is simple conversion from time to space as follows

$$\Delta r = c\Delta t = \frac{c\tau_p}{2} \quad (2-2)$$

where

c is the velocity of radio wave propagation.

More generally, the temporal resolution depends on the specific nature of the radar signal, but in all cases it is inversely proportional to the bandwidth of the transmitted signal. A pulsed carrier has a spectral characteristic of the form of a sinc function with a 3 dB bandwidth, B , of $1/\tau_p$. Therefore the temporal and range resolutions, represented in terms of the signal bandwidth, are as follows:

$$\Delta t = \frac{1}{2B} \quad (2-3)$$

$$\Delta r = \frac{c}{2B} \quad (2-4)$$

This relationship is the most general representation of range resolution, being applicable to more complex waveforms. For instance a pulsed linear frequency modulated (FM) waveform, or *chirp*, could have a bandwidth much wider than that dictated by its pulse width, and the bandwidth ultimately determines the range resolution, not the pulse width. This will be illustrated later on.

Doppler resolution is directly related to frequency resolution and is inversely proportional to the duration of the transmitted signal. The Doppler phenomenon is a frequency shift in the waveform reflected from a moving target with a radial velocity of v_r . The frequency shift is given as [3]

$$f_d = \frac{2v_t}{\lambda} = \frac{2v_t f_c}{c} \quad (2-5)$$

where

λ is the wavelength of the carrier with frequency f_c .

Considering again the spectral characteristic of a simple pulsed carrier waveform, two pulses reflected from coincident moving targets with different instantaneous velocities would be distinguishable in the frequency domain if their respective sinc functions are sufficiently separated. The smaller the width of the main lobe of the sinc functions, the closer these functions can be positioned along the frequency axis and still distinguished from one another. Since the width of the sinc function is inversely proportional to the pulse width, the frequency resolution, and thus the Doppler resolution, is inversely proportional to the pulse width according to the following relationship

$$\Delta f_d = \frac{1}{\tau_p} \quad (2-6)$$

Analogous to range resolution, the reciprocal relationship implies that for a pulsed carrier the frequency resolution is equal to the bandwidth; however, the most general representation for frequency resolution is

$$\Delta f_d = \frac{1}{T_s} \quad (2-7)$$

where

T_s is the overall signal duration.

2.3 The Complex Envelope

Radar analyses usually deal with narrowband signals where the signal spectrum is concentrated in the vicinity of the carrier frequency [9]. Such analyses are often carried out on the complex envelope of the waveform that provides a representation of the signal independent of the carrier frequency. For many analyses, including assessments of range-Doppler ambiguity, the carrier frequency is irrelevant. More importantly, for digital simulations, a sample rate can be chosen relative to the bandwidth of the signal when a complex envelope representation is used. Certain analyses are dependent upon

the carrier frequency—for instance, the study of propagation phenomena—but these are outside the scope of this thesis; therefore all analyses presented will be in complex envelope form. However, as noted by equation (2-5), the Doppler frequency shift is determined through knowledge of the carrier frequency—therefore, the carrier frequency is maintained in the analyses for the purposes of scaling frequency to velocity.

The complex envelope representation is valid for narrowband signals, or under the condition $B \ll f_c$. A signal comprising an amplitude and phase modulated carrier is represented by the following relationship

$$s(t) = a(t) \cos[2\pi f_c t + \phi(t)] \quad (2-8)$$

where $a(t)$ represents the time-varying amplitude and $\phi(t)$ represents the time-varying phase. The real signal represented by the above expression is derived from the complex envelope of the signal, $\tilde{s}(t)$, as follows

$$s(t) = \text{Re}[\tilde{s}(t) \exp(j2\pi f_c t)] \quad (2-9)$$

where

$$\tilde{s}(t) = a(t) \exp[j\phi(t)] \quad (2-10)$$

Clearly the information content of the real signal $s(t)$ is completely represented by the complex envelope $\tilde{s}(t)$ [10]. $\tilde{s}(t)$ may also be expressed in complex Cartesian form rather than polar form as follows:

$$\tilde{s}(t) = s_I(t) + js_Q(t) \quad (2-11)$$

where

$s_I(t)$ is the *in-phase* component, and

$s_Q(t)$ is the *quadrature* component.

It is relevant at this point to introduce the concept of an *analytic signal*, as it is related to the above discussion and referred to later on. Referring back to equation (2-9),

the expression inside the square brackets is known as the *pre-envelope*. The pre-envelope, $s_+(t)$, is related to the real signal, $s(t)$, by the following relationship:

$$s_+(t) = s(t) + j\hat{s}(t) \quad (2-12)$$

where

$\hat{s}(t)$ is the Hilbert transform of $s(t)$.

The Hilbert transform is well-known and defined in many texts (e.g., [10]), but one important property is that a signal and its Hilbert transform are orthogonal (as defined later in equation (3-7)). The relationship between a real signal, its pre-envelope and complex envelope is best observed graphically, as shown in Figure 2-2. This has an important practical implication for coherent radar, where usually, a real signal is digitized, whereupon the analytic signal is formed to remove negative frequencies. The data rate can now be decimated by a factor of two since there are no negative frequencies to alias into the positive frequencies. The analytic signal is then frequency shifted so that the signal bandwidth is centered at zero hertz, which is the complex envelope of the signal. It's a matter of semantics, but some sources state that the complex envelope is an analytic one, in the sense that the in-phase and quadrature components of the complex envelope are orthogonal. However, other references define an analytic signal as being one with no negative frequencies. Either way, the complex envelope carries the same benefit as the pre-envelope in that the minimum sample rate necessary to avoid aliasing is a factor of two less than that for a real signal. This factor will render savings in processing bandwidth needed to perform desired computations on the complex envelope.

Note that the energy of the complex envelope is twice that of the real signal from which it is derived. This is easily seen by noting that the amplitude of the complex envelope spectrum is twice that of the real signal spectrum. The squaring operation in the energy calculation yields a factor of four, compared with a factor of two resulting from the addition of energies from the two sidebands of a real signal.

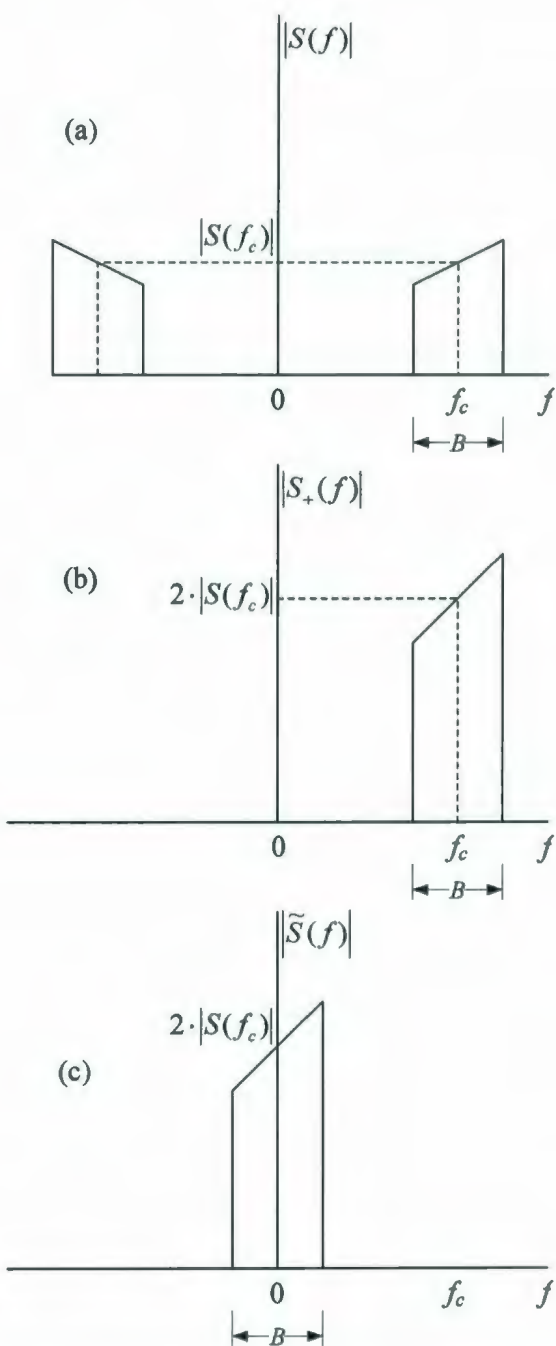


Figure 2-2: (a) Amplitude spectrum of real signal, $s(t)$. (b) Amplitude spectrum of pre-envelope of $s(t)$. (c) Amplitude spectrum of complex envelope of $s(t)$. (Adapted from [10])

For convenience, all subsequent references to the signal $s(t)$ assume a complex envelope representation.

2.4 Radar Ambiguity Function

For any waveform design, the range and Doppler resolution capability is evaluated through the *ambiguity function*, or *range-Doppler ambiguity*. A radar waveform's ambiguity function is probably the most complete statement of the waveform's inherent performance [3]. Examples of using the ambiguity function to assess the application of radar signal designs can be found in [11], [12], [13], and [14], covering a wide array of signal types.

The ambiguity function is an extension of a matched filter whereby a range of Doppler shifted versions of the transmitted signal is considered. The matched filter is the optimal filter that can be employed in a receiver to maximize the signal-to-noise ratio (SNR) of the detected output [10]. The impulse response, $h(t)$, of a matched filter is the conjugate of the time-reversed transmitted signal, $s_t(t)$, as follows

$$h(t) = s_t^*(-t) \quad (2-13)$$

Here, the transmitted waveform, in the context of the matched filter implementation, is often referred to as a *replica*.

The matched filter output is the convolution of the received signal, $s_r(t)$, with the impulse response of the matched filter, or equivalently, the cross-correlation between the transmitted and received signals as follows

$$g(\tau) = \int_{-\infty}^{\infty} s_r(t) s_t^*(t - \tau) dt \quad (2-14)$$

By evaluating the matched filter at Doppler shifted versions of the transmitted signal the *correlation function* is obtained as follows

$$\chi(\tau, f_d) = \int_{-\infty}^{\infty} s_r(t) s_t^*(t - \tau) \exp(j2\pi f_d t) dt \quad (2-15)$$

where

f_d is the Doppler frequency shift.

Note that this relationship can be easily represented in terms of velocity by using equation (2-5).

The magnitude of the correlation function is commonly known as the *ambiguity surface* [3] or the *uncertainty function*, and the ambiguity function is the squared magnitude of the correlation function as follows

$$\psi(\tau, f_d) = |\chi(\tau, f_d)|^2 \quad (2-16)$$

There are a couple of interesting properties for the ambiguity function [15]:

1. The maximum value of the ambiguity function occurs at $(\tau, f_d) = (0, 0)$ and is a constant equal to $4E^2$, where E is the energy of the real signal.
2. The volume under the ambiguity function is a constant equal to $4E^2$.

The first property can be explained intuitively. The origin is the point where the waveform and its reference are perfectly aligned in time and in frequency shift—there is no condition that can produce a higher correlation output. Since the magnitude squared of a complex signal is equal to the product of the signal and its complex conjugate, equation (2-15) reduces, at the origin, to the definition of energy. As noted earlier in Section 2.3, the energy of the complex envelope is twice that of its associated real signal; therefore, due to the subsequent squaring operation of the uncertainty function, the factor of 4 is applied to E^2 .

Interpreting the second property, it is clear that the underlying objective in radar signal design, for a given application, is to favorably distribute a finite and fixed amount of energy over the range-velocity plane. Ideally, all of the energy would be focused at the origin and yield infinitesimal range and velocity resolution. Such an uncertainty function is commonly known as the *thumbtack* response; however, it is not practically realizable.

This thesis will later develop the range-Doppler ambiguity for a SFM waveform, but two simple cases will serve as a point of reference or baseline—these are a constant-frequency pulse and a linear FM pulse. A discussion on the mathematical representation of radar signals is first required.

2.5 Constant Frequency Pulse

One of the simpler radar signals is a constant-frequency pulse, which can be generated by gating a constant-frequency carrier wave, as shown in Figure 2-3.

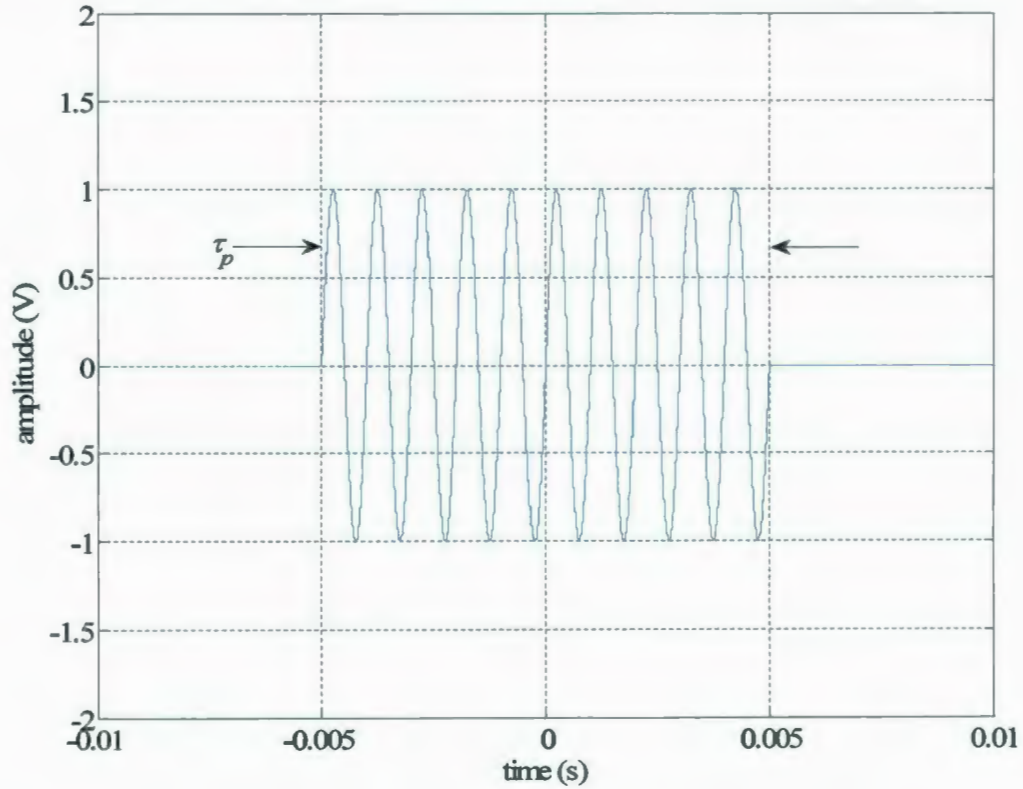


Figure 2-3: Constant-Frequency Pulsed Waveform

Using a complex envelope representation, a constant-frequency pulse is described by the following relationship:

$$s(t) = \text{Rect}\left(\frac{t}{\tau_p}\right) \quad (2-17)$$

where

$$\text{Rect}\left(\frac{x}{b}\right) = \begin{cases} 1 & |x| < b/2 \\ 0 & |x| > b/2 \end{cases}$$

The range-Doppler ambiguity can be derived analytically through the correlation function, noting that $\text{rect}(t/\tau_p)$ is real, as follows

$$\chi(\tau, \omega_d) = \int_{-\infty}^{\infty} \text{Rect}\left(\frac{t}{\tau_p}\right) \text{Rect}\left(\frac{t-\tau}{\tau_p}\right) \exp(j\omega_d t) dt \quad (2-18)$$

Equation (2-18) [7] is reduced in Appendix A.1 to:

$$\chi(\tau, \omega_d) = (\tau_p - |\tau|) \exp\left(\frac{j\omega_d \tau}{2}\right) \text{Sinc}\left(\frac{\omega_d(\tau_p - |\tau|)}{2}\right) \text{Rect}\left(\frac{\tau}{2\tau_p}\right) \quad (2-19)$$

2.6 Linear Frequency Modulation

The constant-frequency pulse can be modified by modulating the carrier wave within the gated region. If a frequency modulation is applied such that the frequency changes linearly with time, the radar waveform is known as linear frequency modulation (LFM), as shown in the example of Figure 2-4.

The complex envelope representation for a linear FM pulse is as follows:

$$s(t) = \exp(j\pi\alpha t^2) \text{Rect}\left(\frac{t}{\tau_p}\right) \quad (2-20)$$

where

α is the quadratic phase constant or chirp rate, and

$2\pi\alpha t$ is the instantaneous frequency.

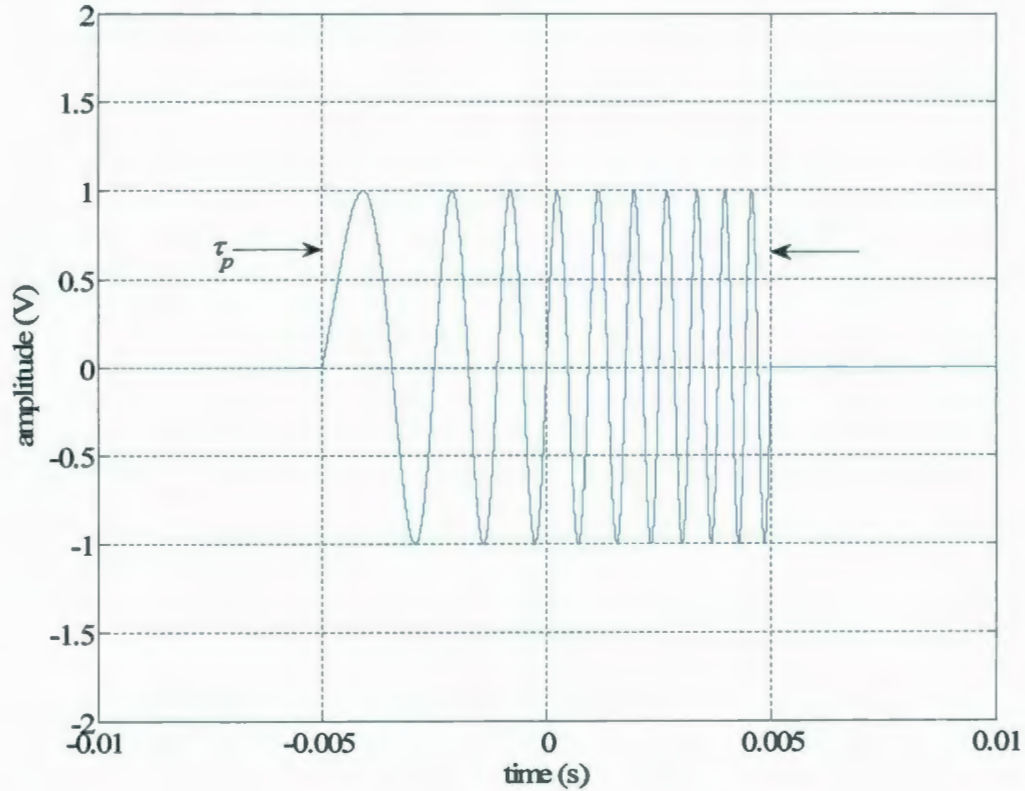


Figure 2-4: LFM Waveform

The correlation function for a linear FM pulse is analytically derived as follows:

$$\chi(\tau, \omega_d) = \int_{-\infty}^{\infty} \left\{ \text{Rect}\left(\frac{t}{\tau_p}\right) \text{Rect}\left(\frac{t-\tau}{\tau_p}\right) \cdot \exp(j\pi\alpha t^2) \exp(-j\pi\alpha(t-\tau)^2) \exp(j\omega_d t) \right\} dt \quad (2-21)$$

which is reduced in Appendix A.2 to the following:

$$\chi(\tau, \omega_d) = (\tau_p - |\tau|) \exp\left(j\frac{\omega_d \tau}{2}\right) \text{Sinc}\left(\left(\pi\alpha\tau + \frac{\omega_d}{2}\right)(\tau_p - |\tau|)\right) \text{Rect}\left(\frac{\tau}{2\tau_p}\right) \quad (2-22)$$

Clearly, this result is a generalization of (2-19), where $\alpha=0$ represents the case of a constant-frequency pulse.

2.7 Ambiguity Function Rendering

Ambiguity functions can be rendered for visual inspection in many forms—both 3-dimensional (3-D) and 2-dimensional (2-D), and both linear or logarithmic. A 3-D surface plot of the uncertainty function for an LFM waveform with a 1s pulse duration and a quadratic phase constant of 5 Hz/s is shown in Figure 2-5 (note that this waveform configuration yields a 5 Hz bandwidth). Figure 2-6 shows the uncertainty function as a 2-D contour plot.

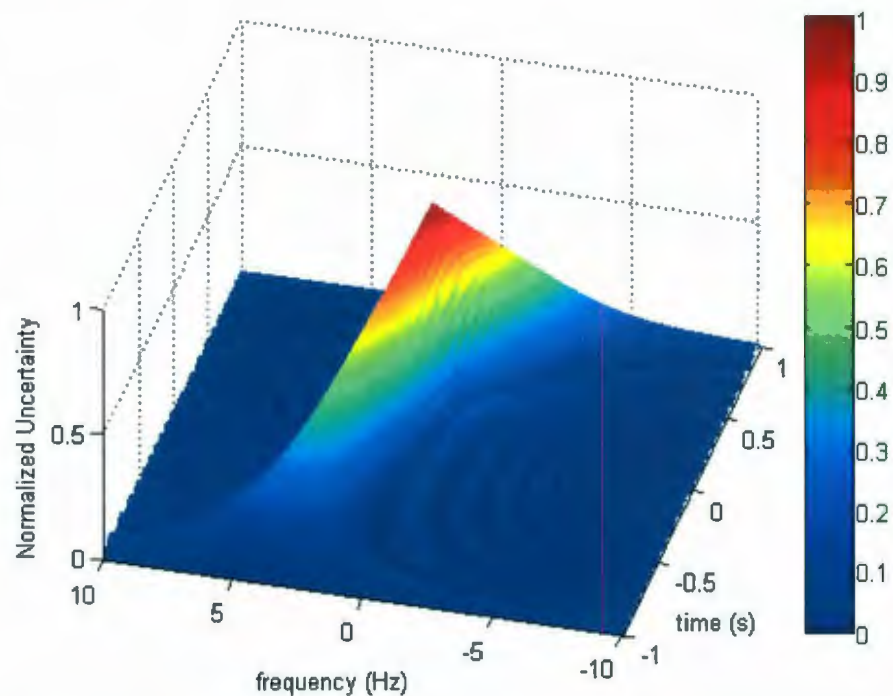


Figure 2-5: Surface Uncertainty Diagram for LFM Waveform, $\tau_p=1s$, $\alpha=5$ Hz/s

Often, a threshold is chosen so that the ambiguity diagram is represented as a single contour. This is useful for comparing the ambiguity diagrams of several different waveforms, or for investigating multiple lobes in an ambiguity diagram associated with a single waveform. When a threshold of one-half the peak value of the uncertainty function is chosen, a very useful result is observed.

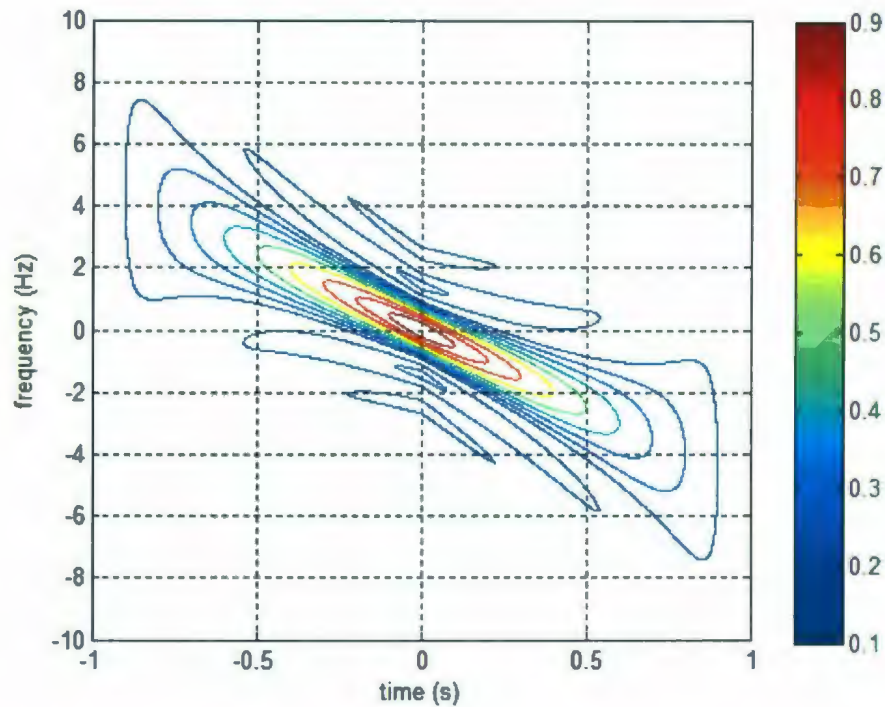


Figure 2-6: Contour Uncertainty Diagram for LFM Waveform, $\tau_p=1\text{s}$, $\alpha=5\text{ Hz/s}$

Figure 2-7 shows the same ambiguity diagram as shown in Figure 2-6, but with a single contour at 0.5 that forms an ellipse, and gridlines placed at specific points along the time and frequency axes. Four important observations can be made in this figure as follows:

1. the horizontal extent of the ellipse is approximately equal to the pulse width, 1s;
2. the vertical extent of the ellipse is approximately equal to the bandwidth, 5Hz;
3. the two zero-crossings of the ellipse along the time axis form an interval approximately equal to the inverse of the bandwidth, 0.2 s (or as discussed earlier, the temporal resolution); and
4. the two zero-crossings of the ellipse along the frequency axis form an interval approximately equal to the inverse of the pulse width, 1 Hz (or as discussed earlier, the frequency resolution).

These observations are illustrated in a general form in Figure 2-8. Note that the slope of the major axis of the ellipse-like contour is given by k , as follows:

$$k = \frac{B}{\tau_p} \quad (2-23)$$

The ambiguity diagram for a constant-frequency pulse of 1 s duration is shown in Figure 2-9. Here it can be seen that because the bandwidth is equal to the inverse of the pulse width, the axes of the ellipse are coincident with the time and frequency axes.

One further means to investigate the ambiguity function of a waveform is to view a planar slice through the surface plot. Two commonly used slices are the planes frequency=0 and time=0, as shown in Figure 2-10 and Figure 2-11 respectively, for the LFM waveform from Figure 2-5. Here, the temporal and frequency resolutions of the waveforms are respectively observed as shown.

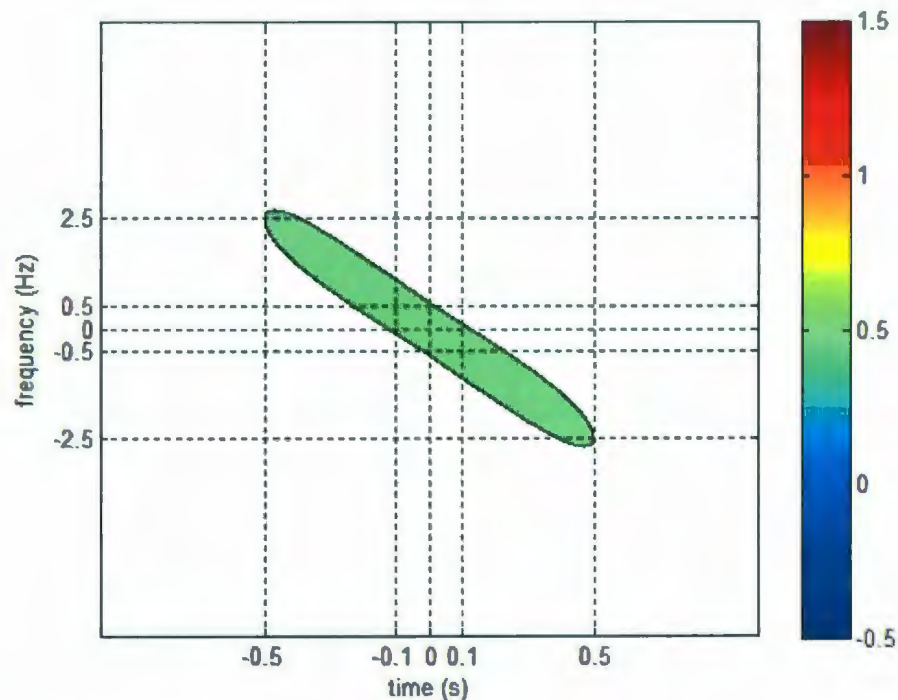


Figure 2-7: Contour Ambiguity for LFM Waveform, $\tau_p=1$ s, $\alpha=5$ Hz/s, Threshold=0.5

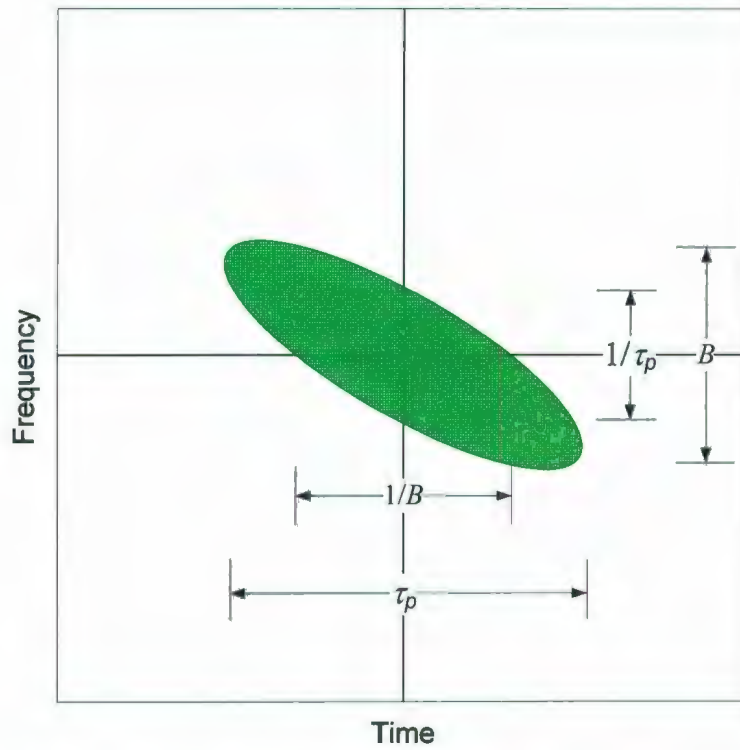


Figure 2-8: Generalized LFM Contour Ambiguity Diagram (adapted from [16])

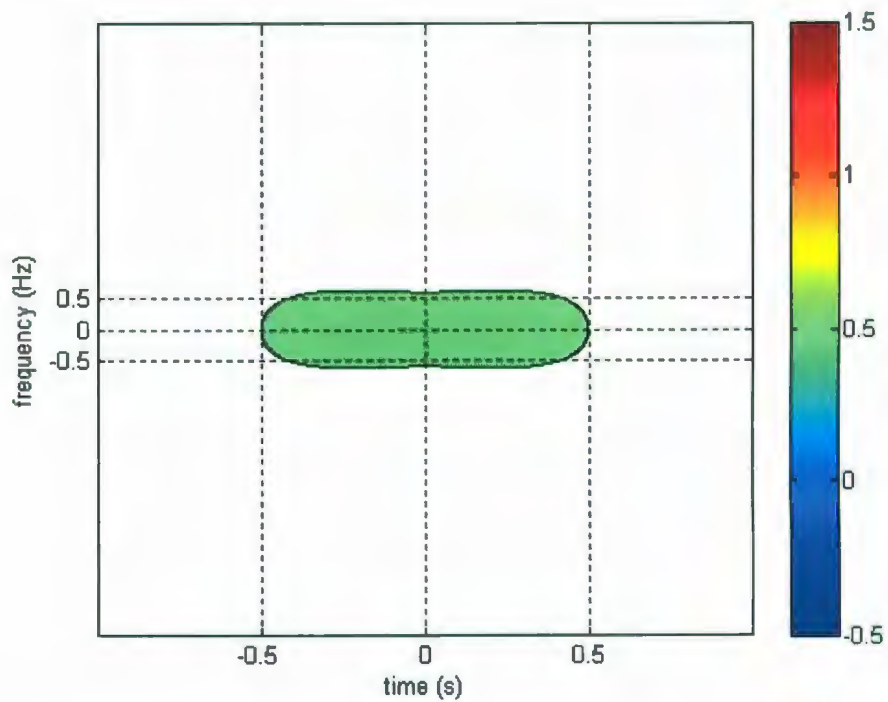


Figure 2-9: Contour Ambiguity for Pulsed Sinusoidal, $\tau_p=1s$, $\alpha=0$ Hz/s, Threshold=0.5

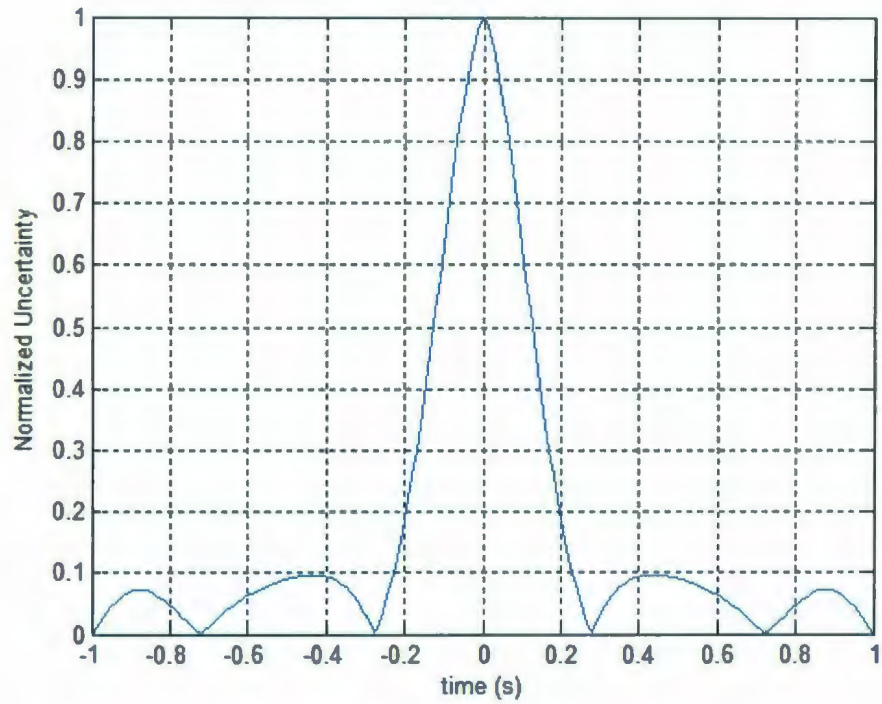


Figure 2-10: Uncertainty Function at frequency=0 for LFM Waveform, $\tau_p=1$ s, $\alpha=5$ Hz/s

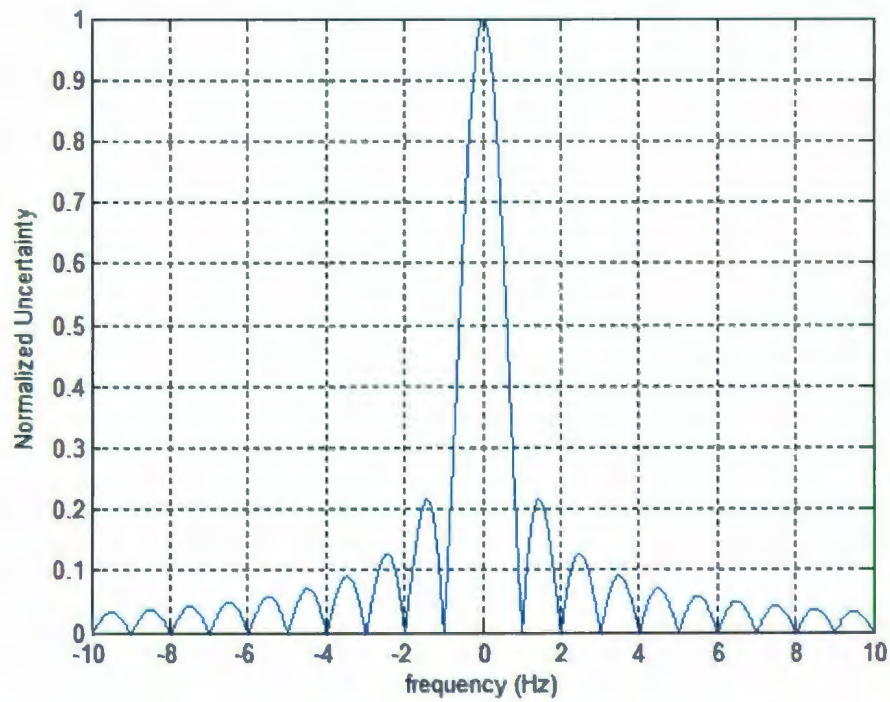


Figure 2-11: Uncertainty Function at time=0 for LFM Waveform, $\tau_p=1$ s, $\alpha=5$ Hz/s

2.8 Pulse Compression

Two final subjects need introduction prior to discussing the specific radar signals developed in this thesis—these are *time-bandwidth product* and *pulse-compression*. These subjects tie together many of the elements introduced previously.

It was shown that for a constant-frequency pulse, the temporal resolution is equal to the pulse width, which is also the inverse of the signal bandwidth. The product of the pulse width and the bandwidth of a radar signal is known as the time-bandwidth product (TBW) [3], and is equal to unity for a constant-frequency pulse, as shown in equation (2-24).

$$\begin{aligned} TBW &= \tau_p B \\ &= \tau_p \cdot \frac{1}{\tau_p} = 1 \quad (\text{for a constant - frequency pulse}) \end{aligned} \quad (2-24)$$

For a given pulse width, if the bandwidth is increased beyond that of a constant-frequency pulse through phase or frequency modulation, then the TBW increases. For the example shown in Figure 2-5, Figure 2-6 and Figure 2-7, the TBW is five. The TBW is also a ratio of the original pulse width to the compressed pulse width—or indirectly, the original range resolution compared with the range resolution achievable through pulse compression. For this reason, the TBW is also known as the *pulse compression ratio*, since the resolution obtained from a given pulse width is improved, or compressed, by a factor equal to the TBW. And, the method of increasing the TBW to enhance resolution is known as pulse compression. Figure 2-12 shows the matched filter output (ambiguity function at $f=0$ Hz) for a LFM $\alpha=20$ Hz/s. Drawing a comparison to Figure 2-10, it is clear that the increase in TBW resulting from an increase in α by some factor, improves the temporal resolution (and thus range resolution) by the same factor. A summary of the comparison is provided in Table 2-1, along with a comparison to the special case of $\alpha=0$, or a constant-frequency pulse.

There is also an associated signal level increase, or gain, associated with pulse compression that is equal to the TBW. Since this gain is derived from a correlation

operation, it is known as *processing gain*, and is usually expressed in decibels, as follows [4]:

$$G_p = 10 \log(\tau_p B) = 10 \log(TBW) \quad (2-25)$$

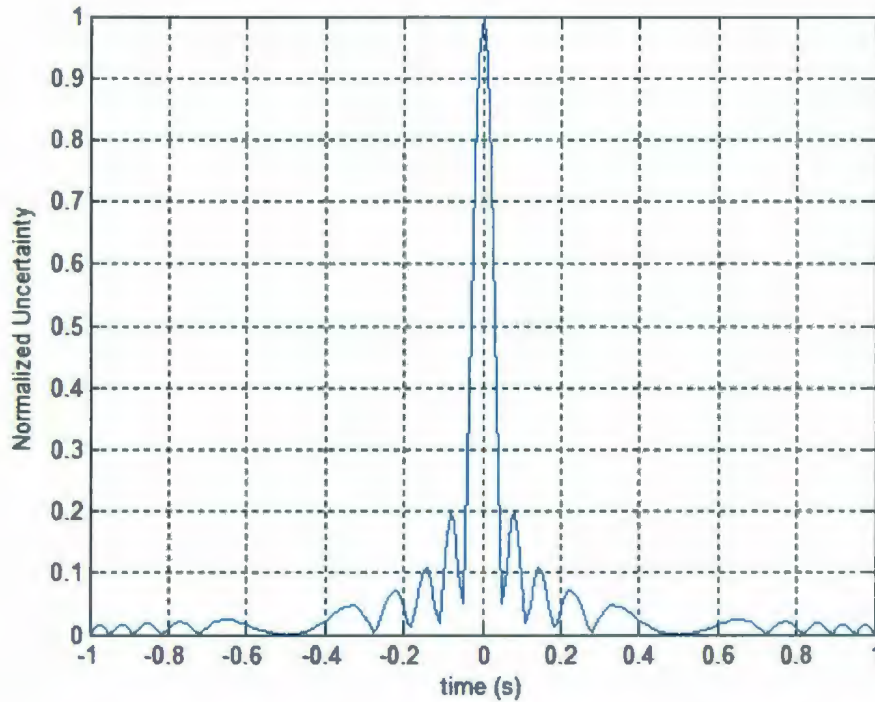


Figure 2-12: Uncertainty Function at frequency=0 for LFM Waveform, $\tau_p=1$ s, $\alpha=20$ Hz/s

Table 2-1: Comparison between LFM waveforms— $\alpha=5$ and $\alpha=20$

α	τ_p	TBW	Δt
5Hz/s	1s	5	0.2s
20Hz/s	1s	20	0.05s
0Hz/s	1s	1	1s

A comparison of Figure 2-10 and Figure 2-12 reveals a tradeoff associated with exploiting pulse compression to achieve improved temporal resolution. The sidelobe levels relative to the main lobe of the matched filter output are higher for higher pulse

compression ratios. To remedy this, other modulation methods and/or processing methods can be overlaid on the LFM waveform to reduce these levels. However, these methods also have associated tradeoffs. Generally, all of these methods have the effect of reducing the sidelobe levels at the expense of compromising the main lobe with respect to its width and/or peak amplitude. In other words, the tradeoff is some increase in temporal resolution and/or some decrease in SNR.

One common method of sidelobe reduction is amplitude weighting, or windowing, in the time domain or the frequency domain [17]. This weighting can be implemented on the received waveform—in fact this is preferred, since the SNR is improved by maximizing the transmitted signal levels across all frequencies. For time domain weighting, a replica of the transmitted waveform can be multiplied by a window function prior to the matched filter computation, which in the time domain is a convolution operation. For frequency domain weighting, the spectrum of the window function is convolved with the spectrum of the replica prior to matched filter computation, which in the frequency domain is a multiplication operation.

Figure 2-13 shows a Hamming window with a duration equal to the pulse width in the previous example (1 s). The window is applied by multiplying the radar signal by the window function in a point-by-point manner. Figure 2-14 and Figure 2-15 show the uncertainty function for the previous example ($\alpha=20$), but with the Hamming window applied to the radar waveform. The resolution and sidelobe level trade-off is very evident in these plots.

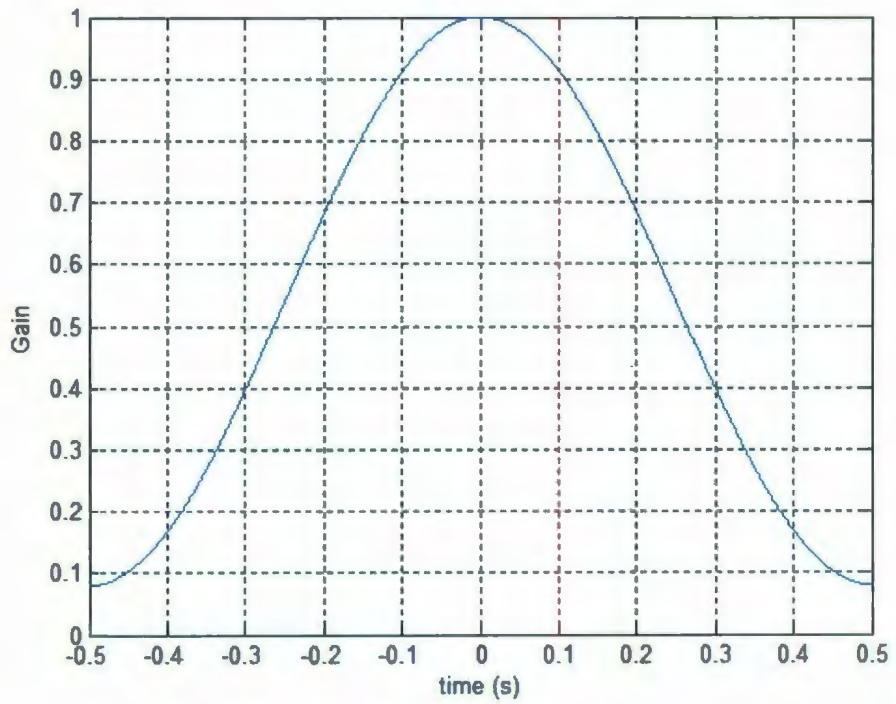


Figure 2-13: Hamming Window

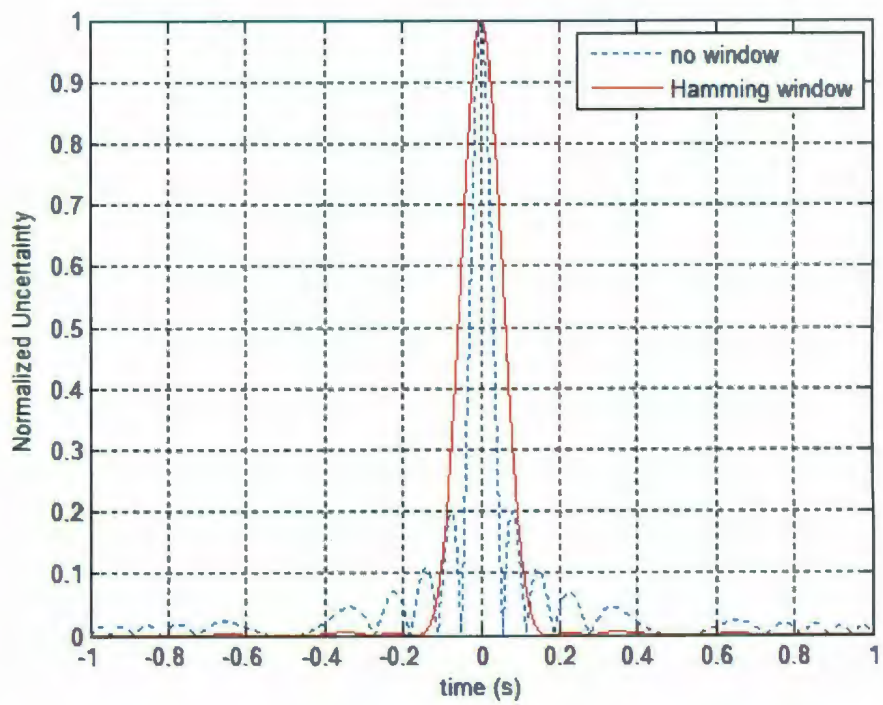


Figure 2-14: Uncertainty Function at $f=0$ for LFM Waveform, $\tau_p=1$ s, $\alpha=20$ Hz/s

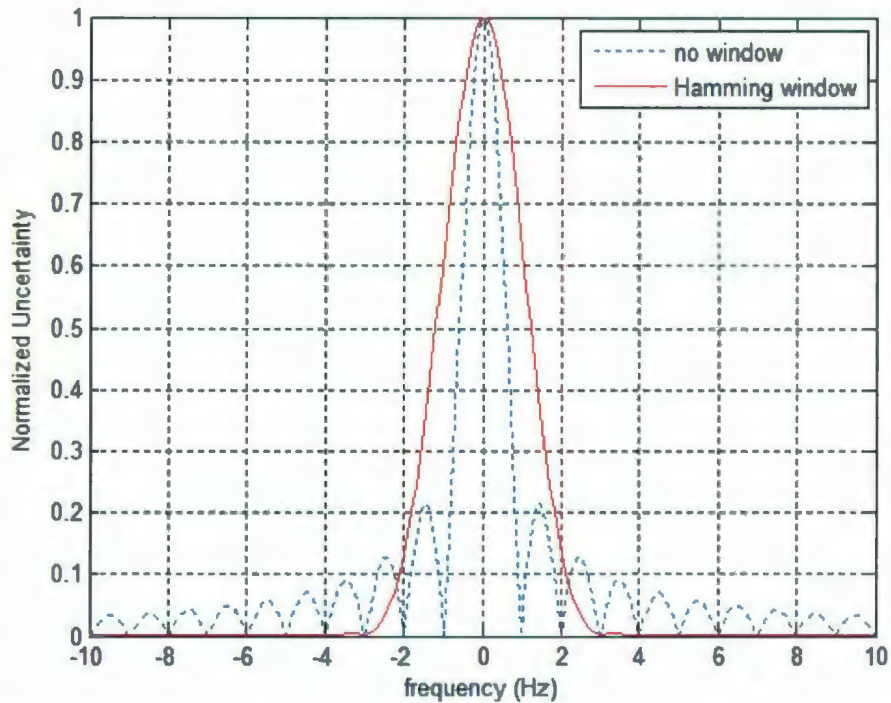


Figure 2-15: Uncertainty Function at time=0 for LFM Waveform, $\tau_p=1$ s, $\alpha=20$ Hz/s

Another method of pulse compression is phase coding. In this case, the radar pulse is segmented into N smaller pulses, where each pulse is assigned a phase offset according to some predetermined favorable pattern or coding scheme. Examples of such coding schemes include Barker Codes, Frank Codes and Maximal Length Sequences [15]. An example of phase coding is shown in Figure 2-16. Here, a continuous-wave (CW) pulsed-radar signal is multiplied by a 13-bit Barker Code ([1 1 1 1 1 -1 -1 1 1 -1 1 -1 1]). The resultant uncertainty function for $v=0$ is shown in Figure 2-17. Note the dramatic improvement over the triangular correlation that is yielded from a simple pulsed sinusoid. Particularly favorable is the flat sidelobe structure. However, the output from Barker Coding is known to be subject to rapid degradation in the presence of a Doppler shift [17]. This is evident in Figure 2-18 where the uncertainty surface is shown over a range of velocities. The application that supported the development of the coherent radar described by this thesis is moving targets in the ocean. Phase coding is not well-suited to this application; therefore, the next section will focus exclusively on a special form of linear FM—stepped frequency modulation (SFM). However, the above example serves

to illustrate the type of analysis that should be executed in selected the best waveform for a given application.

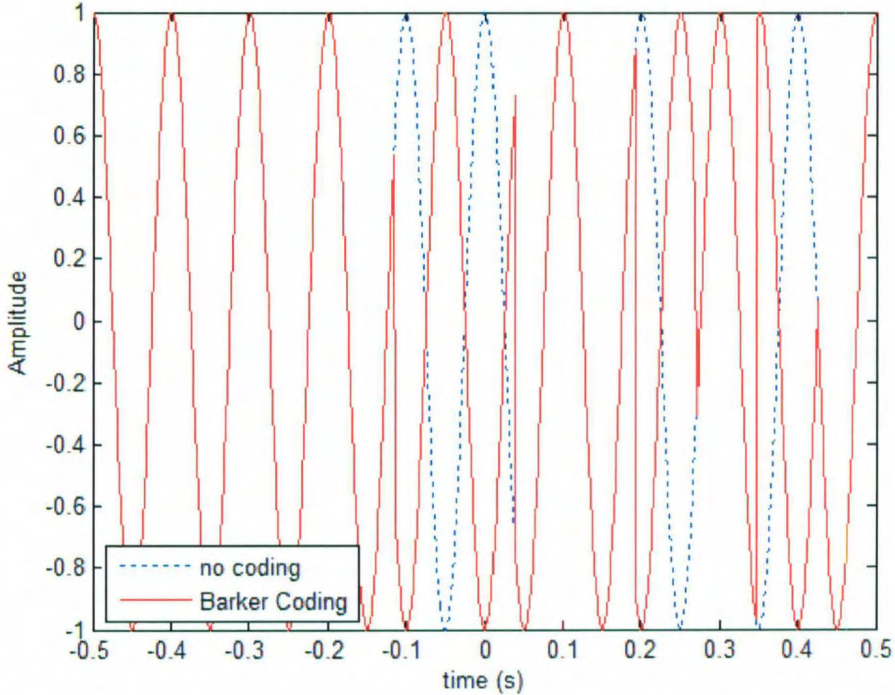


Figure 2-16: 13-bit Barker Coded Sinusoid, $f=10$ Hz

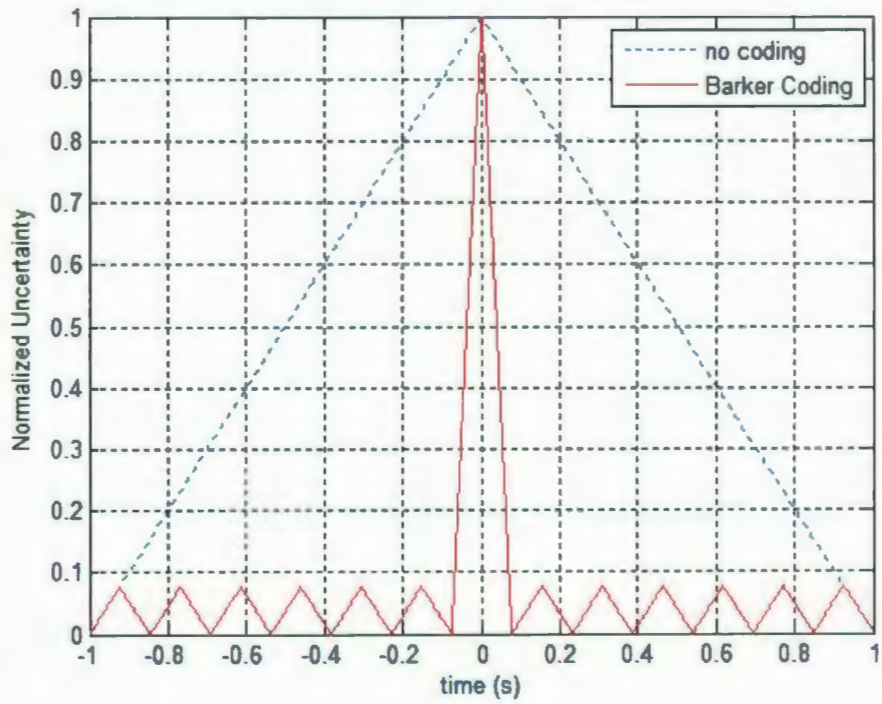


Figure 2-17: Uncertainty Function at time=0 for 13-bit Barker Coded Sinusoid, $f=10$ Hz

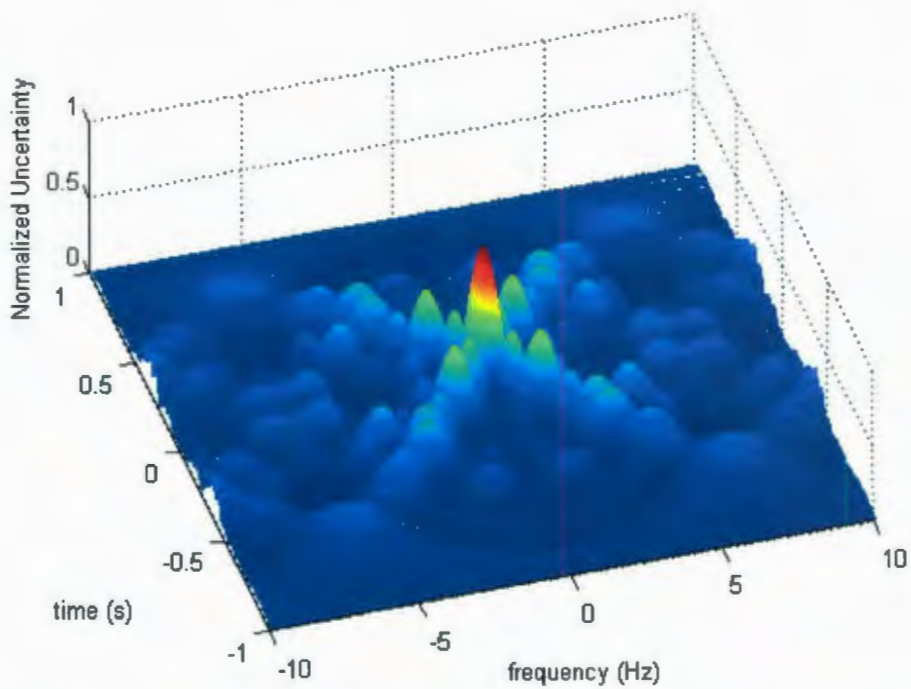


Figure 2-18: Uncertainty Surface 13-bit Barker Coded Sinusoid, $f=10$ Hz

3. Stepped Frequency Modulation

The LFM waveform presented earlier is useful for low duty-cycle *monostatic* applications (single or collocated transmit and receive antennas) where the desired bandwidth can be transmitted in a short enough period of time not to compromise the desired range extent of targets. The receiver is usually gated off during transmission since cross-coupling will saturate the receiver, rendering near targets undetectable. Short-range targets within a range equivalent to one-half of the signal duration, or the *blanking range*, are masked. However, in some applications it is not practical to transmit the entire bandwidth over a single short pulse. In these cases, the radar designer, if certain tradeoffs can be made, may transmit the desired bandwidth over a larger period of time and/or utilize a larger duty-cycle. Three specific variations of the LFM waveform that employ this method are the frequency modulated continuous waveform (FMCW), the frequency modulated interrupted continuous waveform (FMICW), and stepped frequency modulation (SFM). All three waveforms, in addition to LFM, are illustrated in Figure 3-2.

The FMCW waveform, shown in Figure 3-2(b), is typically employed only for bistatic applications (separate isolated transmit and receive antennas) where the receiver can listen while the signal is transmitted; although, low-power monostatic applications are also feasible [18] where the transmitter does not saturate the receiver. Processing within the receiver may consider just a single cycle or multiple cycles.

Sometimes it is not practical to collocate a transmitter and receiver with sufficient isolation to facilitate FMCW. FMICW is a modification of FMCW, designed to permit monostatic operation while retaining some of the advantages of FMCW [9]. In essence, a bandwidth equivalent to FMCW is transmitted, but in a gated manner so that not all frequency components are included, as shown in Figure 3-2(c). Since the bandwidth is not altered, the range resolution is not compromised; however, this method does limit the range extent and poses a greater potential for range ambiguities, or target reflections from one pulse being received following the next transmitted pulse.

SFM is a simple adaptation of FMICW that provides certain conveniences in both the generation of the waveform and the implementation of the pulse compression

algorithm in the receiver. Instead of simply gating an FMCW waveform, each transmitted pulse comprises a single frequency rather than a slice of an FMCW waveform, but the frequency of successive pulses follows the profile of the FMCW waveform, as shown in Figure 3-2(a). From a mathematical perspective, SFM is equivalent to FMICW, in that the same performance is obtained. Furthermore, the processing load for SFM can be fully distributed so that the data from each transmit pulse can be processed separately and combined after the waveform cycle (portion of the waveform occurring over T_s) is complete. This has obvious implications for real-time display of processed radar data.

The SFM waveform is shown in the time domain in Figure 3-1.

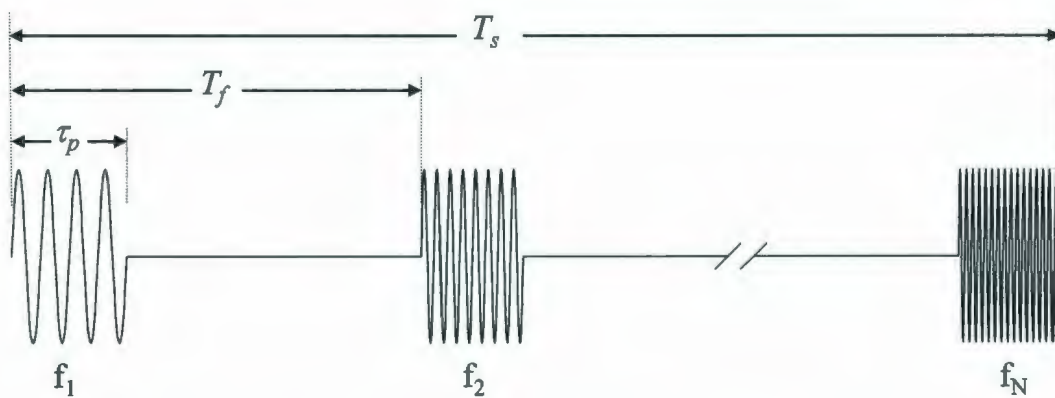


Figure 3-1: Time domain representation of a SFM waveform

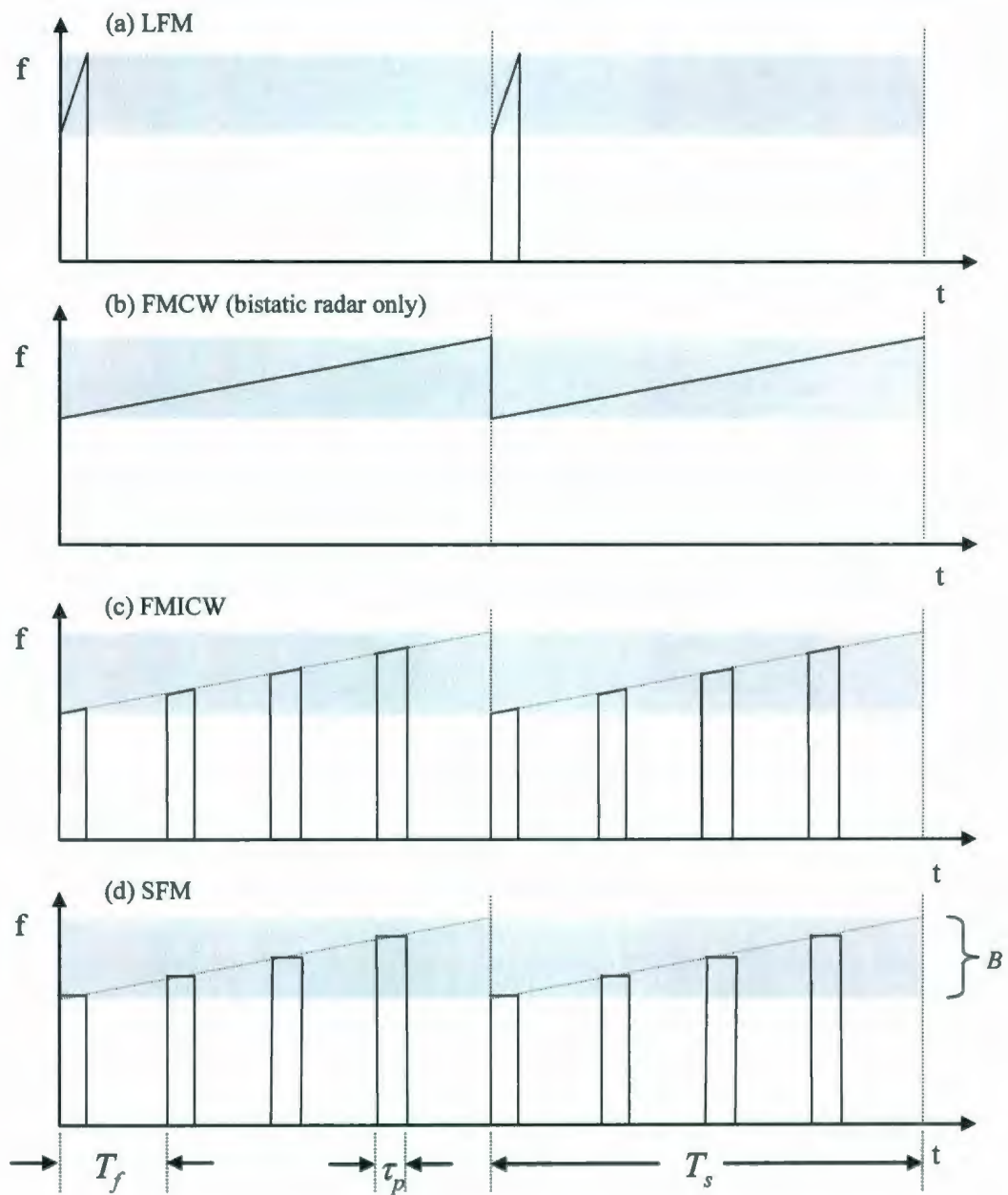


Figure 3-2: Linear FMCW, FMICW and SFM radar waveforms

While the abovementioned FM methods employ a linear modulation, there are many methods that employ non-linear modulation to achieve specific advantages. For example, in [18] the authors have proposed a pseudorandom FMICW interrupt sequence whereby the gate widths and separations are varied across the signal bandwidth according to some deterministic pattern with the effect of reducing ambiguity pop-ups in specified regions

of the ambiguity surface. Figure 3-3 shows a comparison between the matched filter response, or uncertainty response at $v=0$, for a pulse stream comprising a set of random frequencies and a set of linear frequencies over a 1 MHz bandwidth. In comparing these two plots, it is evident that while both waveforms yield similar range resolution as seen in the main lobe, the sidelobe structure for in the case of random frequency assignments is inferior to that of linear SFM.

The subject of non-linear, random or pseudorandom frequency sets would require substantial discussion and is outside the scope of this thesis. The focal point here will be linear modulation and SFM.

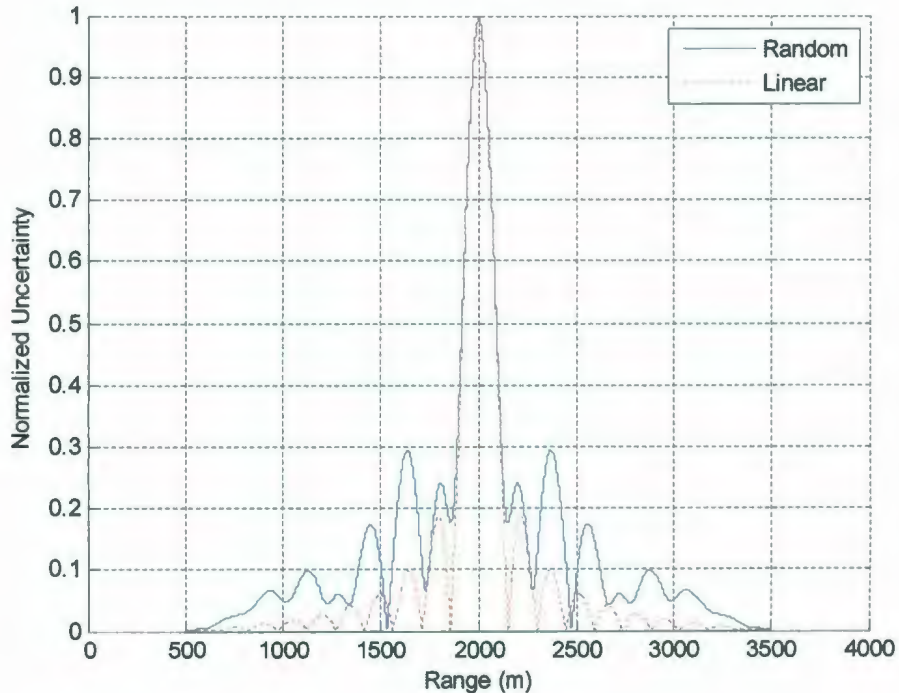


Figure 3-3: Matched Filter Response for SFM with Random and Linear Frequency Assignments, $\tau_p=10$, $B=1$ MHz, $N_p=11$

3.1 SFM Analytical Representations

A waveform comprising a series of pulses, each at a different frequency, can be generally represented as a complex envelope, as follows:

$$u(t) = \sum_{n=0}^{N_p-1} \exp(-j\phi_n) \cdot \exp(j2\pi f_n(t - nT_f)) \cdot \text{Rect}\left(\frac{t - nT_f}{\tau_p}\right) \quad (3-1)$$

where

ϕ_n is the phase offset of the n^{th} pulse,

$\{f_n | 0 \leq n < N_p, n \in \mathbb{Z}\}$ is the set of frequencies for each pulse,

T_f is the pulse repetition period,

N_p is the number of pulses, and

τ_p is the pulse width.

For SFM, the set of frequencies $\{f_n\}$ comprise equi-spaced components increasing or decreasing monotonically in a linear manner with frequency step Δf , as represented in equation (3-2). Notice the bandwidth symmetrically spans negative and positive frequencies, which is typically representative of a complex baseband representation. This particular representation also requires N_p to be an odd integer, to maintain symmetry

$$u(t) = \sum_{n=-\lfloor N_p/2 \rfloor}^{\lfloor N_p/2 \rfloor} \exp(-j\phi_n) \cdot \exp[j2\pi n\Delta f(t - nT_f)] \cdot \text{Rect}\left(\frac{t - nT_f}{\tau_p}\right) \quad (3-2)$$

where

ϕ_n is the phase offset of the n^{th} pulse,

Δf is the frequency step,

T_f is the pulse repetition period,

N_p is the number of pulses, and

τ_p is the pulse width.

So for linear SFM, N_p and Δf collectively determine the bandwidth (B), which in turn dictate the range resolution, as discussed in Section 2.2. Alternatively, the waveform may be indirectly specified by the desired B , and either Δf or N_p . The associated tradeoffs will be discussed in the next section.

3.2 SFM Parameter Sets

As evident above, the parameter set for an SFM waveform has infinite possibilities; however, each application will limit the practical choices. For monostatic radar incorporating this particular waveform, the receiver is disabled for a duration equal to the length of the transmitted pulse, and targets in the associated blanking range are undetectable. So τ_p is readily chosen to be equal to the permissible blanking range, and usually no shorter so as to maximize the radiated energy and optimize target detectability. The pulse repetition period is sometimes chosen to be as short as possible so that the entire bandwidth can be covered in a short period of time. However, *range ambiguities* result when reflections from one pulse occur at a large enough range extent that they do not reach the radar until after the next pulse is transmitted. The reflection, being associated with the following pulse, appears to be at shorter range; therefore, the actual range is ambiguous. So usually, T_f is chosen to be equivalent to the maximum range (R_{max}) of interest, or $2R_{max}/c$. Echoes beyond this range are usually diminished in effect through signal processing. The bandwidth of the waveform is simply chosen from the desired range resolution, given by equation (2-4). Finally, the composition of the frequency set is dictated by the step size and number of pulses. As will be shown shortly, once the bandwidth and pulse width are chosen, there is a unique frequency step that yields preferred performance; therefore, the number of pulses remain as the last parameter to be chosen. N_p determines the overall duration of the waveform, which according to equation (2-7) sets the Doppler resolution; therefore, this last parameter can be chosen based on the velocity of targets that are of interest.

The preceding discussion merely suggest examples of how SFM parameters may be chosen for any application; however, these points are not intended to be rules, as the rationale applied in choosing the parameters may change from one application to the next. Table 3-1 summarizes some general considerations in choosing these parameters. Each parameter can be modified independently, so each associated observation (row in the table) assumes all other parameters remain fixed.

Table 3-1: SFM Signal Design Considerations

	Advantages of Increasing	Disadvantages of Increasing	Application Issues
τ_p	Increases total energy, which benefits the resultant SNR for any given target.	Increases the blanking range, thereby extending the range over which near targets cannot be detected. Increases the range extent of sidelobes that could potentially mask weak targets in the vicinity of strong targets (see Figure 2-8)	Minimize this parameter to detect near targets. Maximize this parameter to detect distant or weak targets.
T_f	Increases the unambiguous range. Improves Doppler resolution by increasing overall signal duration.	Yields more data adding burden to the radar processor.	Range ambiguities can be controlled by reducing the output power of the transmitter.
B	Improves range resolution. Improves TBW and therefore enhances SNR.	Increases the Doppler extent of sidelobes that could potentially mask weak targets in the vicinity, with respect to velocity, of strong targets (see Figure 2-8). Adds more processing burden to the radar processor.	Maximize this parameter detect small targets.
N_p	Improves Doppler resolution by increasing overall signal duration. Improves SNR because of increased averaging effect on noise.	Not well-suited to fast-moving targets (i.e. fast targets could prematurely exit the radar beam). Adds more processing burden to the radar processor.	With sufficient processing power, large cycle numbers are particularly useful for free-floating targets such as life-vessels and ice.

The forthcoming discussions will reveal more in regards to the effects of modifying the waveform parameters.

3.3 SFM Ambiguity Response

It is beneficial to compare the ambiguity responses of LFM, FMCW, FMICW and SFM to understand the implications of choosing between these waveforms. Example 1 provides ambiguity responses for these waveforms as shown respectively in Figure 3-4 through Figure 3-7. Non-realistic parameter values have been chosen for simplicity and illustration.

Example 1: LFM, FMCW, FMICW and SFM Comparison	
T_s	8 s (not applicable to FMCW)
τ_p	0.8s
T_f	2 s (not applicable to FMCW)
B	5 Hz
N_p	5

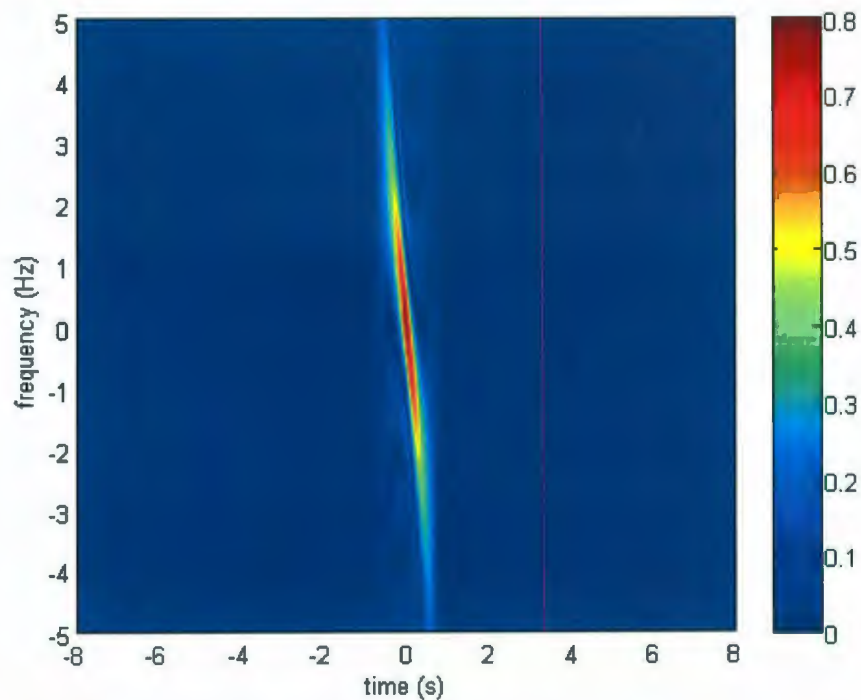


Figure 3-4: LFM Ambiguity Response

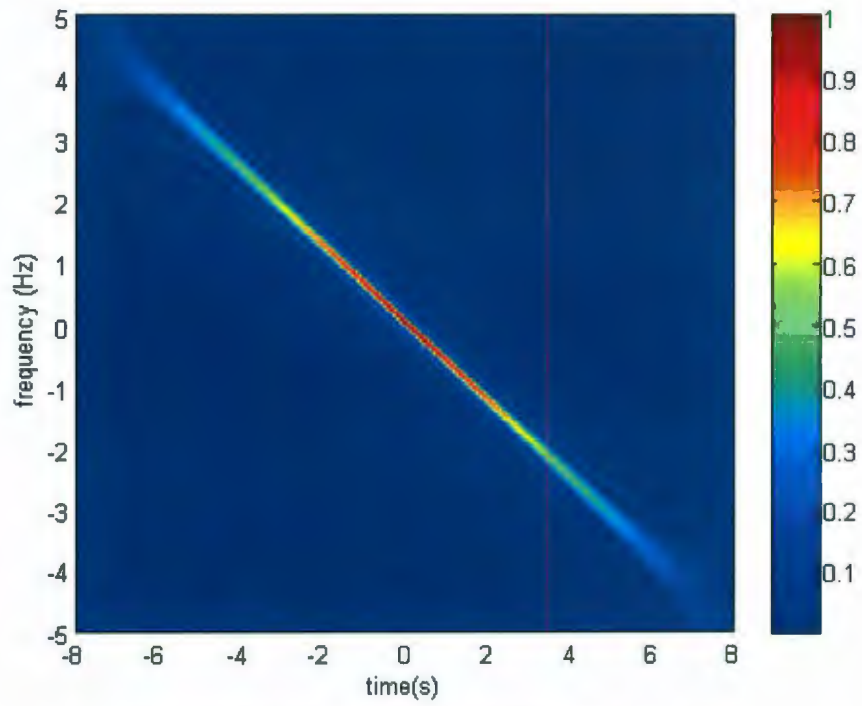


Figure 3-5: FMCW Ambiguity Response

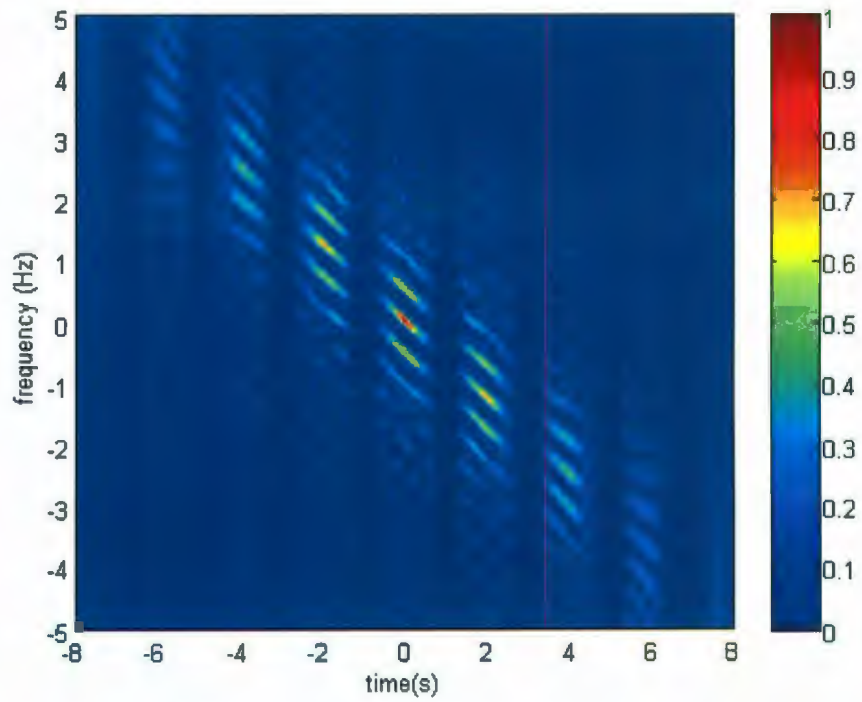


Figure 3-6: FMICW Ambiguity Response

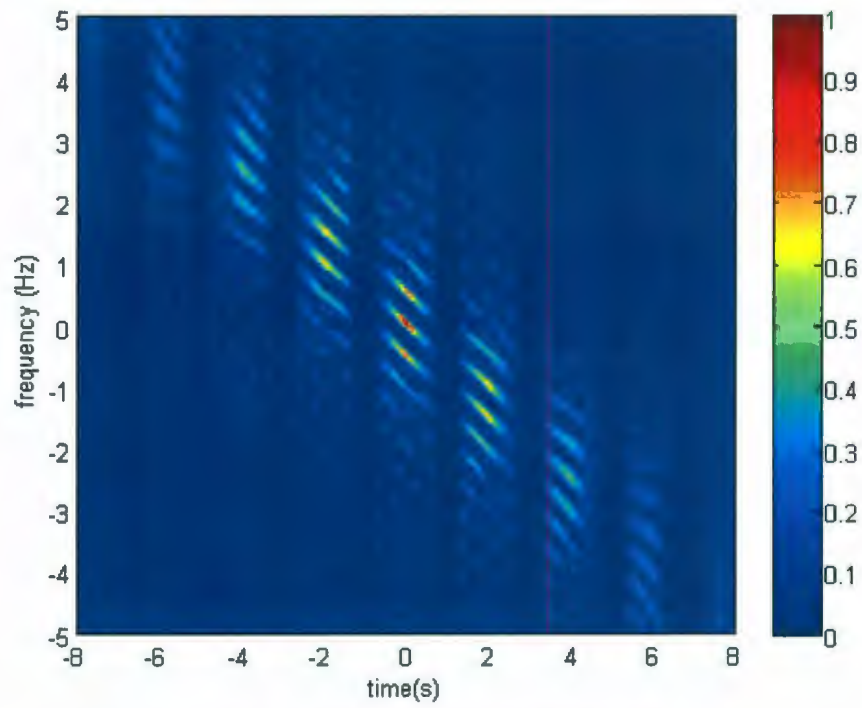


Figure 3-7: SFM Ambiguity Response

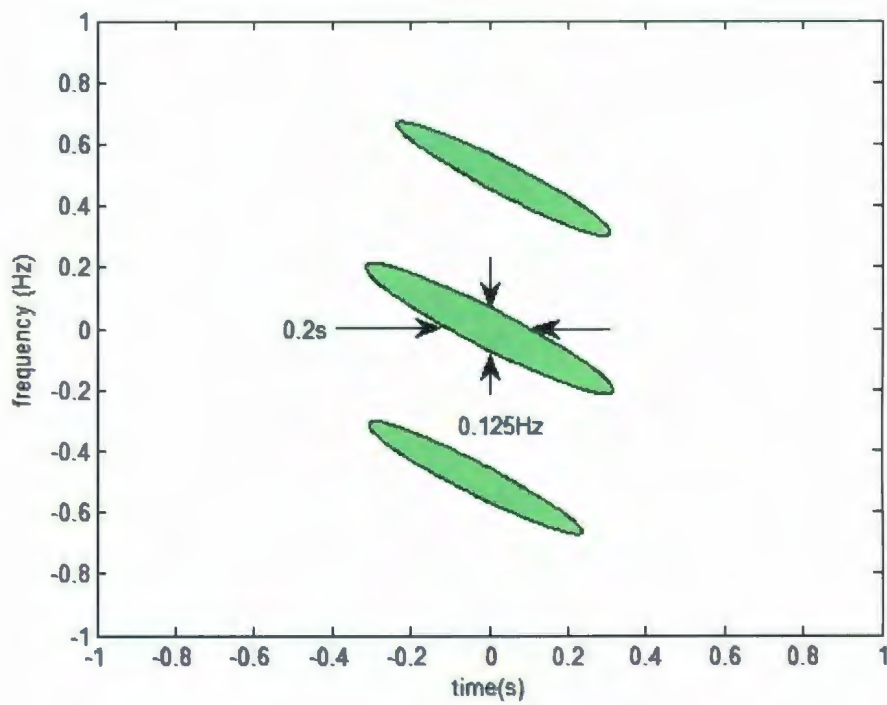


Figure 3-8: SFM Ambiguity Contour (zoomed)

A number of observations can be made in regards to the Example 1:

1. Since the bandwidth, B , is constant, the temporal resolution is identical across all cases. The observed temporal resolution is consistent with that predicted by equation (2-3), as shown in the contour diagram for the SFM ambiguity response in Figure 3-8 ($1/B = 1/5 \text{ Hz} = 0.2 \text{ s}$; the factor of 2 in the denominator is not applicable since the ambiguity response does not consider two-way travel).
2. Since the waveform length, T_s , is constant for FMCW, FMICW and SFM waveforms, the frequency resolution is identical across these three cases. The observed frequency resolution is consistent with that predicted by equation (2-7), as shown in the contour diagram for the SFM ambiguity response in Figure 3-8 ($1/T_s = 1/8 \text{ s} = 0.125 \text{ Hz}$).
3. The ambiguity response for FMCW is similar to that of LFM. The difference between the two waveforms simply lies in the portion of the waveform cycle that sweeps the bandwidth. So for a constant waveform cycle, the shape of the ambiguity response is identical, but is scaled differently. Comparing Figure 3-4 and Figure 3-5 it is evident that the temporal resolution is the same for both waveforms; however, the Doppler resolution is significantly poorer for LFM. The reason for this is that the overall waveform length is shorter in this particular example for LFM; therefore, according to equation (2-7), the Doppler resolution is larger. This exemplifies the advantage of applications, such as bi-static radar, where blanking the receiver is not required.
4. The ambiguity responses for FMICW and SFM waveforms are, for all intents and purposes, identical. This illustrates that waveform performance issues does not dictate the choice between FMICW and SFM waveforms. Instead, this choice is dictated by practical implementation considerations.
5. The observed slopes of the ambiguity contours are identical across FMCW, FMICW and SFM waveforms. The slope of the LFM ambiguity contour is steeper due to the fact that this waveform is shorter in duration, but equal in bandwidth, to the other waveforms.

A generalized ambiguity contour diagram for SFM is shown in Figure 3-9. First, observe that the FMCW contour of equal bandwidth and waveform length is shown by the dotted line. This contour encompasses *main-axis* contours of the SFM response. The slope of the major axis of the ellipse-like FMCW contour is given by (compare with equation (2-23) where T_s is replaced by τ_p):

$$k = \frac{B}{T_s} \quad (3-3)$$

Observe that SFM has the effect of segregating the FMCW response into sections that are τ_p in width and separated by the pulse repetition period, T_f . The number of segregated portions is equal to $2N_p-1$ (in this illustration, $N_p=2$ for simplicity). The response lobes observed off the main-axis are essentially a sampling phenomenon. Because SFM temporally samples an FMCW waveform, the frequency response yields frequency images, as evident in the examples above. The images are spaced at the sampling, or pulse repetition, frequency, $1/T_f$. This result is analogous to signal sampling theory where the sampled signal's spectrum is repeated at multiples of the sampling rate. These images are regarded as Doppler ambiguities.

Figure 3-9 also sheds light on the unambiguous range and velocity associated with any arbitrary SFM waveform. From the figure, it is clear that the unambiguous range is related to T_f and is given by:

$$R_u = \frac{cT_f}{2} \quad (3-4)$$

The unambiguous velocity, or *blind speed*, is given by (applying equation (2-5)):

$$v_b = \frac{c}{2T_f f_c} = \frac{\lambda}{2T_f} \quad (3-5)$$

The product of the unambiguous range and blind speed is a constant, as follows:

$$R_u v_b = \frac{cT_f}{2} \frac{\lambda}{2T_f} = \frac{c\lambda}{4} \quad (3-6)$$

Equation (3-6) sets an important practical limitation for radar design in that for an arbitrary unambiguous range and blind speed, a minimum wavelength must be chosen [19].

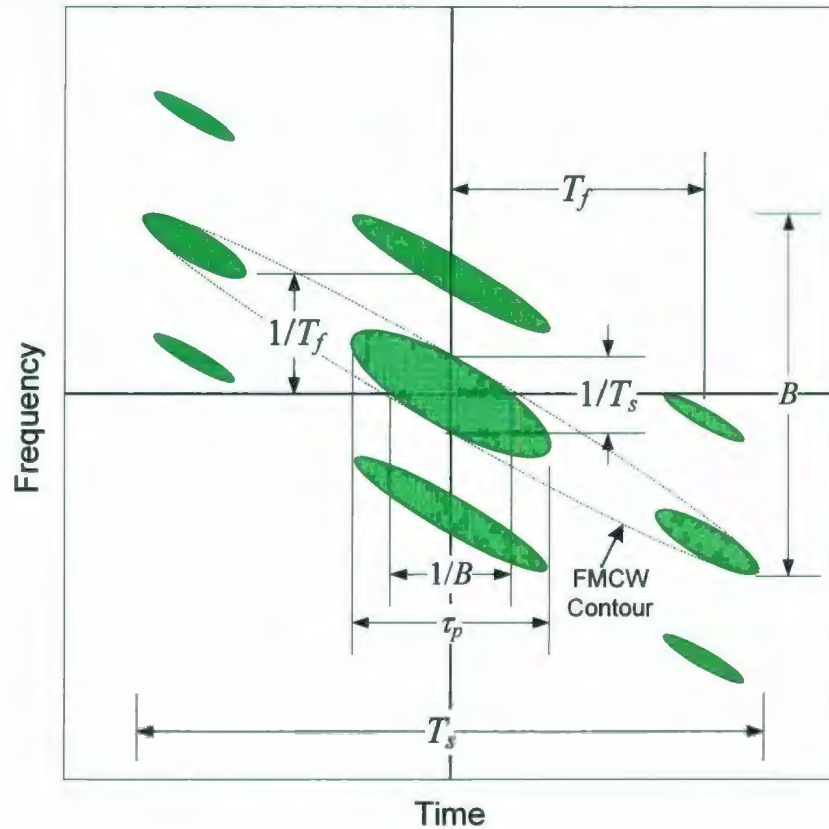


Figure 3-9: Generalized SFM Contour Ambiguity Diagram

3.4 Signal Orthogonality in SFM

As illustrated in the previous section, the waveform parameters affect the ambiguity response associated with the waveform. The pulse repetition period does not alter the shape of the ambiguity surface—instead it *scales* the ambiguity surface such that the velocity resolution and unambiguous range increase for longer T_f . However, different combinations of τ_p and Δf will alter the *shape* of the sidelobe structure. It is observed that when $\Delta f = 1/\tau_p$, or equivalently, when the frequency spacing equals the bandwidth of each pulse, the ambiguity surface provides monotonically decreasing sidelobe peaks moving away from the main lobe in both time and Doppler frequency directions. The effects on

the ambiguity response resulting from various combinations of the three waveform parameters are examined below.

The relationship between each frequency component of an SFM waveform dictates the shape of the ambiguity surface. In particular, the preferred ambiguity surface results when the set of pulses making up a linear SFM waveform are a set of orthogonal functions. Orthogonality is a condition that exists between two functions when the cross-correlation, $R_{12}(\tau)$, of the two functions is zero at zero lag (or $\tau = 0$), as follows:

$$R_{12}(\tau = 0) = \int_{-\infty}^{\infty} g_1(t)g_2(t-\tau)dt \Big|_{\tau=0} = 0 \quad (3-7)$$

The i^{th} pulse in an SFM waveform is represented as follows:

$$s_i(t) = \exp(j2\pi f_i t) \cdot \text{Rect}\left(\frac{t}{\tau_p}\right) \quad (3-8)$$

For any two pulses in an SFM waveform, where $i=\{m, n\} \in \mathbb{Z}$, the cross-correlation is derived as follows:

$$\begin{aligned} R_{mn}(\tau = 0) &= \int_{-\infty}^{\infty} \exp(j2\pi f_m t) \cdot \text{Rect}\left(\frac{t}{\tau_p}\right) \cdot \exp[j2\pi f_n(t)] \cdot \text{Rect}\left(\frac{t}{\tau_p}\right) dt \\ &= \int_{-\tau_p/2}^{\tau_p/2} \exp[j2\pi(f_m + f_n)t] dt \end{aligned} \quad (3-9)$$

If $\Delta f = 1/\tau_p$, then $f_m = m/\tau_p$, and $f_n = n/\tau_p$. Therefore,

$$\begin{aligned}
R_{mn}(\tau = 0) &= \int_{-\tau_p/2}^{\tau_p/2} \exp\left(\frac{j2\pi(m+n)t}{\tau_p}\right) dt & (3-10) \\
&= \frac{\tau_p}{j2\pi(m+n)} \exp\left(\frac{j2\pi(m+n)t}{\tau_p}\right) \Big|_{-\tau_p/2}^{\tau_p/2} \\
&= \frac{\tau_p}{j2\pi(m+n)} (\exp[j\pi(m+n)] - \exp[-j\pi(m+n)]) \\
&= \frac{\tau_p}{\pi(m+n)} \sin[\pi(m+n)] \\
&= 0
\end{aligned}$$

Therefore, if $\Delta f = 1/\tau_p$, then the set of pulses making up the linear SFM waveform are mutually orthogonal.

The effects of orthogonality and non-orthogonality will be demonstrated by way of Example 2 below. For this example, all parameters are fixed, with the exception of the number of pulses (which in turn modifies the pulse repetition interval). The number of pulses is modified so that in one case it presents an orthogonal set of pulses within the waveform, and in other cases, it presents sets of non-orthogonal pulses within the waveform.

Example 2: Orthogonality in SFM Waveforms

T_s	10 s
τ_p	0.25 s
B	40 Hz
$\{N_p, T_f\}$	$\{(5, 2 \text{ s}), (8, 1.25 \text{ s}), (10, 1 \text{ s}), (12, 0.867 \text{ s})\}$

The following figures show the matched filter response (i.e., ambiguity response for $f=0$) for each case, along with a close up of the central responses and adjacent ambiguity responses.

Case 1: Figure 3-12 and Figure 3-16 illustrate the case where the pulses of the SFM waveform are orthogonal. Here, the central response comprises a single peak and the ambiguities are completely confined to low levels.

Case 2: Figure 3-11 and Figure 3-15 illustrate a case where the pulses of the SFM waveform are non-orthogonal and the frequency step is larger than is required for orthogonality. Here, the central response and the ambiguities contain significant artifacts (or peaks) that may confound target detection.

Case 3: Figure 3-13 and Figure 3-17 also illustrate a case where the pulses of the SFM waveform are non-orthogonal, but where the frequency step is smaller than is required for orthogonality. Here, the central response has no artifacts; however, artifacts are present in the ambiguity responses that may confound target detection.

Case 4: Figure 3-10 and Figure 3-14 illustrate an interesting case where by definition the pulses are indeed orthogonal. This waveform is derived from Case 2, where every second pulse is transmitted so that the frequency step is twice that of Case 2. Here, the ambiguity responses have no artifacts; however, two distinct sidelobes are present on either side of the main peak within the central response.

It is important to realize in this analysis that these responses are just a single slice, at $f=0$, of the complete ambiguity surface; nonetheless, the example illustrates the type of compromise that must be considered if utilizing non-orthogonal waveforms. Furthermore, this example is indeed particularly important for the case of stationary or slow-moving targets.

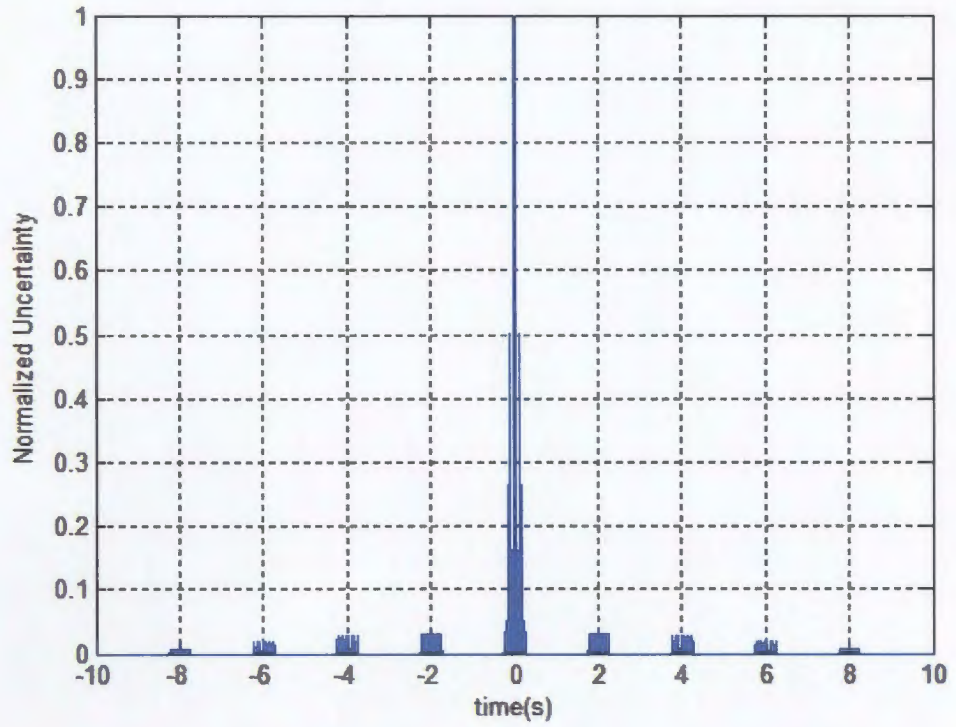


Figure 3-10: Response for Parameters $\{N_p=5, T_f=2 \text{ s}\}$

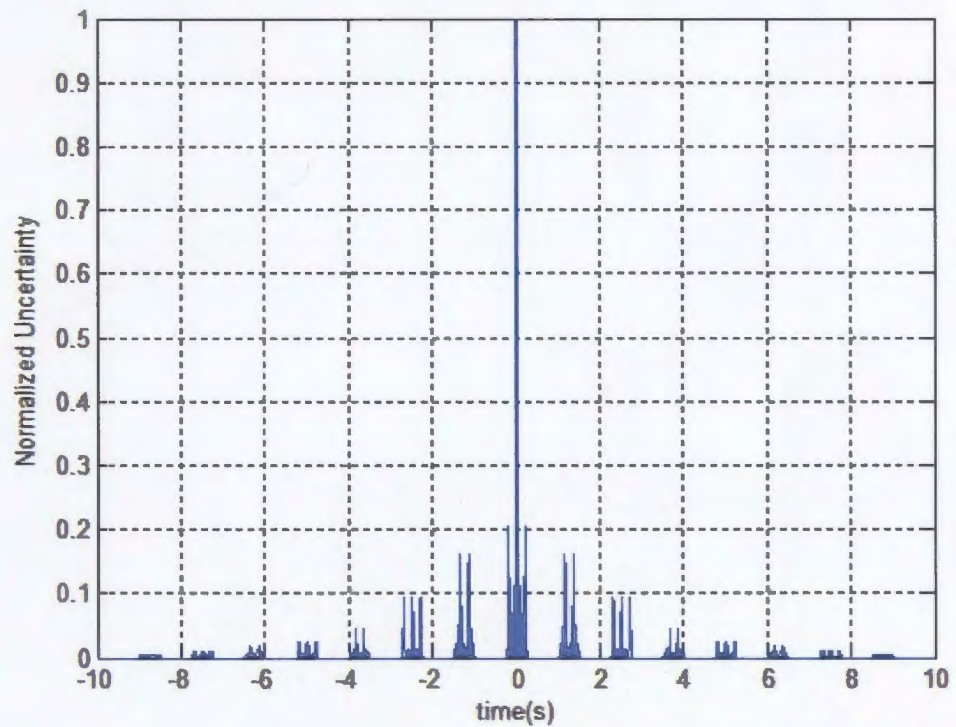


Figure 3-11: Response for Parameters $\{N_p=8, T_f=1.25 \text{ s}\}$

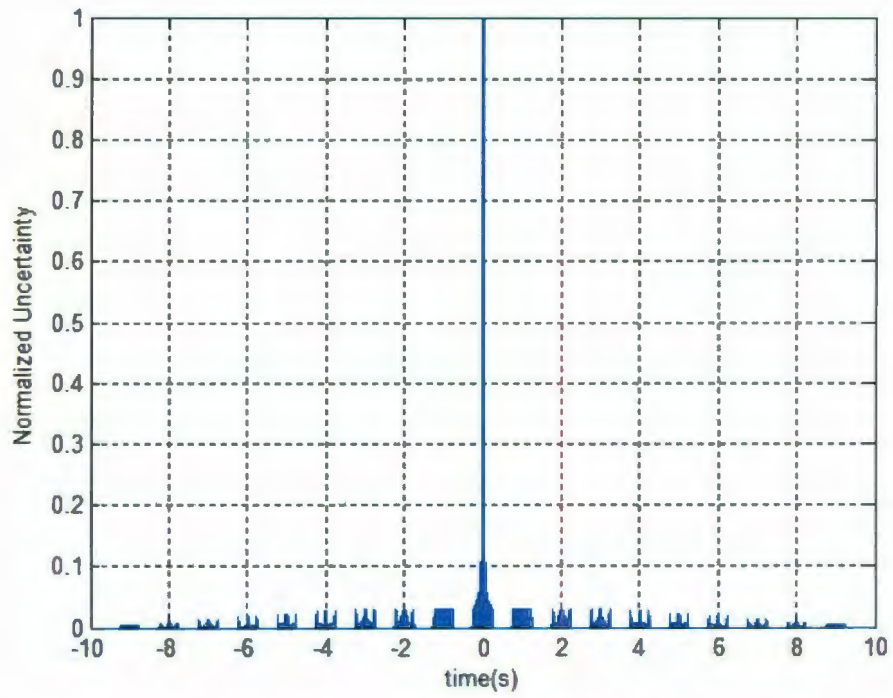


Figure 3-12: Response for Parameters $\{N_p=10, T_f=1 \text{ s}\}$

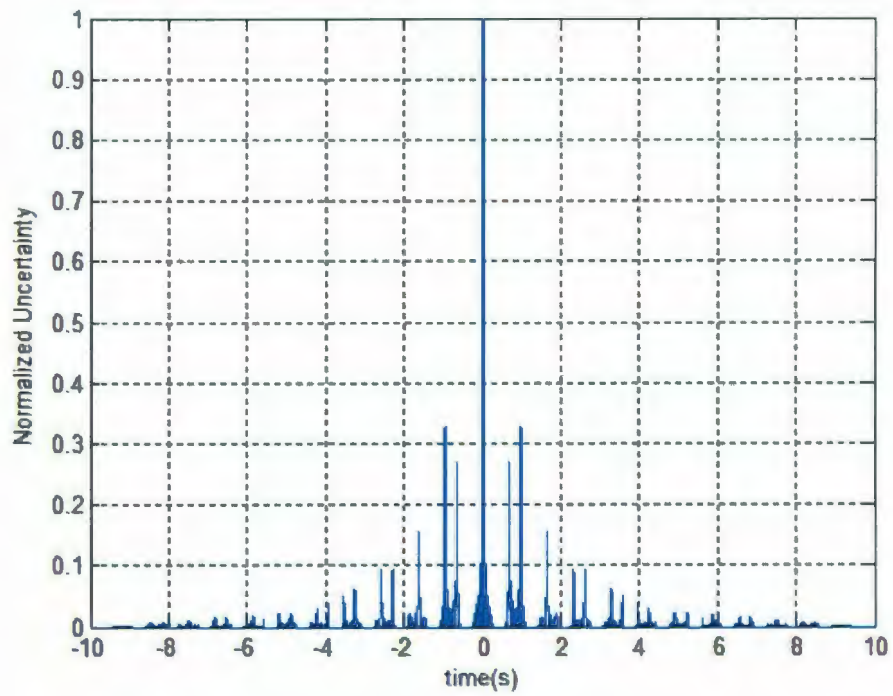


Figure 3-13: Response for Parameters $\{N_p=12, T_f=0.867 \text{ s}\}$

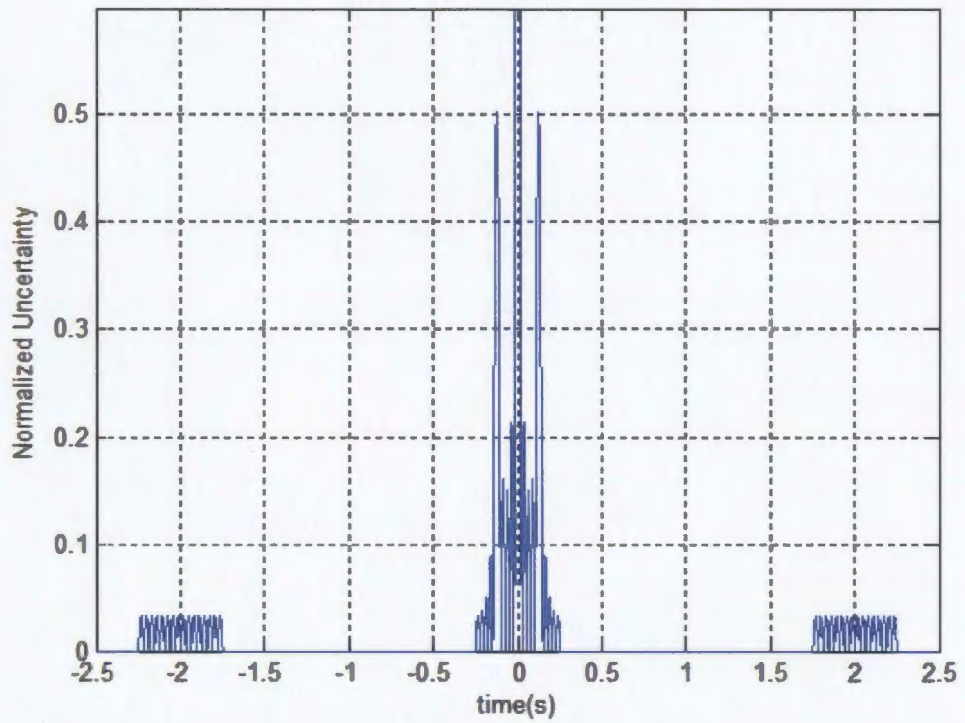


Figure 3-14: Response (zoomed) for Parameters $\{N_p=5, T_f=2 \text{ s}\}$

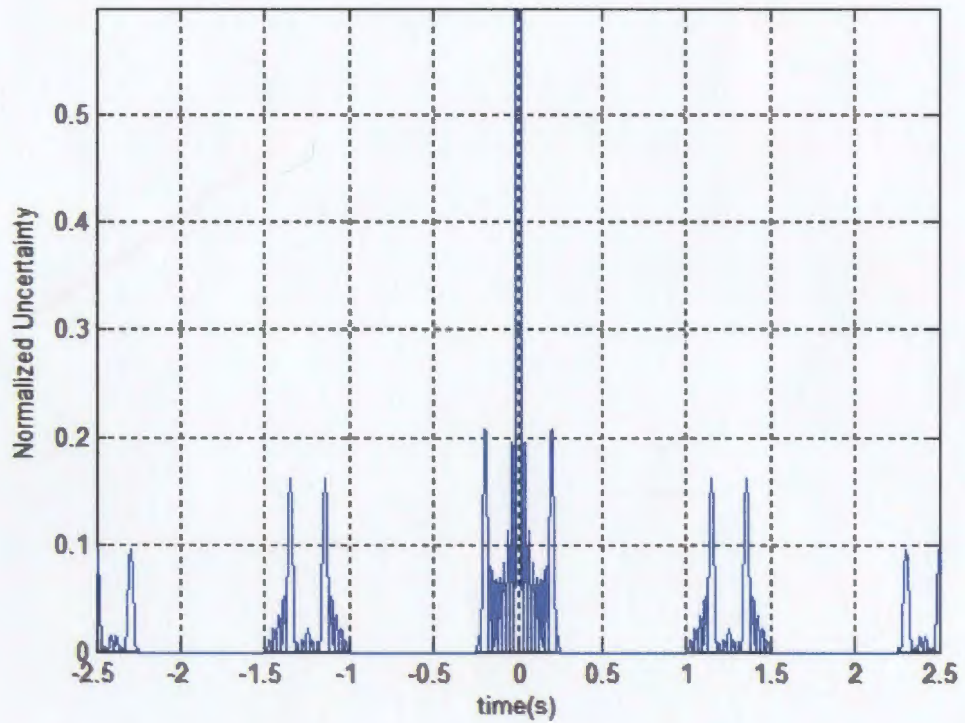


Figure 3-15: Response (zoomed) for Parameters $\{N_p=8, T_f=1.25 \text{ s}\}$

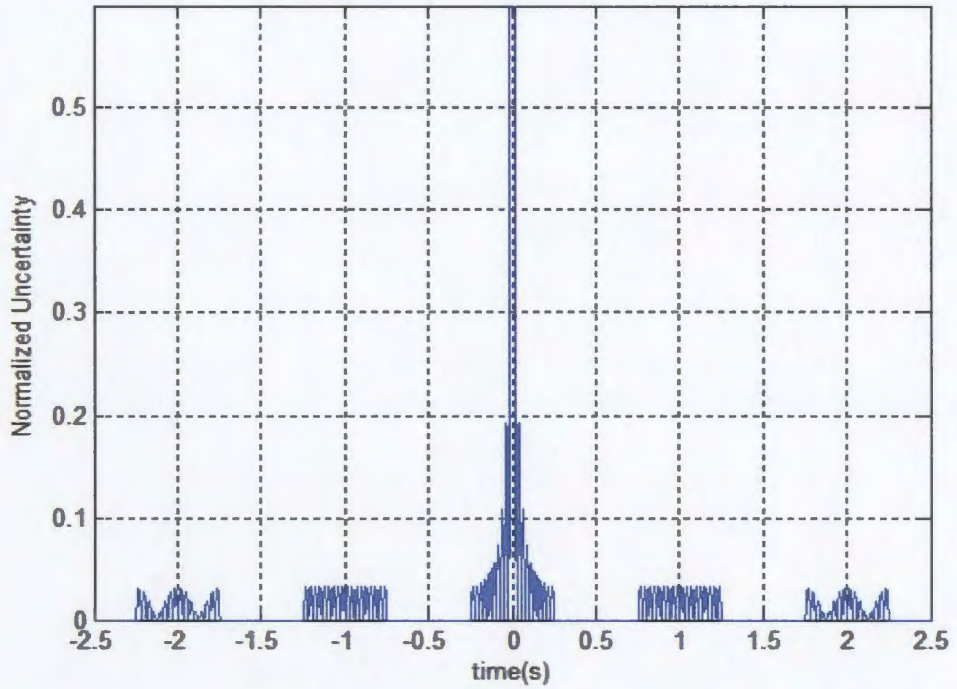


Figure 3-16: Response (zoomed) for Parameters $\{N_p=10, T_f=1 \text{ s}\}$

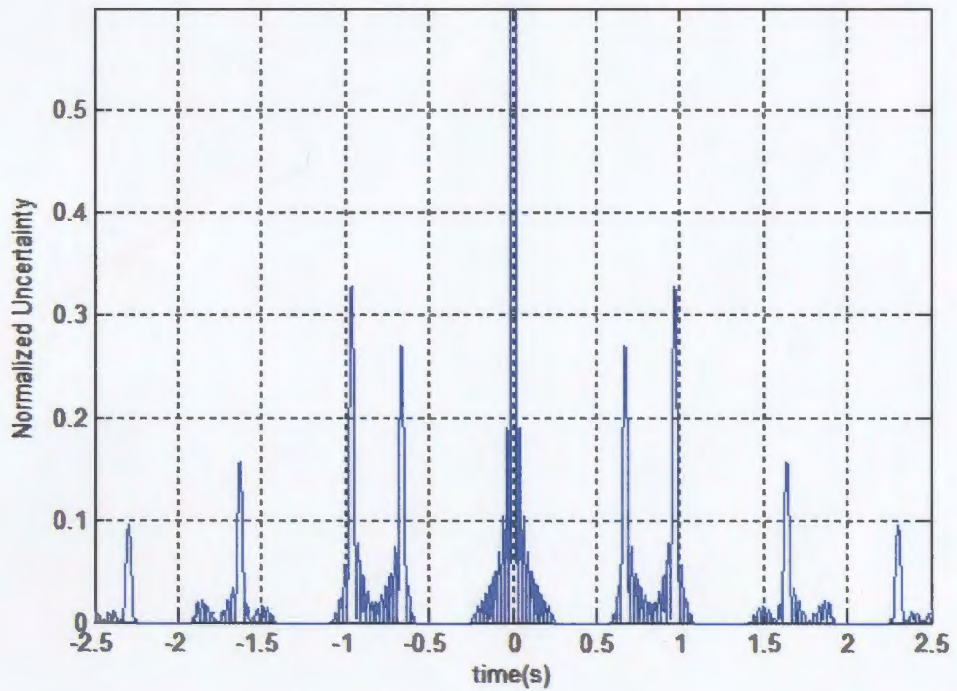


Figure 3-17: Response (zoomed) for Parameters $\{N_p=12, T_f=0.867 \text{ s}\}$

3.5 *Practical considerations for SFM*

For a typical application, the range and velocity ambiguities shown in the previous section are to be avoided. For instance, T_f should be chosen large enough so that the furthest expected target from the radar is within the unambiguous range. But as equation (3-6) dictates, the lengthening of the unambiguous range is done at the expense of shortening blind speed, so not all targets can be easily accommodated. In radar applications, the challenge is to design the waveform so that target ambiguities are outside the scope of expected targets, but that is not always possible—in these cases, other methods must be employed to identify the actual location and velocity of the target. These methods are beyond the scope of this thesis, but include, for instance, moving target indication (MTI) filtering.

Assuming a priori knowledge of the maximum detectable target range and velocity, then for real target detection, the signal return need only be assessed over the ranges and velocities of interest. To ensure that targets beyond these expected limits are not mistakenly aliased into view, various measures can be used; for instance, radiated power can be kept within a certain limit to ensure any reflections from targets beyond the maximum range are negligibly weak. Likewise, filters can be employed to reject any targets with radial velocities beyond the maximum velocity assessed by the radar processor. Once the operating limits are established, the primary interest is the central ambiguity response.

Some of the examples presented earlier are demonstrated using somewhat arbitrary signal parameters that are not necessarily useful in practical applications. In Section 3.3 for instance, a bandwidth, B , of 5 Hz would be very unusual, especially for microwave radar. While such examples serve well in understanding the theory, it is worthwhile to examine more realistic and practical signal parameters, as demonstrated by Example 3.

Example 3: Realistic Signal Parameters for SFM

T_s	5 ms
τ_p	2.5 μ s
T_f	100 μ s
B	20 MHz
N_p	50

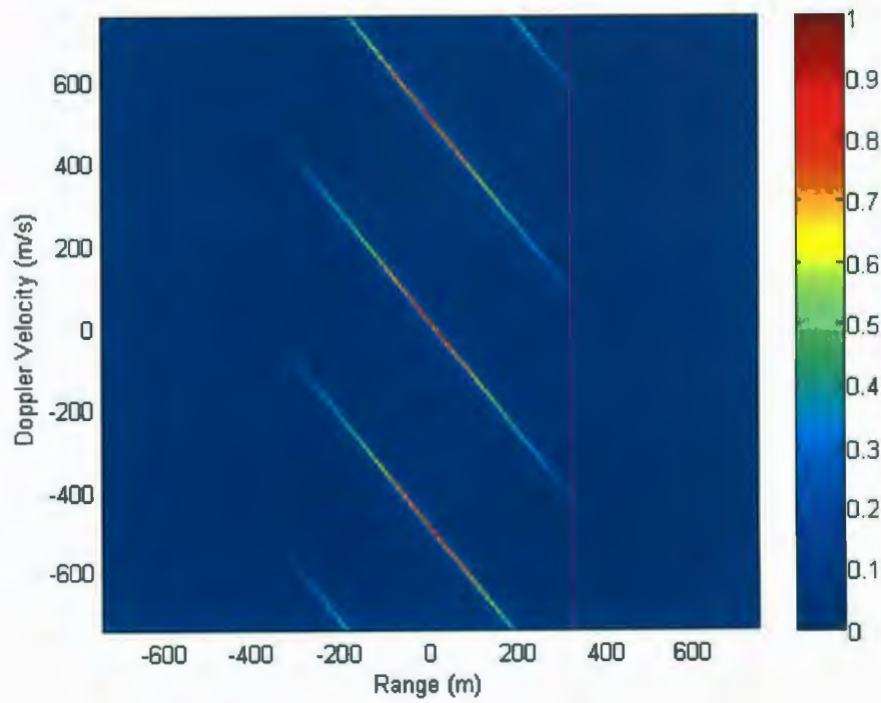


Figure 3-18: Ambiguity for Practical SFM

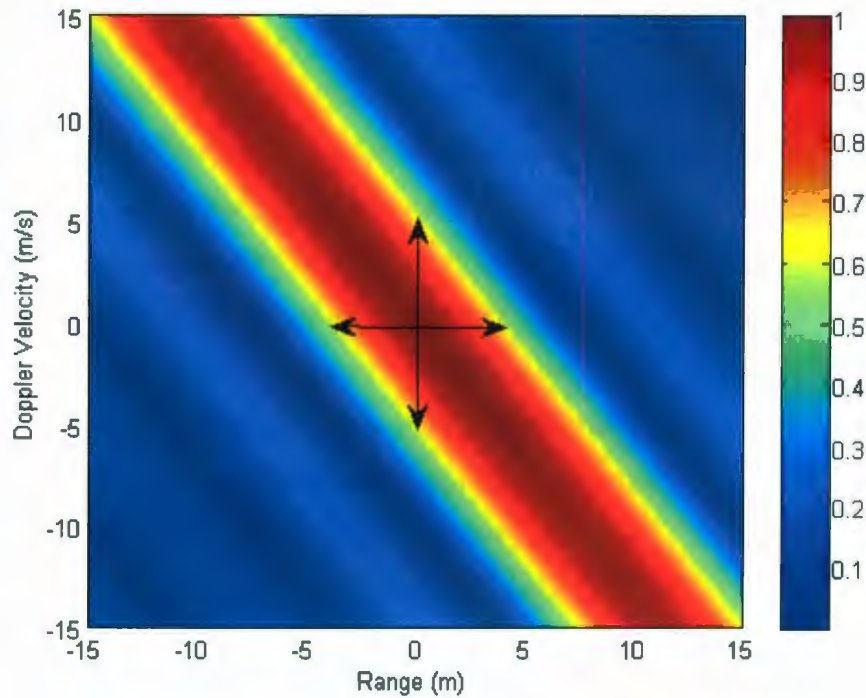


Figure 3-19: Ambiguity for Practical SFM - Zoomed

This example also plots the ambiguity surface with time and Doppler frequency translated into range and Doppler velocity respectively, by applying relations from Section 2.2.

Figure 3-19 is a zoomed rendering of the above example at the origin (zero range and zero Doppler). The arrows indicate the theoretical range and Dopplers resolutions; which, as the figure illustrates, is achieved in the simulation (by observing relative amplitudes of 0.5).

This example illustrates that for relatively short duration signals, achieving any useful information in the Doppler domain is impractical, because the extent of the ambiguity in this domain is large. However, once the bandwidth, pulse width and pulse repetition frequency are determined (and usually limited for a given application), the overall signal duration, which determines the Doppler velocity resolution, is fixed. Therefore, one must utilize a *multi-cycle waveform* to lengthen the waveform. This method comes with its own set of peculiarities and trade-offs—the discussion of the following sub-section.

3.6 Multi-Cycle SFM

The signal bandwidth may be limited for a number of reasons, including the physical makeup of the antenna, spectral allocations, and the microwave transceiver bandwidth. For fixed bandwidth, pulse repetition interval and pulse width, the overall length of a waveform, T_s , is also fixed, if orthogonality is to be maintained. In such a case, the Doppler resolution is thus limited. However, if the waveform is permitted to repeat itself, and many iterations of the waveform are processed for a given target return, then T_s is effectively extended, and the Doppler resolution is thereby reduced. Each iteration is referred to as a cycle; therefore, the composite waveform discussed below is referred to as a *multi-cycle waveform*, where the cycle time is denoted T_c . The behavior and quirks of multi-cycle SFM is demonstrated by way of Example 4.

Example 4: Orthogonality in SFM Waveforms	
T_c	50 μ s
τ_p	0.5 μ s
T_f	5 μ s
B	20 MHz
N_p	10
N_c	{1, 2, 5}

Figure 3-20 presents the point of reference for the example—the ambiguity response for a single-cycle waveform. Figure 3-21 shows the ambiguity response of the same waveform comprising two cycles. For a multi-cycle waveform, it is evident that the response lobes are divided into smaller segregated lobes. Figure 3-22 shows that introducing more cycles has the effect of further reducing the size of the segregated lobes; however, note that the quantity and position of these segregated lobes remain fixed. Finally, Figure 3-23 shows a magnification of the central response for the last case, whereby the sidelobes are clearly evident. More importantly, this figure reveals that the five-cycle waveform has one-fifth the Doppler resolution as the single-cycle case. This is consistent with equation (2-7), which relates the Doppler resolution to the overall waveform length.

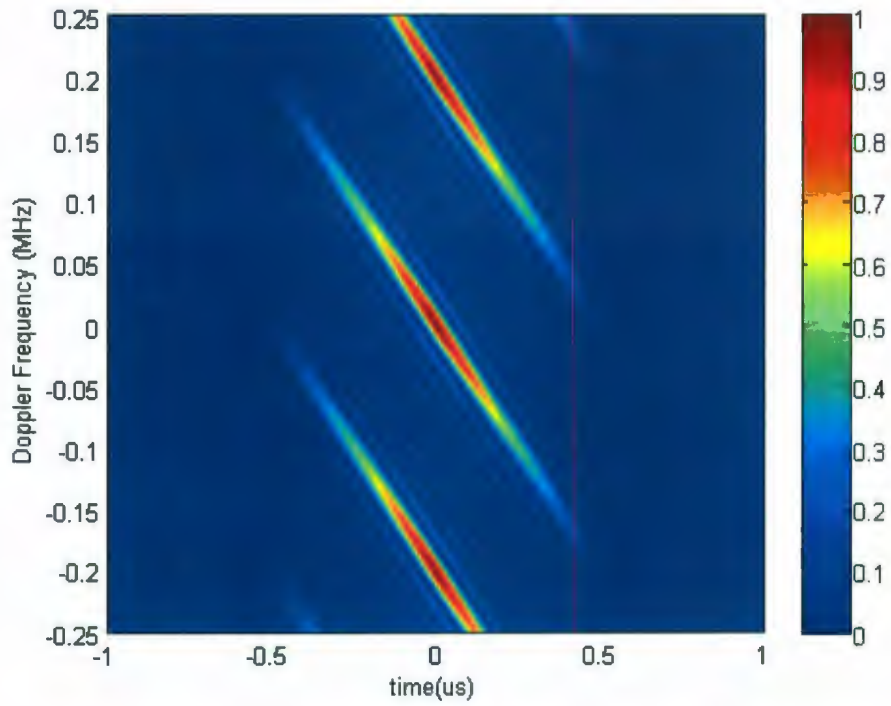


Figure 3-20: Ambiguity Response for Single-Cycle SFM Waveform

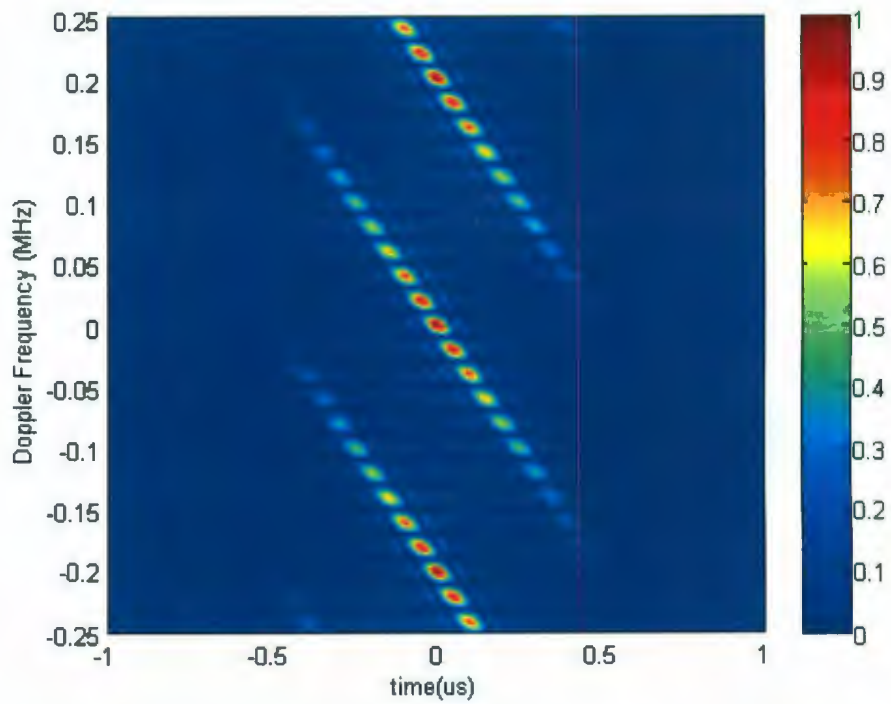


Figure 3-21: Ambiguity Response for a Two-Cycle SFM Waveform

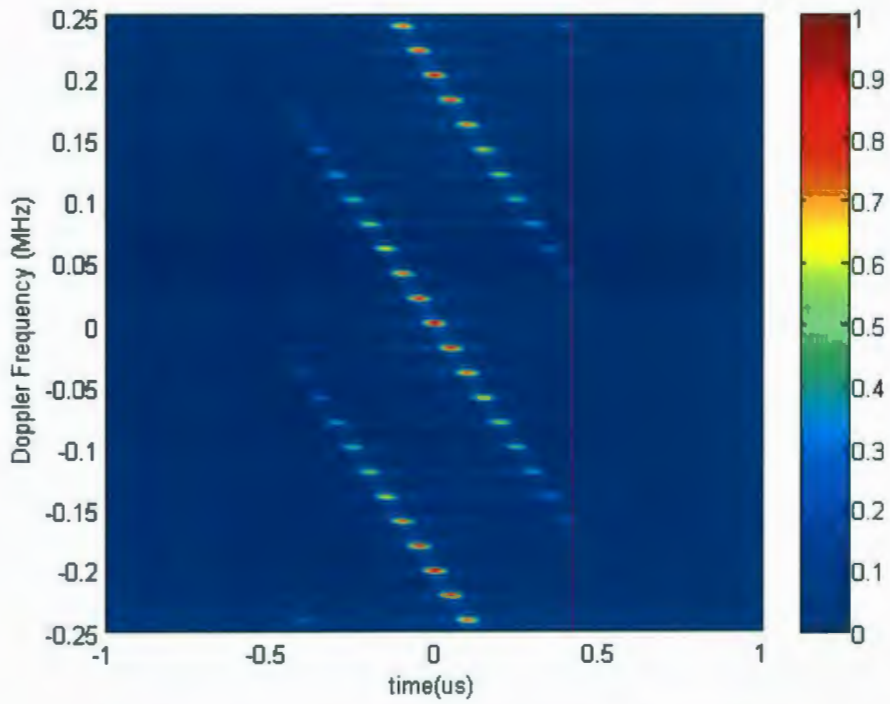


Figure 3-22: Ambiguity a Five-Cycle SFM Waveform

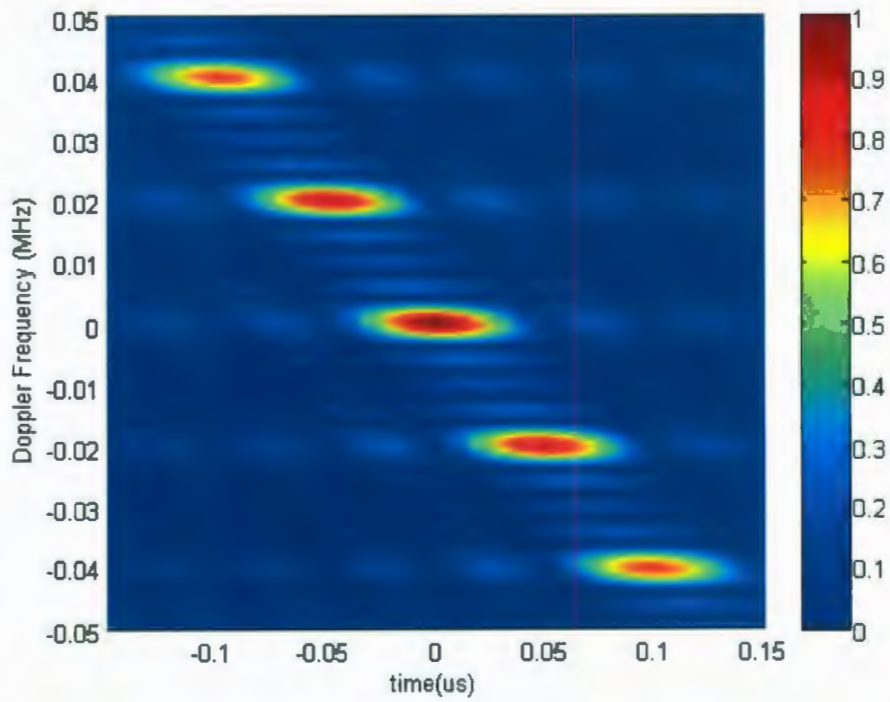


Figure 3-23: Ambiguity for a Five-Cycle SFM Waveform—Zoomed

A final observation in regards to the above example is that while the multi-cycle waveform improved the Doppler resolution, it did not change the temporal, or range resolution. This is because increasing the number of cycles does not increase the bandwidth; therefore, the range resolution remains constant.

As mentioned above, the segregated lobes are fixed in position. These positions are coincident with the area occupied by the response lobes for the single-cycle ambiguity and are spaced along the Doppler axis by the inverse of the cycle time, or $1/T_c$. From this observation, a generalized contour diagram for multi-cycle SFM can be created, as shown in Figure 3-24. In comparison to the single-cycle contour diagram (Figure 3-9), all of the parameters remain fixed with the exception of T_s and the newly introduced T_c (in boldface). Previously, for FMCW and single-cycle SFM, T_s equaled T_c ; however, here, T_s is N_c times longer than T_c . Clearly, in waveform design, one would be interested in choosing T_c so that the first Doppler ambiguity is outside any expected target velocity.

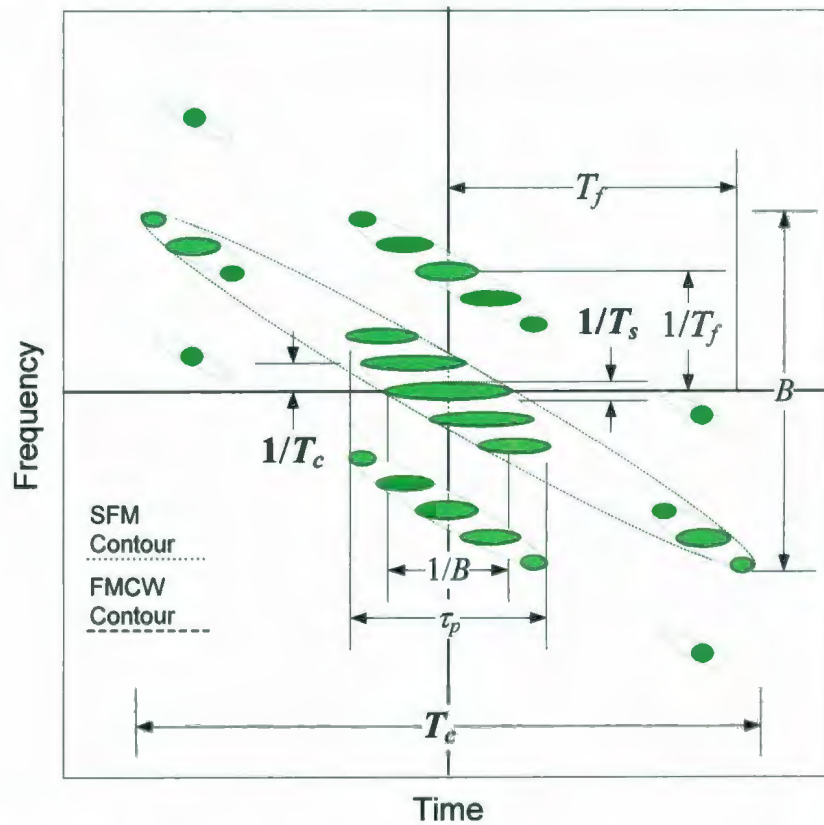


Figure 3-24: Generalized Multi-Cycle SFM Contour Ambiguity Diagram

3.7 Sidelobe Reduction in SFM

Earlier, in Section 2.8, a sidelobe reduction technique in the form of a Hamming window was introduced to demonstrate how such a technique will reduce sidelobes, but at the expense of widening the main response lobe. Such techniques are especially useful for the benefit of detecting small targets in the vicinity of large targets—these small targets would be otherwise obscured by the large target sidelobes. In this section, the concept is extended to an SFM waveform, for both single-cycle and multi-cycle cases.

In general, the removal of time-domain sidelobe artifacts requires windowing in the frequency domain, and removal of frequency (or Doppler) domain sidelobe artifact requires windowing in the time domain. However, because SFM constitutes a linear frequency stepping, applying a weight window across the entire signal, on a pulse-by-pulse basis, achieves both time-domain weighting and frequency-domain weighting (since each frequency component implicitly receives a different weighting) [20].

For SFM, a Hamming window is employed by sampling the window function such that the number of samples equals the number of pulses in the SFM waveform. Each window sample, or coefficient, is applied in a multiplicative manner across each SFM pulse. For a real radar, the window need only be applied to either the transmitted waveform or its reference used by the matched filter. In order to maximize the energy transmitted, the choice may be made to apply the window within the receiver. However, Levanon [20] indicates that mismatching amplitudes between the transmitted waveform and the receiver reference will have implications with respect to the resultant SNR. This subject is beyond the scope of this thesis; however, this factor should be carefully considered in the application of window functions.

Referring back to Example 4, if a Hamming window were introduced it would assume 10 (or N_p) coefficients, as illustrated in Figure 3-25. Figure 3-26 shows the resulting ambiguity response, where the expected sidelobe reduction is evident along with the associated widening of resolutions in both the temporal and frequency domains.

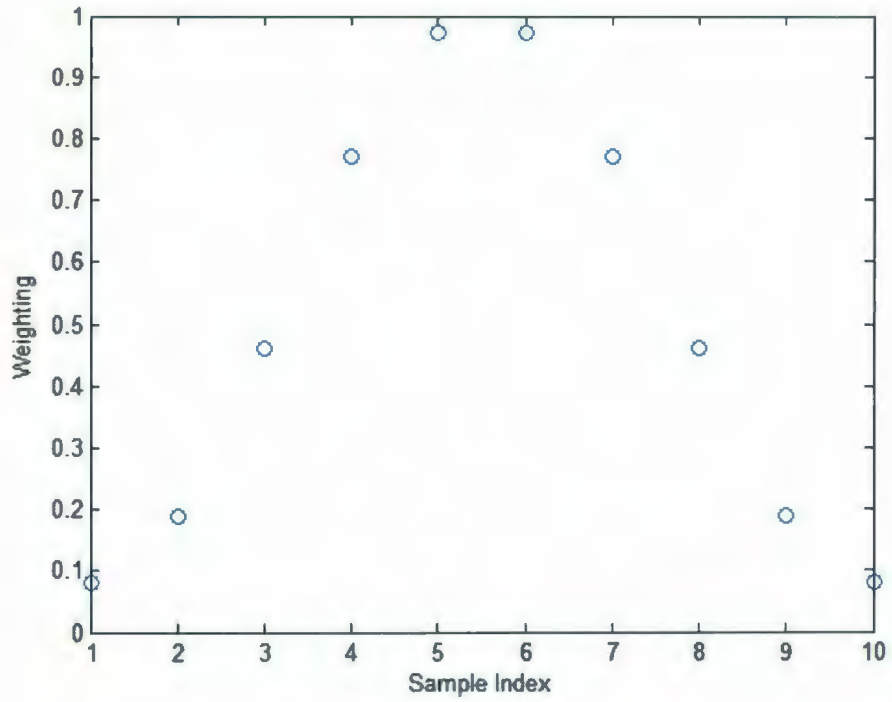


Figure 3-25: 10-Point Hamming Window

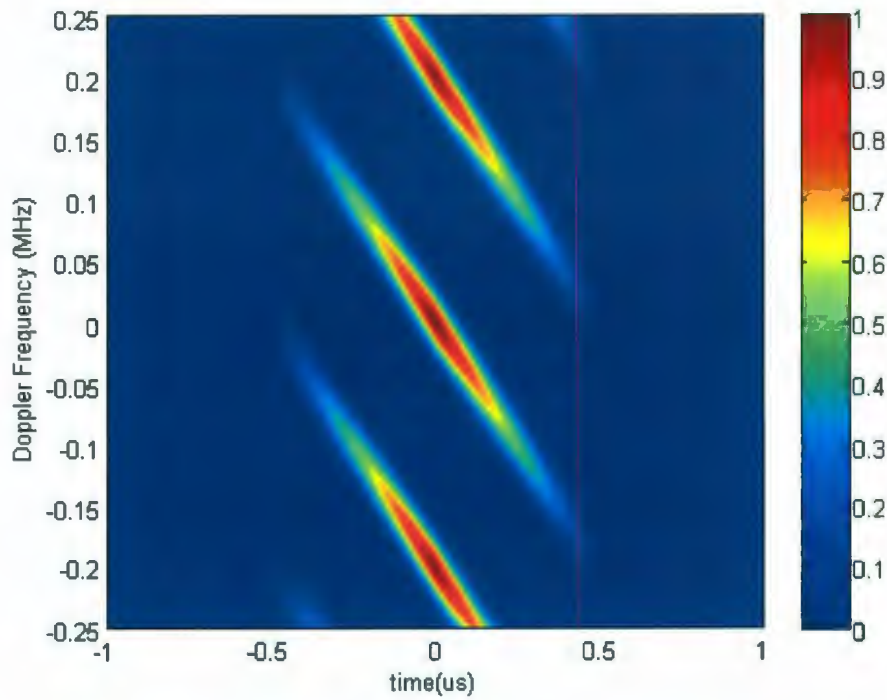


Figure 3-26: Ambiguity for Practical SFM w/ Hamming Window

The exact degree of widening of the main-lobe is dependent on the specific window employed; without such knowledge, a general rule of thumb states that the width of the main-lobe will increase by factor of roughly 1.3 through the application of a window [4].

For multi-cycle SFM, there are two manners in which a window function can be applied:

1. An $N_p * N_c$ -point window can be applied across the entire waveform (time domain dominant window).
2. An N_p -point window can be repeatedly applied across N_c cycles (frequency domain dominant window).

These two approaches are illustrated in Figure 3-27.

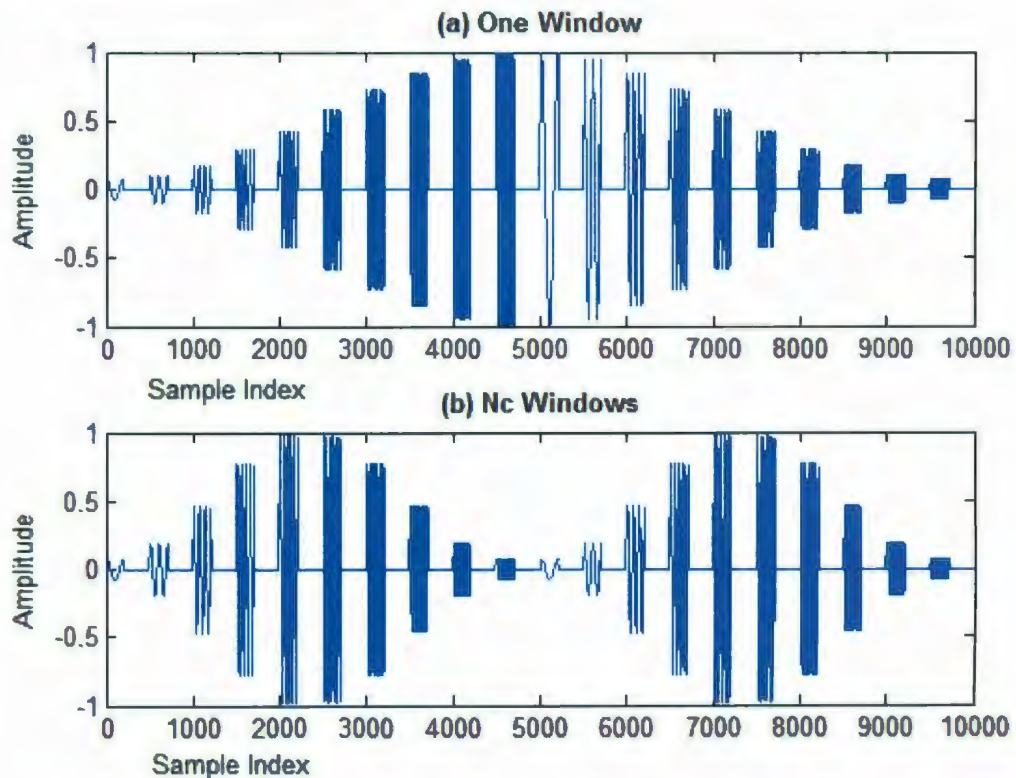


Figure 3-27: Application of Hamming Window to Multi-Cycle Waveform

Consider first Figure 3-27(a). In this case, the weighting is not consistent from cycle to cycle on a per frequency basis. However, the window is consistent over time. Therefore, this is a time-domain dominant window. As time domain windowing provides a reduction of sidelobe artifacts in the frequency domain, it is to be expected that this

choice of multi-cycle window would perform well in the removal of frequency domain artifacts, but not perform well in the time domain. This hypothesis is supported by the simulation result shown in Figure 3-28, which is a repeat of Example 4, but with a time-domain dominant window applied. Besides the removal of the frequency artifacts, it is observed that the main-lobe response is widened in the frequency domain, in comparison with Figure 3-23.

Next consider Figure 3-27(b). In this case, the weighting is consistent from cycle to cycle on a per frequency basis, but not consistent over time. Therefore, this is a frequency domain dominant window; so, the opposite effect of the previous case is expected. This hypothesis is supported by Figure 3-29 where the temporal artifacts are removed and the temporal resolution is widened in comparison with Figure 3-23.

While multi-cycle waveforms can be used to provide finer Doppler resolution, time and frequency domain sidelobe artifacts are not easily removed simultaneously. The determination of a window that might be employed to accomplish this, even partially, is outside the scope of the thesis.

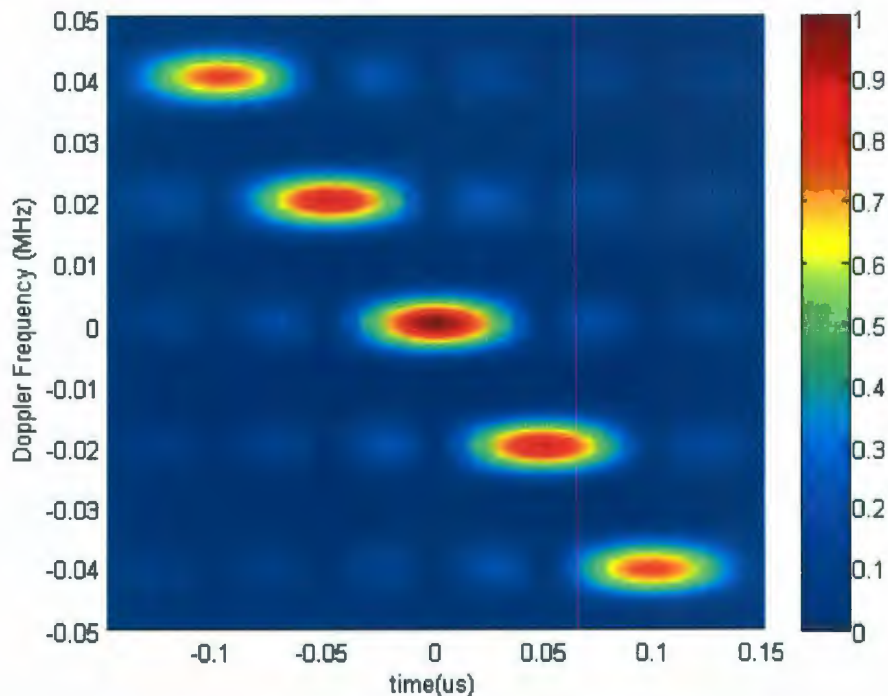


Figure 3-28: Multi-Cycle Ambiguity with Time Domain Dominant Window

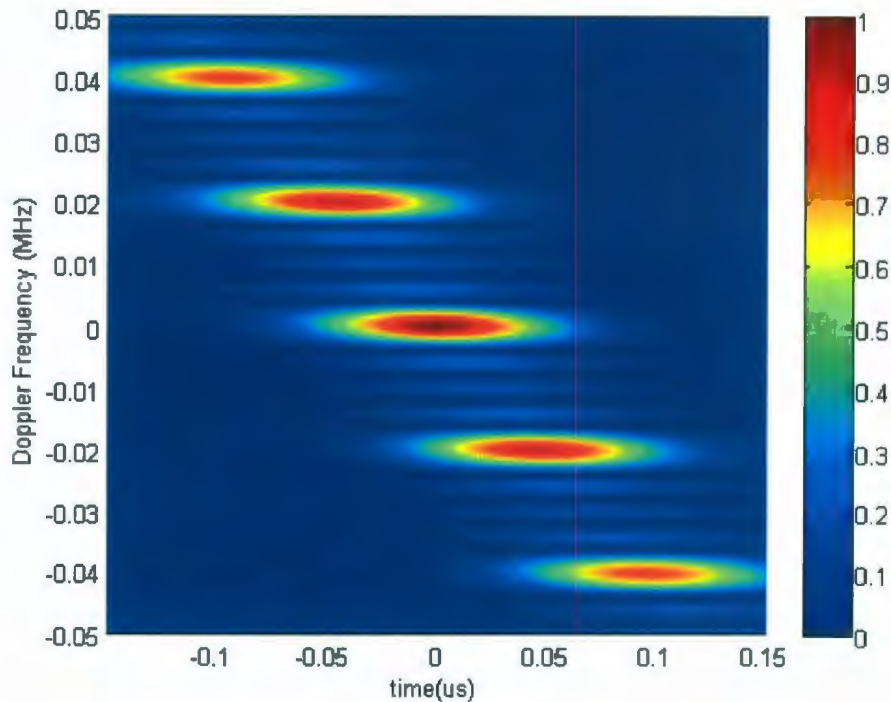


Figure 3-29: Multi-Cycle Ambiguity with Frequency Domain Dominant Window

3.8 Isomorphic Matched Filter

For a given radar hardware architecture, the *instantaneous* signal bandwidth may be limited by either the analog bandwidth of the RF hardware, or the processing bandwidth of the radar processor—both of which are strongly influenced by design and/or production costs. To provide relatively large bandwidths when a design is limited in this respect requires a novel design. This section discusses an original derivation of an equivalent means of matched filtering for an SFM radar signal that operates on a wideband signal, but on smaller portions of bandwidth at a time.

A brief background is first required. For FMICW, the echo is usually processed by mixing the return with the conjugate of the transmitted signal, with the resultant signal containing both frequency and Doppler information that is recovered using an FFT. Similarly, the echo from an FMICW signal can be processed by mixing the return with the conjugate of the un-gated transmit signal (FMCW equivalent). This results in many range ambiguities which can be resolved through a decomposition procedure described in [9]. Ideally a matched filter could be employed whereby the entire transmit sequence

is correlated with itself; however, this approach would be computationally intensive considering the duration of the sequence.

For SFM, the mixing approach described above will not work because the frequency is constant over short time intervals; therefore, a beat frequency will not be obtained from the mixing operation. Additionally, a matched filter approach will suffer the same computational burden discussed above. Therefore a method is desired that will generate an equivalent matched filter response without the computational requirements.

The signal processing approach to SFM portrayed below first converts the signal to baseband using a mixing operation, and then performs an operation on the baseband signal that results in an equivalent matched filter output. This operation essentially processes one pulse at a time, collecting and appropriately summing the individual results at the end of the complete SFM cycle. The approach has a tremendous advantage over matched filtering the entire signal since the bandwidth requirements of the receiver, including the analog-to-digital converter (ADC), are significantly reduced. This permits the use of a low-cost narrow-band receiver, and provides a reduction in the noise figure of the system. This section provides a detailed derivation, first starting with a single-pulse, single-frequency signal; then the concept is extended to the multi-pulse, multi-frequency SFM case.

3.8.1 Single Pulse Case (Pulsed Radar)

Begin with the following pulsed sinusoid:

$$s(t) = A \cos(2\pi f_o t + \phi(t)) \cdot \text{Rect}\left(\frac{t}{\tau_p}\right) \quad (3-11)$$

where

$$\phi(t) = 2\pi f_m t$$

f_m frequency offset (from carrier f_o)

τ_p pulse width

A amplitude

For $A=1$, the complex envelope representation of equation (3-11) is

$$u(t) = \tilde{s}(t) = \exp(j2\pi f_m t) \cdot \text{Rect}\left(\frac{t}{\tau_p}\right) \quad (3-12)$$

The complex envelope of the signal received from a target at a range corresponding to a time delay of τ_o is

$$r(t) = \exp[j2\pi f_m (t - \tau_o)] \cdot \text{Rect}\left(\frac{t - \tau_o}{\tau_p}\right) \quad (3-13)$$

3.8.1.1 Matched Filter

The cross-correlation of the transmitted and received waveforms is

$$\begin{aligned} m(\tau) &= \int_{-\infty}^{\infty} u(t)r^*(t - \tau)dt \\ &= \int_{-\infty}^{\infty} \exp(j2\pi f_m t) \cdot \exp(-j2\pi f_m (t - \tau_o - \tau)) \cdot \text{Rect}\left(\frac{t}{\tau_p}\right) \cdot \text{Rect}\left(\frac{t - \tau_o - \tau}{\tau_p}\right) dt \\ &= \exp(j2\pi f_m (\tau + \tau_o)) \cdot \int_{-\infty}^{\infty} \text{Rect}\left(\frac{t}{\tau_p}\right) \cdot \text{Rect}\left(\frac{t - \tau_o - \tau}{\tau_p}\right) dt \end{aligned} \quad (3-14)$$

The integral and integrand of equation (3-14) form the correlation between a rectangle function and a time-shifted version of the same rectangle function; which results in a triangular function. Therefore equation (3-14) may be re-written as

$$m(\tau) = \exp(j2\pi f_m (\tau + \tau_o)) \cdot \Lambda\left(\frac{\tau - \tau_o}{\tau_p}\right) \quad (3-15)$$

where

$$\Lambda\left(\frac{\tau - \tau_o}{\tau_p}\right) = \begin{cases} 0 & |\tau - \tau_o| \geq \tau_p \\ 1 - |\tau| & |\tau - \tau_o| \leq \tau_p \end{cases}$$

The signal, $m(\tau)$, is illustrated in Figure 3-30.

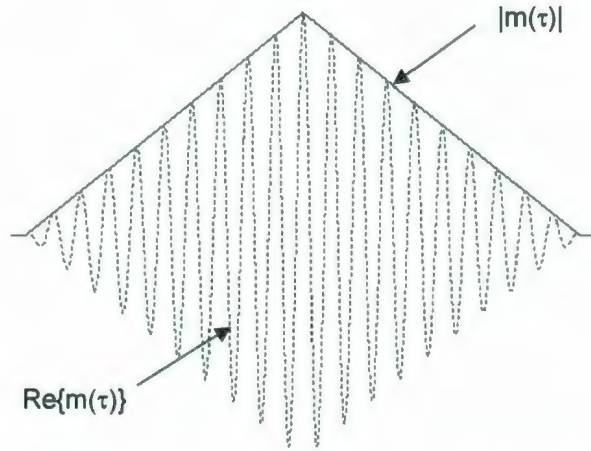


Figure 3-30: Matched Filter Output for Single Pulse

3.8.1.2 Isomorphic Matched Filter using a Mixer

The objective here is to recover equation (3-15) after a mixing operation has shifted f_m to baseband. To do this, the conjugate of the return is multiplied by an *un-gated* transmit signal – in this case a continuous wave (CW) signal, $u'(t)$, as given below:

$$\begin{aligned}
 m'(t) &= u'(t) \cdot r^*(t) = \exp(j2\pi f_m t) \cdot \exp(-j2\pi f_m (t - \tau_o)) \cdot \text{Rect}\left(\frac{t - \tau_o}{\tau_p}\right) \\
 &= \exp(j2\pi f_m \tau_o) \cdot \text{Rect}\left(\frac{t - \tau_o}{\tau_p}\right)
 \end{aligned}
 \tag{3-16}$$

By carefully considering equations (3-14) and (3-16), $m(\tau)$ can be written in terms of $m'(t)$. Given that

$$m'(t - \tau) = \exp(j2\pi f_m \tau_o) \cdot \text{Rect}\left(\frac{t - \tau_o - \tau}{\tau_p}\right)
 \tag{3-17}$$

then,

$$m(\tau) = \exp(j2\pi f_m \tau) \cdot \int_{-\infty}^{\infty} m'(t - \tau) \cdot \text{Rect}\left(\frac{t}{\tau_p}\right) dt
 \tag{3-18}$$

Essentially, equation (3-18) represents a very simple concept. The return envelope, obtained through mixing (this is why the conjugate is needed—to recover the envelope), is correlated with the transmit envelope to recover range information, while preserving phase information. Although a correlation operation is required, one of the elements is a rectangle; so this should be a lesser computational burden than with the matched filter at RF.

3.8.2 Multi-Pulse Case (SFM)

There are many physical means by which to generate an SFM signal. Each method can result in a different set of *starting phases*, ϕ_n , for each pulse. It doesn't matter what the starting phases are, as long as they are known and accounted for. A general complex envelope representation for an SFM signal, which will accommodate all methods of generation, is as follows:

$$u(t) = \sum_{n=0}^{N_p-1} \exp(-j\phi_n) \cdot \exp(j2\pi f_n t) \cdot \text{Rect}\left(\frac{t - nT_f}{\tau_p}\right) \quad (3-19)$$

The corresponding received signal from a target, with range delay τ_o , is

$$r(t) = \sum_{n=0}^{N_p-1} \exp(-j\phi_n) \cdot \exp(j2\pi f_n (t - \tau_o)) \cdot \text{Rect}\left(\frac{t - nT_f - \tau_o}{\tau_p}\right) \quad (3-20)$$

3.8.2.1 Matched Filter

The cross-correlation of the transmitted and received waveforms is

$$\begin{aligned} m(\tau) &= \int_{-\infty}^{\infty} u(t)r^*(t - \tau)dt \\ &= \int_{-\infty}^{\infty} \left\{ \sum_{n=0}^{N_p-1} \exp(-j\phi_n) \cdot \exp(j2\pi f_n t) \cdot \text{Rect}\left(\frac{t - nT_f}{\tau_p}\right) \cdot \sum_{n'=0}^{N_p-1} \exp(j\phi_{n'}) \cdot \exp(-j2\pi f_{n'} (t - \tau_o - \tau)) \cdot \text{Rect}\left(\frac{t - n'T_f - \tau_o - \tau}{\tau_p}\right) \right\} dt \end{aligned} \quad (3-21)$$

Equation (3-21) can be simplified by the knowledge that we do not need to consider the correlation of the transmitted and received waveforms over the entire range of τ , since the pulse rate, T_f , will be chosen so that all echo returns for each pulse will occur within T_f . Therefore, only the terms of each summation for which $n=n'$ need to be considered in the cross correlation. The subset of the matched-filter output of interest is

$$m_s(\tau) = m(\tau) \Big|_{\tau \in [0, T_f]} \\ = \int_{-\infty}^{\infty} \sum_{n=0}^{N_p-1} \left\{ \begin{array}{l} \exp(j2\pi f_n t) \cdot \text{Rect}\left(\frac{t - nT_f}{\tau_p}\right) \cdot \exp(-j2\pi f_n(t - \tau_o - \tau)) \\ \cdot \text{Rect}\left(\frac{t - nT_f - \tau_o - \tau}{\tau_p}\right) \end{array} \right\} dt \quad (3-22)$$

Exchanging the order of integration and summation, and combining exponential terms, the matched filter output is

$$m_s(\tau) = \sum_{n=0}^{N_p-1} \exp(j2\pi f_n(\tau_o + \tau)) \cdot \int_{-\infty}^{\infty} \text{Rect}\left(\frac{t - nT_f}{\tau_p}\right) \cdot \text{Rect}\left(\frac{t - nT_f - \tau_o - \tau}{\tau_p}\right) dt \quad (3-23)$$

This result is identical to equation (3-14) except that the cross-correlations for all n pulses are summed. The integral of equation (3-23) forms the correlation between a rectangle function and a time-shifted version of the same rectangle function; which results in a triangular function (the nT_f is lost because the same delay is in both rectangle functions). Therefore, equation (3-23) may be re-written as

$$m_s(\tau) = \sum_{n=0}^{N_p-1} \exp(j2\pi f_n(\tau + \tau_o)) \cdot \Lambda\left(\frac{\tau - \tau_o}{\tau_p}\right) \quad (3-24)$$

The resultant signal from equation (3-24) can take on many different forms, depending on the number of pulses and the frequencies chosen, as shown in Figure 3-31, Figure 3-32 and Figure 3-33.

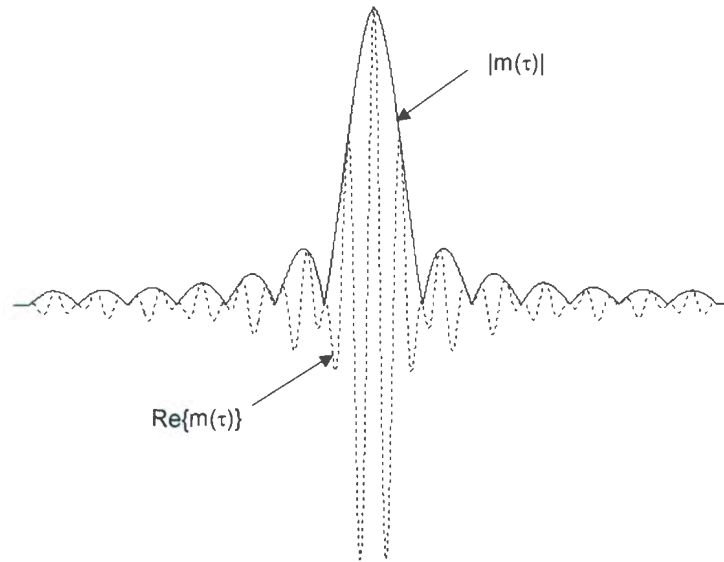


Figure 3-31: $m_s(\tau)$ for $N_p=7$, $\Delta f=1/\tau_p$

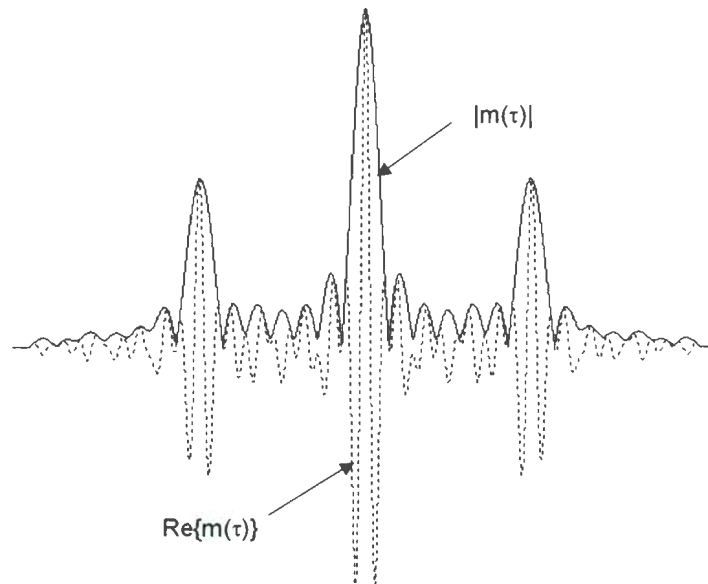


Figure 3-32: $m_s(\tau)$ for $N_p=7$, Δf =arbitrary

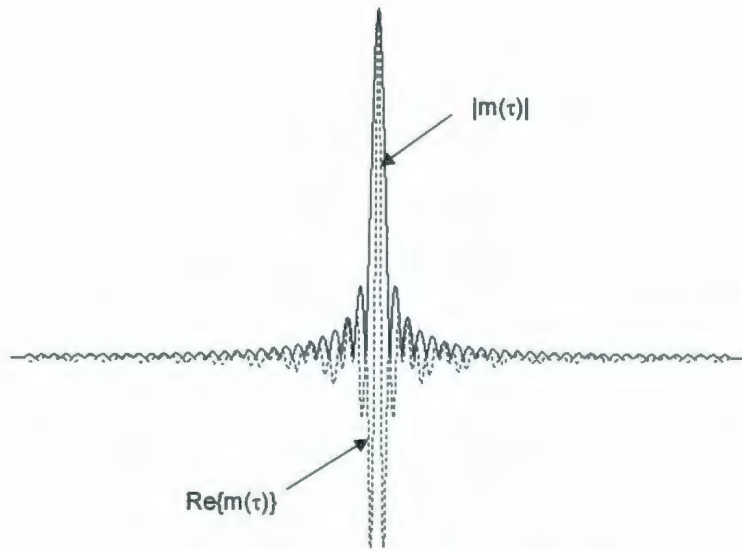


Figure 3-33: $m_s(\tau)$ for $N_p=29$, $\Delta f=1/\tau_p$

3.8.2.2 Isomorphic Matched Filter using a Mixer

Again, the objective here is to use an alternative approach whereby the received signal is mixed with some form of the transmit signal, resulting in a reduced bandwidth. Intuitively, if each pulse were multiplied by a CW signal of the same frequency and phase, then all pulses would be reduced to a single frequency; therefore, the chosen mixing signal is as illustrated in Figure 3-34, and represented by equation (3-25). This is analogous to the un-gated transmit signal, described for the single-pulse case.

$$u'(t) = \sum_{n=0}^{N_p-1} \exp(-j\phi_n) \cdot \exp(j2\pi f_n t) \cdot \text{Rect}\left(\frac{t - nT_f}{T_f}\right) \quad (3-25)$$

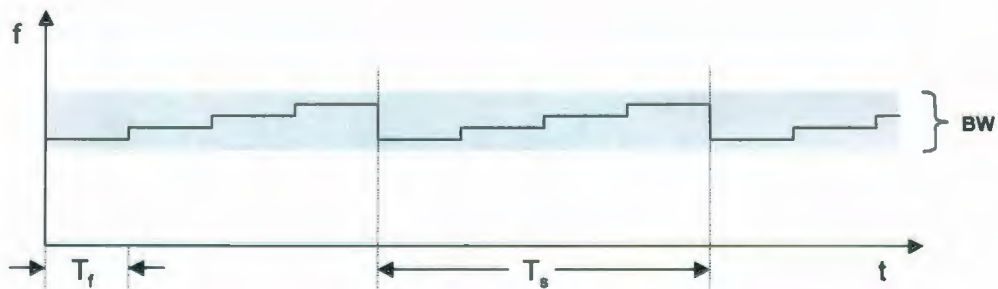


Figure 3-34: Mixing Signal

The mixer output is obtained by multiplying the signal in equation (3-25) with the complex conjugate of the echo return in equation (3-20):

$$m'(t) = u'(t) \cdot r^*(t) \quad (3-26)$$

It is assumed that no echos will occur beyond a range delay of T_f (i.e. $\tau_o \in [0, T_f]$). Therefore, only those product terms for which $n=n'$ are non-zero. The mixer output becomes

$$\begin{aligned} m'_s(t) &= m(t) \Big|_{\tau_o \in [0, T_f]} \\ &= \sum_{n=0}^{N_p-1} \exp(j2\pi f_n \tau_o) \cdot \text{Rect}\left(\frac{t - nT_f}{T_f}\right) \cdot \text{Rect}\left(\frac{t - nT_f - \tau_o}{\tau_p}\right) \end{aligned} \quad (3-27)$$

By carefully considering equations (3-23) and (3-27), $m_s(\tau)$ can be written in terms of $m'_s(t)$, as follows. First the delayed version of the latter is

$$\begin{aligned} m'_s(t - \tau) &= \sum_{n=0}^{N_p-1} \exp(j2\pi f_n \tau_o) \cdot \text{Rect}\left(\frac{t - nT_f - \tau}{T_f}\right) \cdot \text{Rect}\left(\frac{t - nT_f - \tau_o - \tau}{\tau_p}\right) \\ &= \sum_{n=0}^{N_p-1} \exp(j2\pi f_n \tau_o) \cdot R_1 \cdot R_2 \end{aligned} \quad (3-28)$$

Notice that R_1 is always equal to 1, for all $\tau \in [0, T_f]$; therefore, equation (3-28) can be simplified as follows:

$$m'_s(t - \tau) = \sum_{n=0}^{N_p-1} \exp(j2\pi f_n \tau_o) \cdot \text{Rect}\left(\frac{t - nT_f - \tau_o - \tau}{\tau_p}\right) \quad (3-29)$$

Therefore, the matched filter output, derived from the output of the mixer, is

$$m(\tau) = \sum_{n=0}^{N_p-1} \exp(j2\pi f_n \tau) \cdot \int_{-\infty}^{\infty} m'_s(t - \tau) \cdot \text{Rect}\left(\frac{t - nT_f}{\tau_p}\right) dt \quad (3-30)$$

This result is identical to equation (3-18) except that the same operation is repeated across N_p pulses and summed. Essentially, the mixing operation has converted each

segment to a common frequency range in order to reduce the required bandwidth of the receiver. Following correlation with the transmit envelope, each segment is then mixed with an exponential whose frequency is unique for each segment. All of the segments making up the entire transmit cycle are overlaid, frequency shifted, and summed in a manner that restores the original signal bandwidth.

4. SFM-Based Radar Design

Section 3.8 provided the rationale for exploiting wideband SFM on a narrowband hardware platform. This chapter provides a description of a hardware architecture that can realize this approach. The hardware design that is presented originated within the scope of research contracts executed by C-CORE under the technical lead of the author. However, insight gained through this research has identified certain areas of improvement. Where appropriate, these points are addressed below.

There are many aspects of detailed design associated with radar development. Some of these are generic across any radar design—for instance, cascade analysis of the receiver to determine parameters such as dynamic range and noise floor. These design issues are well-documented common practices. This chapter will focus solely on a couple of design issues that are particularly relevant to coherent SFM-based radar—namely coherency and phase noise. Subsequently, an overview of the radar prototype that was developed for the study is presented. Accordingly, the chapter will discuss the following elements:

1. the need and benefits of coherency;
2. phase noise;
3. a narrow-band coherent radar architecture well-suited to SFM; and,
4. processing algorithms.

4.1 *Coherency in Radar Design*

As described earlier, coherency can bring about many benefits to radar design—particularly in the area of resolution and SNR enhancement. Coherency in a radar design is a quality that enables phase comparisons to be made between the transmitted waveform and the received echo. These phase comparisons, accomplished through suitable processing, allow the radar to determine target attributes that are responsible for imparting phase artifacts, such as the radial velocity of a moving target. But what makes a radar coherent?

In order to accurately measure changes in phase, precise knowledge of the phase of the transmitted signal, or the oscillator from which it is derived, is first required over the

entire period of signal analysis. Secondly, through the up-conversion, down-conversion and detection processes, the radar must retain the phase information of the received signal in relation to the transmitted signal. To meet the first condition, the transmitted waveform must be synthesized from a highly stable reference oscillator with low phase noise. Once the transmitted signal is created, it will typically undergo several frequency translations in both the transmitter and receiver (up-conversion and down-conversion respectively). These frequency translations are accomplished in mixer devices fed by local oscillators (LOs). If these LOs are not derived from the same reference oscillator used to generate the transmitted waveform, then an unknown phase component will be added to the phase of the received waveform, thereby obscuring the desired phase information. Furthermore, the detection process might be preceded by an analog-to-digital converter (ADC). For a digitized signal, all processing is based on an assumed precise sample rate. If the sample clock for the ADC is not derived from the common reference discussed above, then the phase relationship between the captured signal and the transmitted signal is lost. So a coherent radar must have stable a reference oscillator, for the purposes of not only generating the transmitted waveform, but also from which all system clocks, including LOs and ADC sample clocks, must be derived¹.

Even when a common reference oscillator is employed, as described above, perfect coherence is not achievable. Loss of coherency can be attributed to many factors, many of which are addressed in detail by Scheer [4]. These include the following:

1. *Phase Noise*: The variation of phase of an oscillator relative to that of an ideal oscillator (pure sinusoid) is known as phase noise. Phase noise manifests itself in an LO's spectrum as energy in frequency bins adjacent to the LO frequency. For radar, this noise spectrum will be convolved in the frequency domain with an ideal target response such that the noise floor in the vicinity of the target is elevated—possibly obscuring weak targets in the vicinity of a strong target.

¹ For completeness, it should be noted that there exists a class of radar termed *pseudo-coherent* which essentially attempts to measure and track the phase of unstable waveform sources (such as the magnetron), for the purposes of making phase comparisons with the received waveform.

2. *Phase Non-Linearity*: Elements, such as filters, in a radar system will exhibit a non-linear phase response that will apply a variant time shift across different frequency components of a waveform. In such a case, the matched filter output of a receiver will degrade from the ideal case presented earlier. The result is a reduction in peak response and a perturbation, possibly elevation, of the sidelobe structure.
3. *Radar Motion*: Uncertain motion of the radar platform, both intended (as with an aircraft) and unintended (such as vibration), will cause phase deviations that if uncompensated will cause a degradation in the matched filter output. Intended motion, to some degree, may be readily accounted for through the use of technologies such as inertial navigation systems (IMS) or global positioning systems (GPS). There are also autofocus techniques where the radar data itself is used to estimate the phase error and refocus the radar image.

I/Q Errors: In order to measure phase, it is necessary to represent phase, which, in the digital domain, can only be accomplished with a complex representation. For a pure sinusoid, the complex form is represented as a rotating phasor of constant amplitude and constant angular speed (determining its frequency). The phasor, at any instant, may be decomposed into either magnitude and phase, or real and imaginary components. In the latter case, the components are referred to as *in-phase* and *quadrature* respectively, or I and Q. These components are orthogonal with respect to one another. I/Q may originate in either the analog domain, through an I/Q demodulator with two associated ADC channels, or in the digital domain from a single ADC channel and a transformation such as the Hilbert Transform. In the digital domain, errors may result from truncation effects; however, these are usually insignificant in modern computers that maintain a large number of significant digits. In the analog domain, the I/Q demodulator will not produce perfect I and Q owing to imbalances within the I/Q demodulator.

In the analog domain, I/Q signals are also used in conjunction with quadrature modulators, particularly in modern transceiver systems, for image

rejection in down-conversion and side-band rejection in up-conversion. Quadrature modulators can not produce perfect rejection of these mixing artifacts for the following reasons:

- a. An amplitude imbalance in I/Q will degrade the artifact rejection level. Typically, 30-40dB rejection is achievable with current technology.
 - b. A DC offset in both I and Q channels will elevate LO feed-through in the modulator.
 - c. If the I and Q channels are not perfectly orthogonal, then artifact rejection will degrade.
4. *Sample Jitter*: Most modern coherent radar will use digital processing to perform signal detection; therefore, a signal sampler, or digitizer, would be employed. Such sampling is subject to inaccuracies in the sample instant, known as sample jitter. Such inaccuracies may be brought about by jitter in the sample clock, or jitter that is inherent in the sample and hold circuitry within the analog-to-digital converter (ADC).
5. *Quantization*: When digitizers are employed within a radar design, a signal is quantized in both time and amplitude. In time, quantization is the effect of transforming a continuous time signal representation to a discrete time representation. Such sampling will cause frequency components of the continuous time signal to fold over to the frequency interval between zero and the sampling rate—a phenomenon known as aliasing. Amplitude quantization is the transformation of a continuous amplitude signal representation into discrete amplitude levels, as governed by the number of binary bits used in the representation. Both of the above types of quantization will have the effect of reducing the signal to noise ratio of prospective targets.

It is not the intention of this thesis to delve into great detail as to the quantitative performance degradation associated with a lack of, or reduction in, coherency. Instead, the purpose is to create awareness of the associated caveats in the design of coherent radar. However, the following section provides an example that is useful in providing the

reader insight into the type of investigations in respect to phase noise that may be warranted in coherent radar design.

4.2 Phase Noise Effects on SFM

There are many elements requiring in-depth analysis in any radar design—receiver noise figure, dynamic range, and sensitivity—to name a few. Scheer [4][21] provides excellent descriptions of coherent radar performance estimation in relation to device imperfections such as quantization, I/Q errors, and phase non-linearity, to name a few. One element of particular interest that can be analyzed in the context of specific radar signals is phase noise. Phase noise predominantly originates within the radar's frequency synthesizers, and is the most important characteristic of these devices [22]. This section examines phase noise in the context an SFM-based radar through a combination of analytical means and simulation. First a little background is required on how phase noise manifests itself in a radar and how it is generally characterized.

4.2.1 Phase Noise Background

Phase noise in coherent radar, is typically dominated by the phase noise characteristic of the reference oscillator from which all system clocks are derived. Other clock-generation subsystems, such as phase-locked-loops (PLLs), derive various system clocks from the reference oscillator; however, although these subsystems inherently generate phase noise, the dominant source of phase noise observed in their outputs, originates from the reference oscillator¹.

All clock generation subsystems effectively multiply the reference oscillator by some factor to achieve a desired system clock frequency. The phase noise of an oscillator is usually given by the one-sided phase noise power spectral density (PSD), $\mathcal{L}(f_m)$, where f_m is the frequency offset from the carrier, and phase noise side-bands are expressed as power levels relative to the carrier peak power; an example for an oven controlled crystal oscillator (OCXO) is shown in Figure 4-1, where the characteristic response is sometimes referred to as a *skirt*. Typically, this PSD is represented at discrete points in the

¹ In the case of a PLL, the reference oscillator dominates with the bandwidth of the loop filter; outside the filter, the inherent phase noise of the PLL dominates, but is relatively weak.

spectrum, or offsets from the center frequency, and tabularized as shown in Table 4-1. This is a reasonable approximation from which most relevant analyses can be performed on phase noise effects. The total phase noise is usually obtained by integrating the one-sided PSD across all frequencies, as described below. If the reference oscillator is multiplied by some factor, then all inherent frequency components of the oscillator are also multiplied by the same factor. This spreads the offsets further from the center frequency by the same factor, creating more area under the curve. Therefore, clock generation subsystems will increase the total phase noise, as a consequence of the multiplicative action. Typically, a factor of $20\log_{10}(N) + 3$ dB can be assumed.

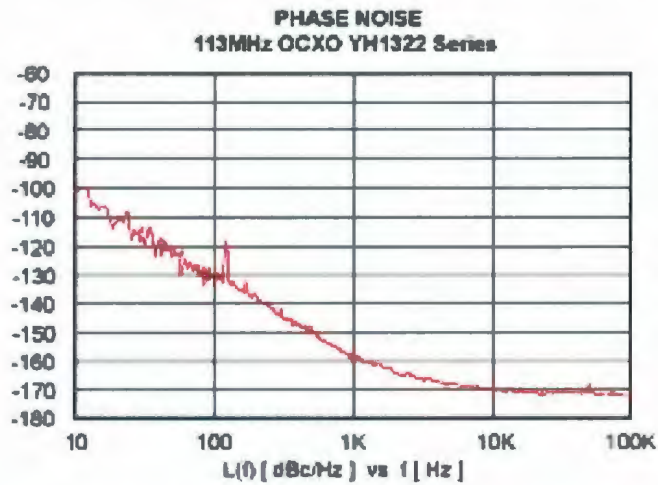


Figure 4-1: OCXO Phase Noise (© 2008 Greenray Frequency Control Solutions)

Table 4-1: Tabularized One-Sided Phase Noise PSD Corresponding to Figure 4-1

f_m (Hz)	$\mathcal{L}(f_m)$ (dBc/Hz)
10	-100
100	-130
1000	-159
10,000	-170
100,000	-172

In order to derive phase noise from the PSD, the relationship between the two must be first understood in order to make the conversion. Sinusoidal angle modulation with a rate of f_m can be represented as follows:

$$s(t) = A_c \cos[2\pi f_c t + \beta \sin(2\pi f_m t)] \quad (4-1)$$

where

A_c is the carrier amplitude, and

$\beta = \Delta f / f_m$ is the modulation index, where Δf is the maximum instantaneous frequency deviation from the carrier, f_c .

For small β (or narrow-band FM), equation (4-1) can be reduced to the following [10]:

$$s(t) \approx A_c \cos(2\pi f_c t) + \frac{A_c \beta}{2} \{\cos[2\pi(f_c + f_m)t] - \cos[2\pi(f_c - f_m)t]\} \quad (4-2)$$

This relationship shows that small-angle FM sinusoidal modulation gives rise to two delta function sidebands on each side of the carrier with amplitude $A_c \beta / 2$; therefore, β represents a proportion of the carrier amplitude, A_c . Since noise can be decomposed into an infinite number of these sidebands, a relationship between frequency deviation and PSD level for any arbitrary offset, f_m , is established as follows:

$$L(f_m) = \left(\frac{\beta}{2}\right)^2 = \left(\frac{\Delta f}{2f_m}\right)^2 = \frac{\Delta f_{rms}^2}{2f_m^2} = \frac{(\Delta\theta_{rms})^2}{2} \quad (4-3)$$

where

$$\mathcal{A}(f_m) = 10 \log_{10}\{L(f_m)\}$$

From the tabularized density, the total phase noise is computed by first performing a linear interpolation followed by an integration (in this case, computing the area of trapezoids), as shown in Figure 4-2 for the example in Figure 4-1. The approximation takes an average between two adjacent density values (in dBc/Hz) and computes the relative noise power over the corresponding bandwidth, as follows:

$$P_N = \left(\frac{L_2 + L_1}{2}\right) \text{dBc} / \text{Hz} + 10 \log_{10}(f_2 - f_1) \text{dBHz} \quad (4-4)$$

The above method is actually an approximation because the interpolation has been performed on a log-log scale. However, since the tabularized density is already an

approximate representation of the entire density, the approximate integration on the log-log scale will usually suffice.

The relative noise power is then translated into phase noise using the result from equation (4-3), as follows:

$$\Delta\theta_{rms} = \sqrt{2P_n} \times \frac{360}{2\pi} \text{ (}^\circ\text{rms)} \quad (4-5)$$

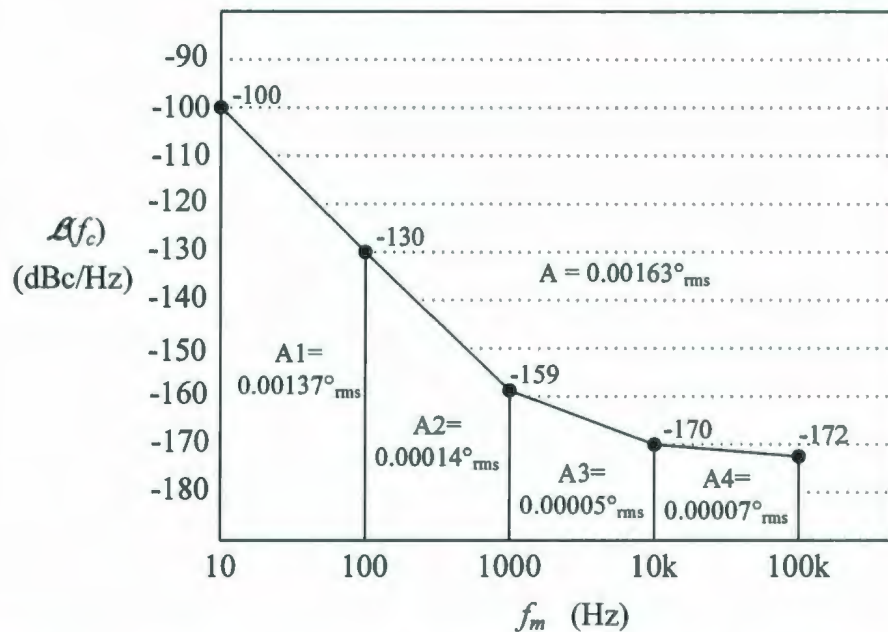


Figure 4-2: Computation of Total Phase Noise from Single-Sided PSD

To evaluate the effects of LO phase noise at the output of a mixer, consider that multiplication in the time domain infers convolution in the frequency domain. Therefore, through a mixer, the spectral characteristic of the LO is simply translated to the carrier at the output of the mixer, with the addition of any phase noise inherent in the input signal. A receiver path comprising several mixers in series will have a net phase noise effect resulting from contributions from each mixer—these add in a root-mean-square manner. Furthermore, an ADC in the receiver will also add phase noise inherent in its sample clock, as well as phase noise associated with aperture jitter. Therefore, the total phase noise in a receiver path is calculated as follows:

$$\phi_T = \sqrt{\phi_{LO1}^2 + \phi_{LO2}^2 + \phi_{LO3}^2 + \phi_{ADC_CLK}^2 + \phi_{ADC_JIT}^2} \quad (4-6)$$

where

ϕ_T = total cumulative phase noise

ϕ_{LOn} = phase noise of n^{th} LO

ϕ_{ADC_CLK} = phase noise of ADC sample clock

ϕ_{ADC_JIT} = phase noise representative of ADC aperture jitter

4.2.2 Phase Noise Simulation

To simulate the effects of oscillator phase noise on an SFM-based radar, it is meaningful to derive a phase noise characteristic from a realistic single-sided PSD as presented in the previous section, and apply it to an SFM signal in the model. The method of accomplishing this is outlined in the following steps (derived from [23]):

1. The one-sided PSD, $L(m)$, is interpolated over M equally spaced points, where, for a signal of size N , $M=N/2+1$ (even N), or $M=(N+1)/2+1$ (odd N).
2. The spectral shape of the phase noise is computed as $X(m)=\text{sqrt}(L(m)*dF)$, where dF is the frequency bin size determined from the sample rate and M .
3. The spectral shape is scaled by N to account for IFFT scaling ($1/N$) and multiplied, point-for-point, by a vector comprising additive white Gaussian noise (AWGN) of power 1.
4. The negative complex conjugate symmetrical portion of the noise spectrum is formed, and an IFFT is performed to generate a time series representation of the phase noise $\phi(n)$ (rendering a real signal, due to complex conjugate symmetry).
5. The signal, $s(n)$, is modified with the phase noise as follows:
 $s'(n)=s(n)*\exp(j\phi(n))$.

As expected, for

$$s(n)=\exp(j2\pi f^*n/F_s), s'(n)=\cos(2\pi f^*n/F_s+\phi(n))+j\sin(2\pi f^*n/F_s+\phi(n)).$$

Going back to the example in Section 3.7 and Figure 3-26, phase noise was applied in the manner described above in order to illustrate the resulting effect. The figures that follow are plotted on a dB scale in order to assess resultant SNRs for each phase noise

scenario. These plots are also scaled relative to the peak response in the original example (without phase noise), in order to make a relative comparison of compressed output levels. A table summarizing the parameters and results for each of the four scenarios is shown in Table 4-2. The degeneration of the main lobe and the enhancement of sidelobe artifacts are very evident in this simulation.

Table 4-2: Parameters and Results for Phase Noise Scenarios

<i>Parameter</i>	<i>Case 1</i>	<i>Case 2</i>	<i>Case 3</i>	<i>Case 4</i>
10Hz Offset (dBc/Hz)	n/a	-30	-30	-30
100Hz Offset (dBc/Hz)	n/a	-50	-40	-40
1kHz Offset (dBc/Hz)	n/a	-70	-50	-50
10kHz Offset (dBc/Hz)	n/a	-75	-60	-60
100kHz Offset (dBc/Hz)	n/a	-80	-70	-70
1MHz Offset (dBc/Hz)	n/a	-85	-80	-75
10MHz Offset (dBc/Hz)	n/a	-90	-90	-80
Phase Noise (rad _{RMS})	0	0.25	0.5	0.75
Relative Peak (dB)	0	-0.4	-0.7	-4.9
SNR (dB)	37	29	23	15

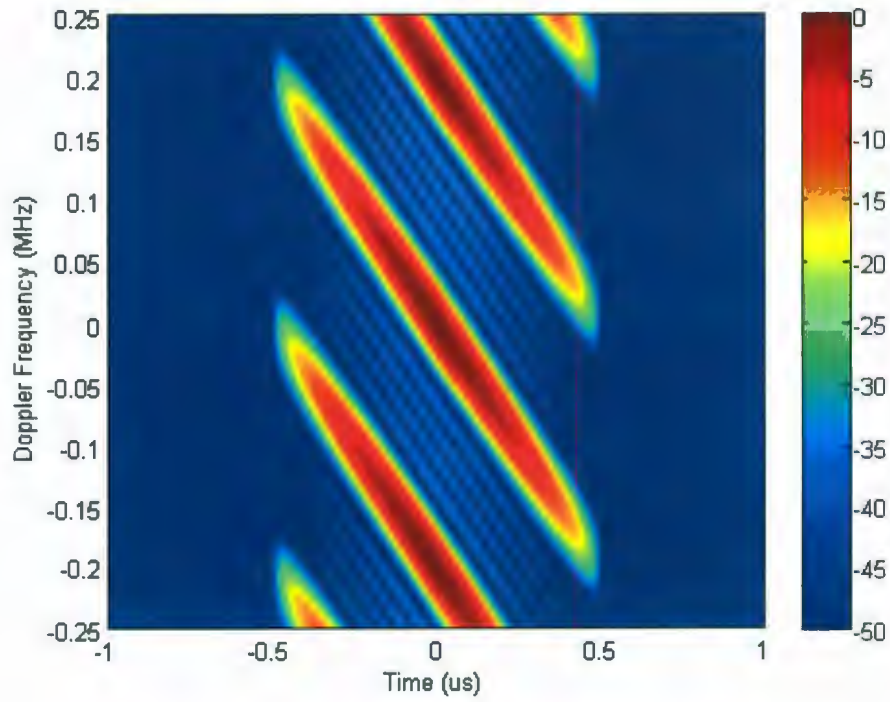


Figure 4-3: Ambiguity Response for Case 1: $\phi_N=0 \text{ rad}_{\text{RMS}}$

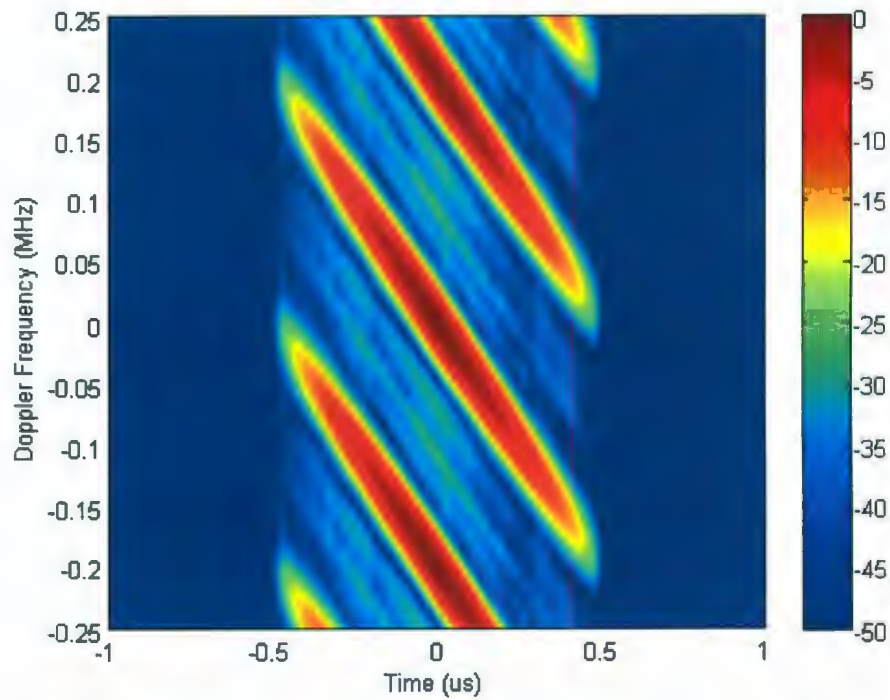


Figure 4-4: Phase Ambiguity Response for Case 2: $\phi_N=0.25 \text{ rad}_{\text{RMS}}$

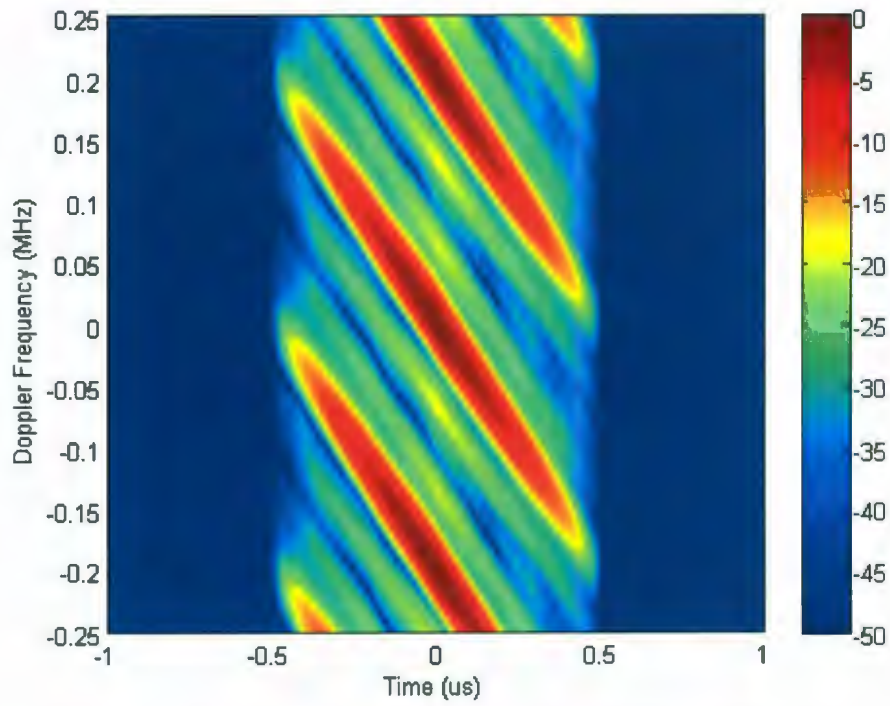


Figure 4-5: Phase Ambiguity Response for Case 3: $\phi_N=0.5 \text{ rad}_{\text{RMS}}$

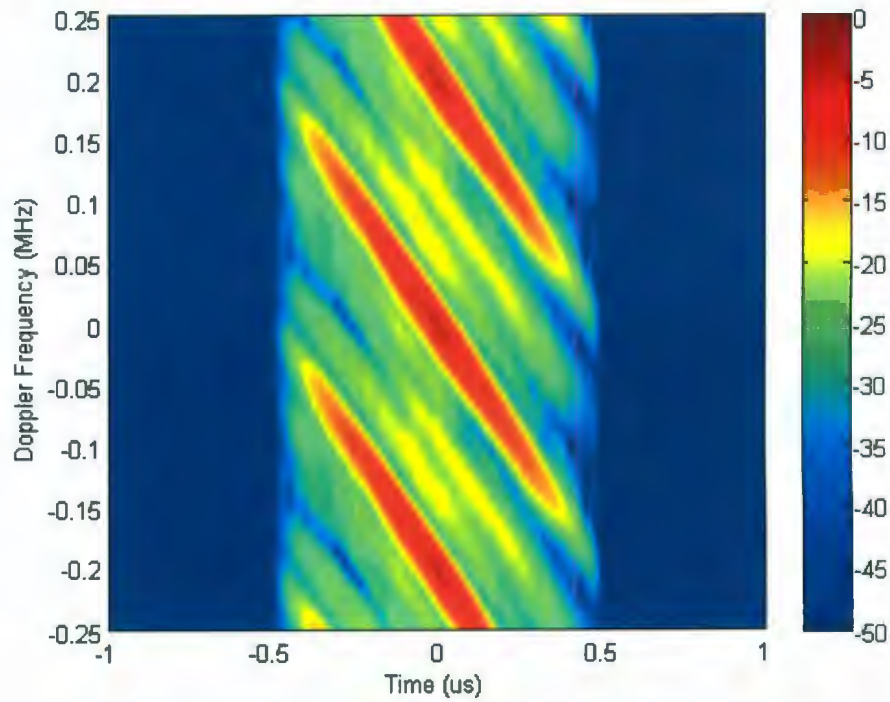


Figure 4-6: Ambiguity Response for Case 4: $\phi_N=0.75 \text{ rad}_{\text{RMS}}$

It is also interesting to look at the matched filter response, or a slice of the ambiguity response at $v=0$ m/s. The respective plots are shown in Figure 4-7 through Figure 4-10. These figures show that the width of the main-lobe does not appear to change as the level of phase noise is increased—only the peak response and the sidelobe artifacts are affected.

This simulation is only intended to be representative of the manner in which phase noise analysis may be carried out. Obviously, phase noise analysis could be carried out in much more depth by investigating various shapes and power levels of noise spectra as well as various waveform designs; however, such analysis is beyond the scope of this thesis.

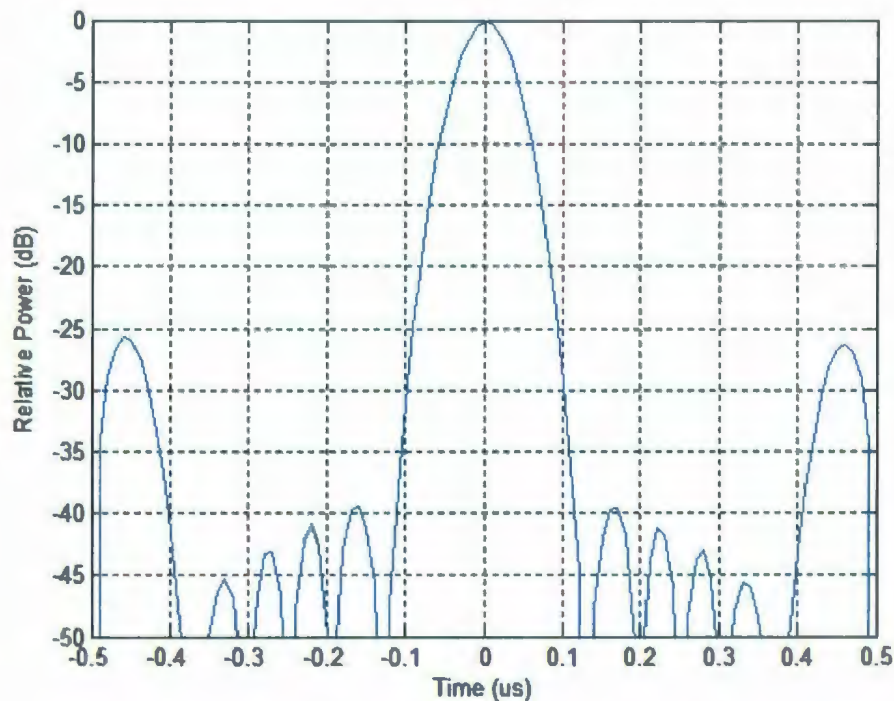


Figure 4-7: Matched Filter Response for Case 1: $\phi_N=0$ rad_{RMS}

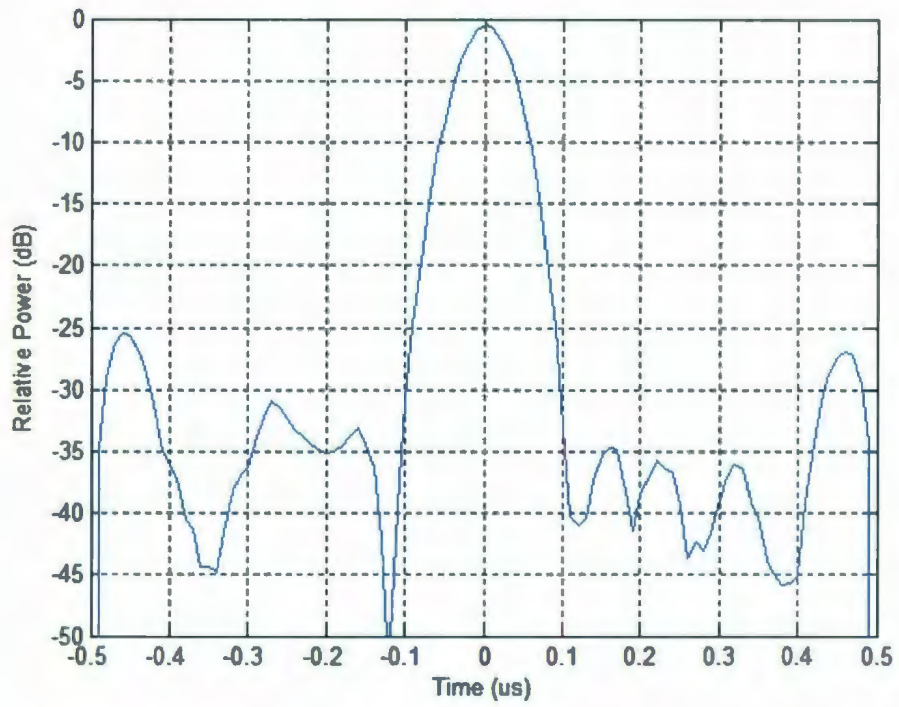


Figure 4-8: Matched Filter Response for Case 2: $\phi_N=0.25 \text{ rad}_{\text{RMS}}$

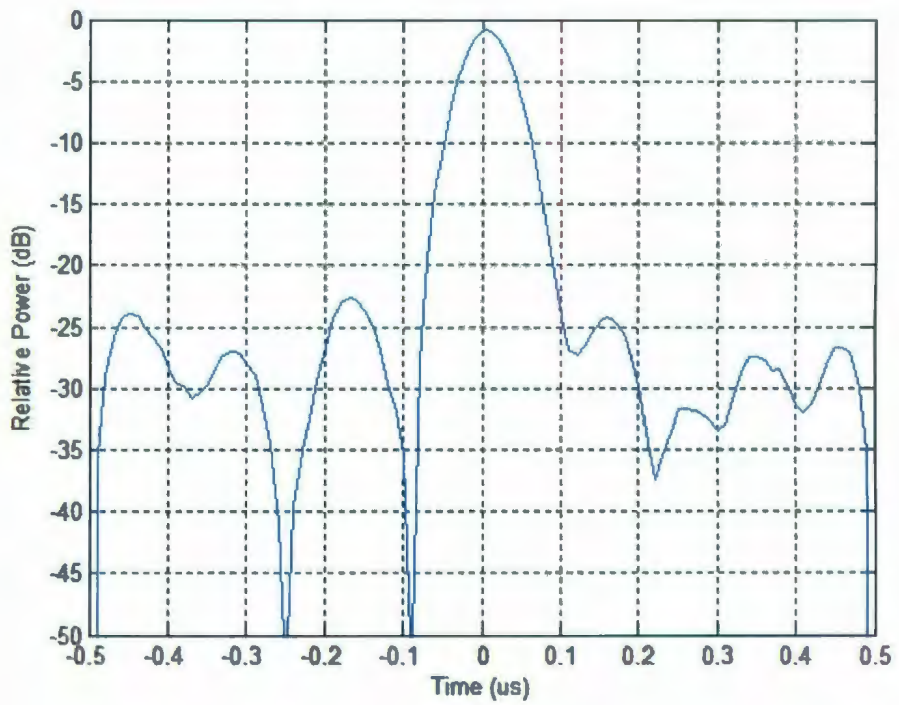


Figure 4-9: Matched Filter Response for Case 3: $\phi_N=0.5 \text{ rad}_{\text{RMS}}$

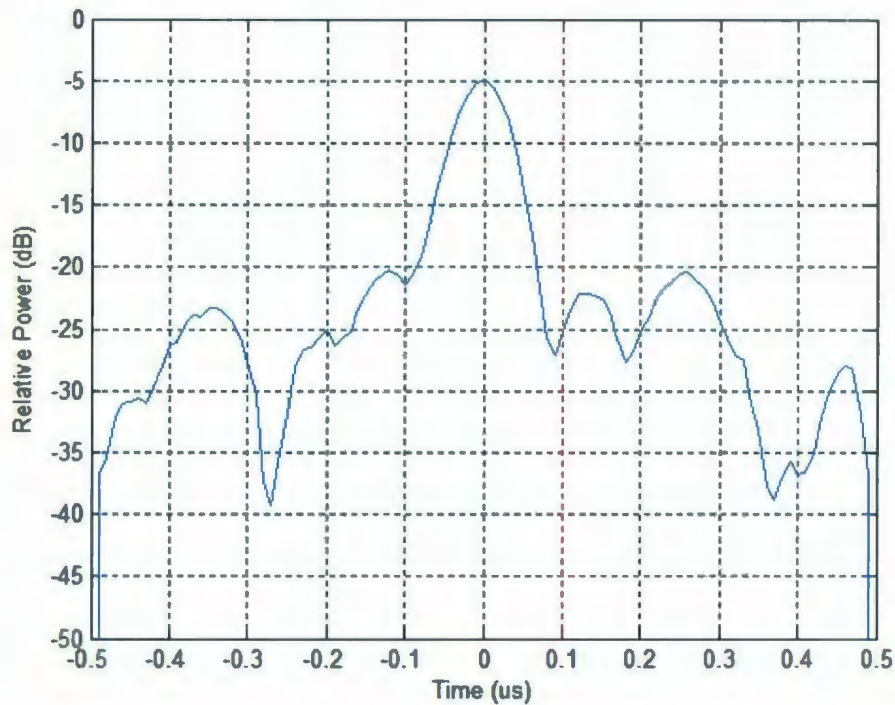


Figure 4-10: Matched Filter Response for Case 4: $\phi_N=0.75 \text{ rad}_{\text{RMS}}$

4.3 Narrow-Band Coherent Radar Prototype Hardware

A prototype coherent radar was designed at C-CORE in 2005—the hardware and signal processing components of which were designed by the author. This section presents a high level design of the prototype. In some cases, future design considerations are shown that have been derived from experience gained during development. The prototype was designed around an operating frequency of 2.4 GHz—conveniently chosen within the industrial, scientific and medical (ISM) band to take advantage of the license free nature of this band and also to avail of the wide range of device technologies readily available in the marketplace (e.g., cordless phones and wireless routers) that support RF development in this band¹.

¹ An early version of the prototype was in fact a dual-band radar operating at both S-band (2.4 GHz) and L-band (775 MHz); however, L-band was eventually abandoned in favor of S-band, as S-band has more commercial significance for marine radar.

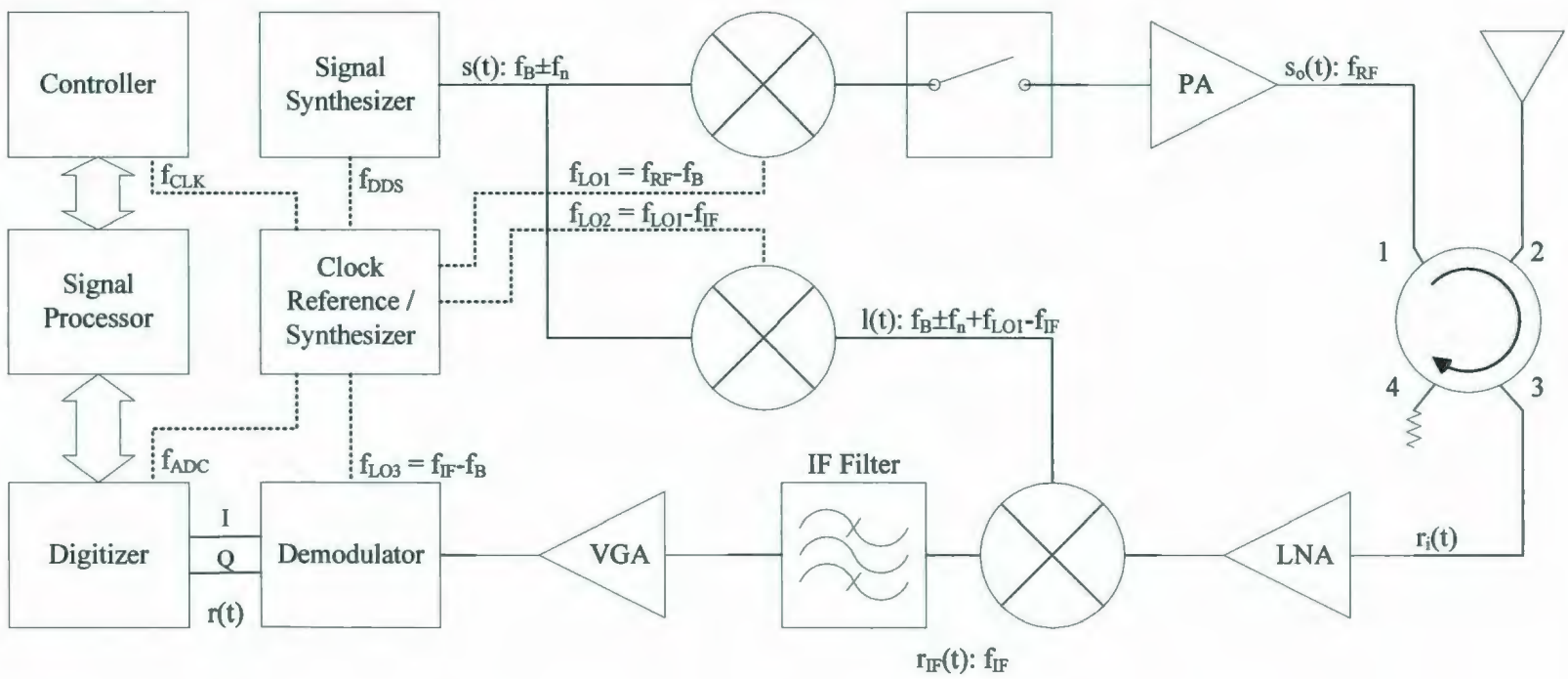
The narrow-band coherent radar design takes advantage of the fact that the radar waveform is SFM, where a large bandwidth is distributed over time in a piecewise manner. So for any given pulse, the receiver need only listen to the particular frequency that is transmitted in the pulse. The bandwidth is determined by the pulse width, as with any traditional pulsed radar. The unique attribute of the SFM-based receiver however, is that from pulse to pulse, it re-tunes to the transmitted frequency. Therefore, its instantaneous bandwidth is only just enough to pass a single pulse, but over time, the bandwidth can be arbitrarily large (theoretically, but other practical limits are imposed, such as antenna bandwidth). This appears to be a novel architecture; however, Dawood [24] describes a coherent ultra-wideband random noise radar that has similar attributes. The pulse compression is carried out by appropriately assembling the returns from each individual pulse following the math presented in Section 3.8.

A high level block diagram of the narrowband radar architecture is shown in Figure 4-11. Whereas a standard pulsed radar receiver uses a fixed, first-stage, local oscillator (LO), directly derived from the clock generator, the narrowband architecture presented here uses a first-stage LO that changes from pulse to pulse, as it is derived from the synthesized transmit signal, or in this case, the SFM waveform. This feature enables the radar to tune in to the transmit frequency for each individual pulse.

Other features of the design include a 100 W power amplifier (PA) in the transmitter, a low noise amplifier (LNA) in the receiver to provide low noise figure, and a variable gain amplifier (VGA) to enhance the receiver's non-instantaneous dynamic range.

The system was designed in a modular fashion (19-inch rack format) to isolate the six main components: transmitter, receiver, power amplifier, controller, data acquisition (DAQ) module and power supply. The front panel of the coherent UHF radar is pictured in Figure 4-12 and an operational configuration in the field is shown in Figure 4-13. Complete system control was provided through a PC graphical user interface (GUI). The PC also stored and post-processed the data acquired by the DAQ sub-system. The data acquisition card is a PCI-based, 12-bit, 4-channel data acquisition system from National Instruments (PCI-6110). To accommodate the use of a laptop (for portability), a PCMCIA-PCI expansion chassis was chosen to accommodate the PCI-6110.

Figure 4-11: Radar Block Diagram



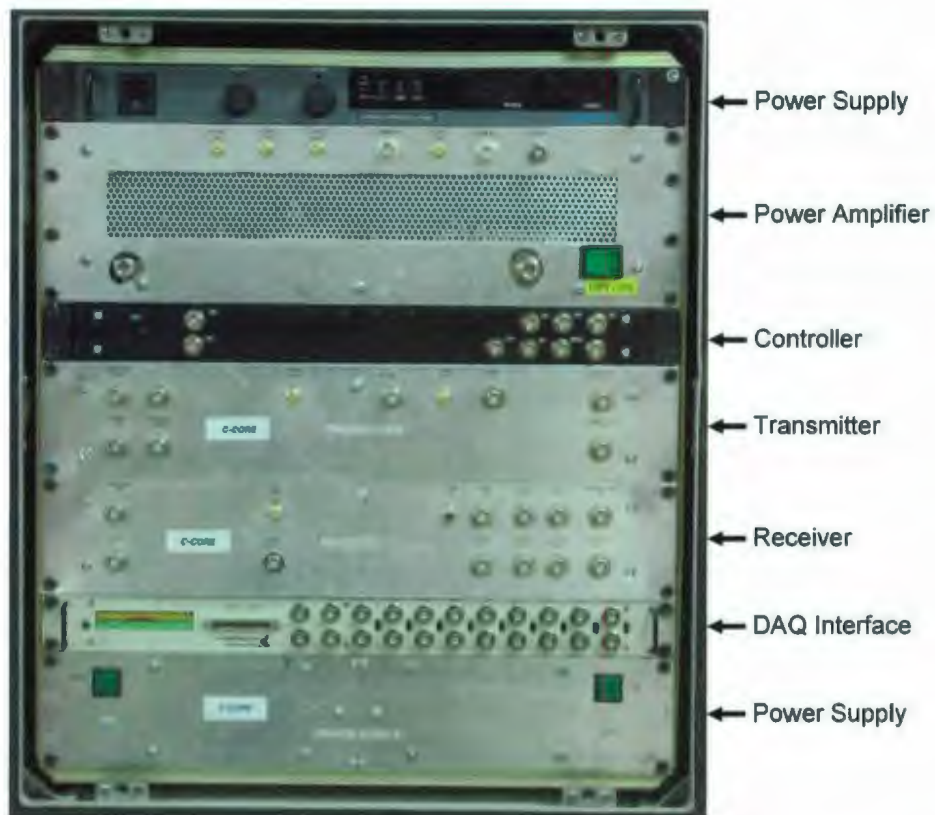


Figure 4-12: Radar Prototype Front Panel



Figure 4-13: Radar Operational Configuration

Some of the basic specifications of the prototype are given in Table 4-3. The subsections that follow provide further insight into each of the functional elements comprising the radar design.

Table 4-3: Radar Prototype Signal Specifications

Specification	Value			Units
Start Frequency	2405			MHz
Stop Frequency	2440			MHz
Bandwidth	35			MHz
Target Resolution	4.3			meters
Frequency Step	0.1	0.2	1.0	MHz
Pulse Width (τ_p)	10	5	1	μ Sec
Number Pulses (N_p)	351	176	36	n/a
Repetition Period (T_F)	100			μ Sec
Peak Transmit Power	100			Watts

4.3.1 Clock Reference/Synthesizer

The clock reference and synthesizer is a very important feature of any coherent design. As discussed in Section 4.1, the clock or local oscillator for nearly every functional element must be derived from a common reference—usually one with very good short term stability and low phase noise. The exception is the signal processor. The signal processor need not be synchronized with the reference oscillator; it only needs to process and/or store data fast enough to keep up with the data being continuously acquired.

The clock reference is typically an oven controlled crystal oscillator (OCXO), which uses a resistive heater with closed-loop control to maintain the crystal at a fixed temperature above ambient in order to enhance the stability of the oscillator circuit. A frequency of 10 MHz is chosen, since most lab instruments accept a 10 MHz external reference; in this manner, the radar may readily provide an external reference for say a spectrum analyzer so that the analyzer is phase-locked to the radar—a very important

quality for hardware debugging. An example of a clock reference that might be used in this application is shown in Appendix B.1.

The clock reference is split and distributed either to various synthesizer devices, or directly to other elements, as shown in Figure 4-11 and Figure 4-14. Each synthesizer can assume many different forms, but for coherent radar, each synthesizer must achieve phase lock with the clock reference. This is usually accomplished through some form of phase-locked-loop (PLL), in a single or double loop manner. The oscillator driven by the PLL may also be of several forms, including a voltage-controlled oscillator (VCO), a voltage-controlled crystal oscillator (VCXO), a dielectric resonator oscillator (DRO), or a coaxial resonator oscillator (CRO). The choice of technology depends on cost, complexity, frequency step size, switching rate, phase noise, and spurious output. For the prototype developed at C-CORE, low-cost VCXOs were chosen, incorporated into a single-loop PLL. Ideally, the performance requirements should be analytically or empirically linked to a phase noise requirement, from which the optimal choice of clock reference and synthesizer technology can be chosen.

The synthesizers are reprogrammable to accommodate different possibilities of signal center frequency. The examples shown in parenthesis in Figure 4-14 are for a signal centered at 22.5 MHz. f_{LO1} maps the center frequency of the baseband signal from the DDS to the center of the ISM band ($22.5+2427.5=2450$). f_{LO2} , when subsequently mixed with the baseband signal, creates an IF LO that maps any transmitted frequency to the IF frequency ($2450-2337.5-22.5=90$). f_{LO3} is chosen to be 87.5 MHz so that the IF frequency is mapped to the middle of the Nyquist band of the ADC, or 2.5 MHz. Both the DDS and the microcontroller derive their own system clocks from 10 MHz, and the ADC is clocked directly at 10 MHz; therefore, all three of f_{ADC} , f_{CLK} , and f_{DDS} are equal to 10MHz, which is generated by simply buffering the reference clock.

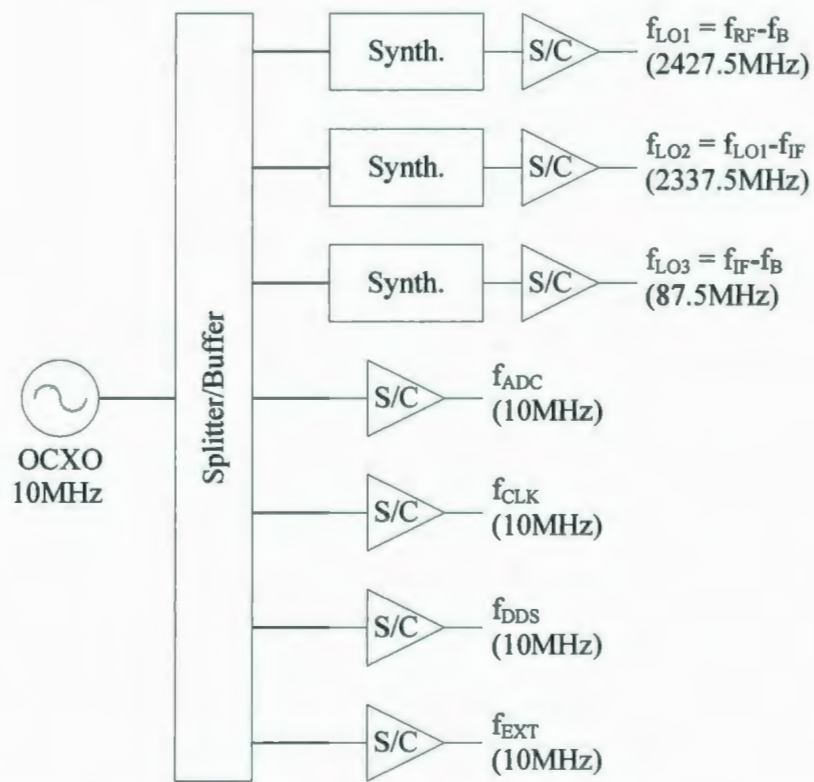


Figure 4-14: Clock Generation Block Diagram

4.3.2 Signal Synthesizer

The signal synthesizer is the element responsible for the formation of the SFM waveform. In this case it is based upon a direct digital synthesizer (DDS). A DDS is a device whose output is constructed from a sine lookup table and a digital-to-analog converter. A simplified block diagram is shown in Figure 4-15. The sine-lookup is referenced from a phase accumulator that is incremented from a fixed, but re-programmable, phase increment (called a *frequency-tuning-word*). By incrementing the phase accumulator at a fixed rate according to the frequency-tuning-word, a sinusoidal waveform is constructed through the look-up table. The frequency of the waveform is determined according to the following equation:

$$f = \Delta\phi \times f_{CLK} / 2\pi \quad (4-7)$$

where

$\Delta\phi$ is the phase increment, and

f_{CLK} is the clock frequency.

A phase offset feature is usually provided, as shown in the figure, to allow modification of the phase following accumulation, providing capabilities such as phase modulation (e.g., phase shift keying).

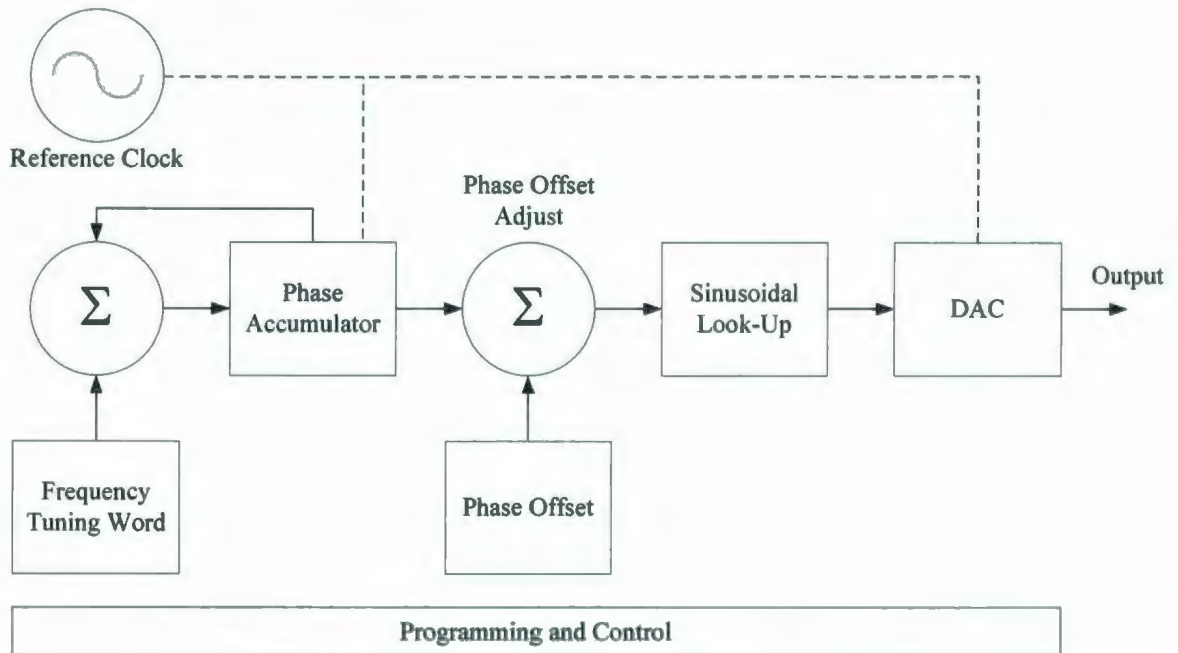


Figure 4-15: DDS Block Diagram

One feature of a DDS that should be given particular consideration for an SFM coherent radar is the generation of the frequency tuning word. In some devices the frequency tuning word, rather than being a fixed programmed constant, is generated on the fly such that the word changes with time, providing for a frequency sweep. In such a case, additional programmable constants are made available that dictates the sweep rate and frequency step. Therefore, for SFM, the designer can consider two methods to step through the waveform. The DDS can either be programmed to sweep frequency at a rate matching T_s , and a frequency step matching Δf ; or, the frequency tuning word can be directly reprogrammed at each pulse interval for the next frequency. In the latter case, the designer must be careful to allow the DDS to be programmed in a manner that is synchronous with the pulses in the SFM waveform. This adds complexity, but it provides the additional flexibility to program arbitrary frequencies for each pulse interval, rather than just a linear frequency step.

The first page of the data sheet for the DDS used in the prototype coherent radar is provided in Appendix B.2. This particular DDS was chosen, in part, because it provided I and Q outputs, which, being generated digitally, are perfectly orthogonal. This is ideally suited to feeding a quadrature modulator, whose sideband rejection would be otherwise compromised by imperfect orthogonality.

4.3.3 Transmit/Receive Multiplexer

The prototype was monostatic, using a single antenna, therefore some means of multiplexing was needed to switch the antenna between transmitter and receiver. Fast (5ns) solid state switches (e.g., gallium arsenide) are available to minimize the switch-over between transmit and receive (which factors into the blanking range); however, as these devices have moderate isolation, they typically need to be cascaded in applications such as this, adding cost and physical size to the design.

An alternative to a switch is a circulator, configured as shown in Figure 4-11. A circulator is a multiport device, typically three or four ports, whereby a signal fed into one port will only appear at the next adjacent port in one direction. In this design a four-port circulator was used, with the fourth port terminated with an absorptive load. The operation of the circulator, in this case, is as follows. The transmit signal enters port 1 and leaves port 2 radiating through the antenna. Energy resulting from target reflections is received by the antenna and routed back into port 2. This signal leaves the circulator at port 3 and is routed to the low-noise amplifier in the receiver. Any reflections at the receiver due to impedance mismatch will enter port 3 and leave the circulator at port 4 where it is absorbed by a matched load. Any subsequent reflected energy is usually insignificantly small to render damage to the transmitter or re-enter the receiver.

Since circulators are more commonly, and economically, available with three ports, a four-port circulator is easily constructed from two three-port devices as shown in Figure 4-16, which was the configuration chosen for the prototype.

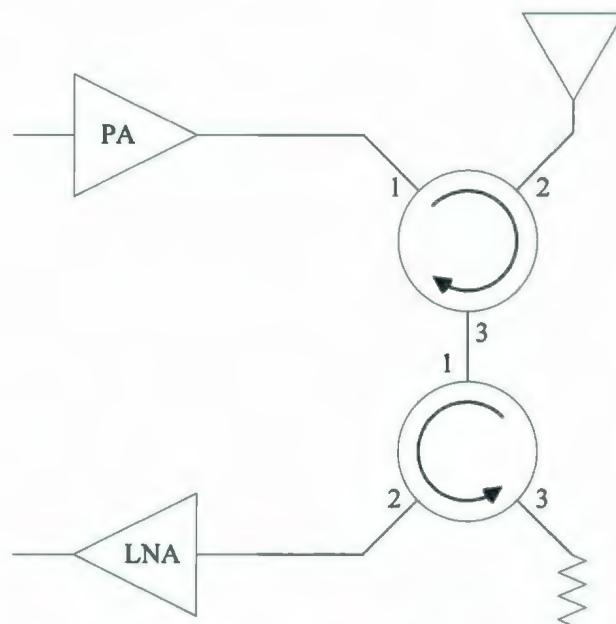


Figure 4-16: 4-Port Circulator Configuration

Despite the appeal of this design, and despite the isolation, a portion of transmitter noise is coupled to the receiver through the circulator—sufficient to raise the noise floor and compromise the sensitivity of the receiver. One solution to this problem is to gate the output of the power amp (PA); however, this is a provision that is required in the PA itself—one that was not available with the PA acquired for this design. Therefore, the circulator was removed from the radar and two antennas were used instead (Tx and Rx), resulting in an improvement in sensitivity of about 20 dB. With an appropriate PA, the circulator is still an attractive choice for the future, but careful attention needs to be paid to isolation issues.

4.3.4 Gate

The gate is shown in Figure 4-11 just prior to the power amplifier. The DDS, which synthesizes the stepped waveform, generally produces a continuous signal to which a gate must be applied, with appropriate timing, to render a pulse for each frequency step. The gate is activated/deactivated by the controller, which is synchronous with the DDS frequency step, by virtue of the fact that the controller and DDS receive a common clock and the DDS is programmed by the controller.

For the configuration shown in Figure 4-11, it was revealed that even for a good off-state gate isolation of 60 dB, the continuous DDS waveform, when amplified through the PA and reflected from the antenna (due to impedance mismatch), is coupled into the receiver at a level surpassing the receiver's sensitivity. Such a signal in the receive path (*carrier feed-through*) renders a periodic artifact in the matched filter output, as shown in Figure 4-17. The reason for this is understood intuitively as follows. A pulsed sinusoid will correlate perfectly with a continuous sinusoid of the same carrier frequency once every cycle. However, to generate a significant output, all N pulses of the SFM waveform must simultaneously correlate with their respective continuous carriers. Such an alignment occurs once every pulse-width in duration—essentially because the frequency step is determined by the pulse-width, as discussed in Section 3.4. For the example in Figure 4-17, the pulse width is 10 μ s, resulting in a feed-through artifact every 1500m in range.

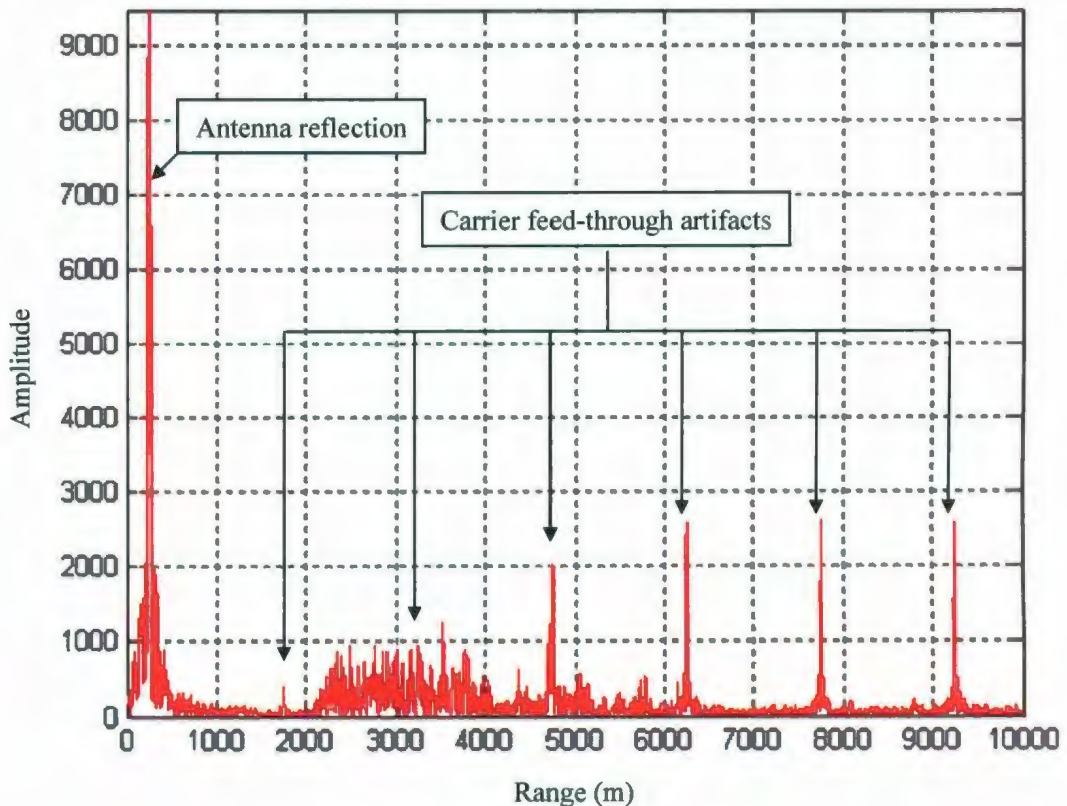


Figure 4-17: Carrier Feed-Through Effects

One solution to the carrier feed-through problem is to cascade two switches so that the effective isolation is doubled. However, it was found that in this case the artifacts were reduced, but not sufficiently eliminated. An alternate, and preferred method to the switch is to use a DDC that has the capability to modulate its output in a manner that will implement the gate. This would provide perfect rejection of the carrier; however, there is a caveat. Because the first stage local oscillator in the receiver is derived from the DDS output, the DDS output must be continuous. The work-around to this problem is to use two DDS devices—one that is modulated and feeding the transmitter path, and one that is continuous and feeding the receiver. Because these devices are digital, they can be perfectly synchronized and phase locked if fed from the same clock reference; therefore, the only downside to this approach is cost and complexity.

Another factor works in favour of a dual-DDS design. The output of the DDS is usually a current source that must see a specific resistive load. For a single DDS design followed by a quadrature modulator, splitting the I and Q output two ways complicates the matching in a way that sideband artifacts may be worsened. The easy fix to this problem is to use a two DDS devices and remove the splitter—possibly an even trade with respect to cost.

4.3.5 IF Filter

The intermediate frequency (IF) filter serves to reject out-of-band noise and interference that would otherwise compromise the dynamic range of the receiver by increasing the minimum detectable signal or sensitivity. For a typical radar, the IF bandwidth should be wide enough to pass the radar signal over the linear portion of the pass-band, thereby avoiding any signal distortion. This can generally be accomplished by specifying a 0.5 dB bandwidth over the pass-band of the filter.

The IF is selected through well-known heterodyne receiver design practices. The IF determines the separation between the desired RF band and its image; the order of the image rejection filter at RF is dictated by this separation. So the larger the IF, the simpler, and cheaper the image reject filter. However, the IF filter is primarily intended to maximize the sensitivity of the receiver by limiting the pass-band to the signal bandwidth. The order, or complexity, of a filter is dictated by the ratio of its center

frequency to its bandwidth—called the *quality factor*, or Q . So for any desired bandwidth, as the chosen IF increases, the Q increases, thereby increasing the filter complexity and cost. Therefore, the choice of IF comes from a careful balancing between RF and IF filter complexity. For the prototype, an IF of 90MHz was chosen.

The choice of filter technology is dictated by both the IF frequency and desired electrical characteristics of the filter. A *cavity filter* uses a hollow resonant cavity to achieve a band-pass, or band-reject, characteristic. An exciter is used to generate an electromagnetic field in the cavity which in turn is subject to the resonant characteristic of the cavity. This filter type was chosen for the radar prototype since it has very low insertion loss (less than 1 dB), and a very sharp roll-off is achievable with a multi-section design. The disadvantages of a cavity filter are that it is physically large, especially at low center frequencies, and is costly relative to other options; however, these were not deterrents for this *one-of* prototype. For lower frequency pass-bands, or cases where physical size and/or cost is a premium, a discrete filter, comprising a network of capacitors and inductors, can be a more appropriate choice.

For the SFM-based coherent radar, the filter characteristic need only be sufficient to capture the signal bandwidth associated with a single pulse in the waveform, since every pulse is translated to the common IF of 90 MHz. Therefore, the IF bandwidth is determined from the pulse-width. In order to enhance the flexibility of the radar, it would be useful that it accommodate various pulse widths. Recall, that the larger the pulse width the larger the blanking range of the radar, and the smaller the frequency step. Optimal sensitivity for each pulse width requires a different IF bandwidth for each pulse width. This may be incorporated into the radar design, as shown in Figure 4-18, but with added expense and complexity.

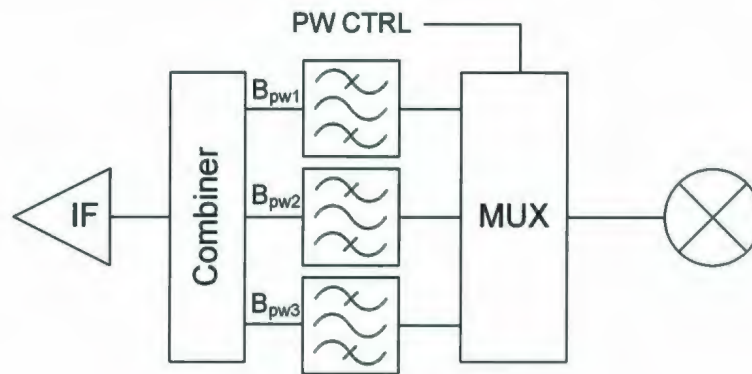


Figure 4-18: Multi-IF-Filter Design

4.3.6 Demodulator

The architectural structure of the receiver is a purpose-built single-conversion super-heterodyne design. The single-conversion attribute implies there is a single IF, and therefore, two mixing operations—one before, and one after, the IF filter. A demodulator is the last element in the chain of analog elements of this receiver. The demodulator, in its simplest form, is the second mixing operation that frequency shifts the signal at IF to baseband (or near-baseband¹) for digitization. Typically, demodulators incorporate additional features such as received signal strength indication (RSSI), AM or FM detection, gain control, and quadrature (I and Q) output channels. Furthermore, demodulators can contain an integrated PLL for generating the LO from an external reference. A block diagram of the demodulator employed within the prototype is illustrated in Figure 4-19. This demodulator was chosen primarily because it had a suitable IF range covering the 90 MHz IF of the prototype, and a demodulation bandwidth in excess of a single pulse bandwidth. This model also provided a gain control, which was driven by the controller to optimize the total receiver based on the noise floor. Finally, this demodulator provided both I and Q channels. This permitted a means to evaluate two approaches—forming the analytic signal in the analog domain by digitizing both I and Q channels, or in the digital domain from a signal channel.

¹ Some choose to refer to baseband as only the condition whereby the signal band is centered at DC. However, this is only possible when quadrature channels (I and Q) exist. For single channel down-conversion, baseband can be considered the region just above DC, with an image just below DC. It's purely a matter of semantics.

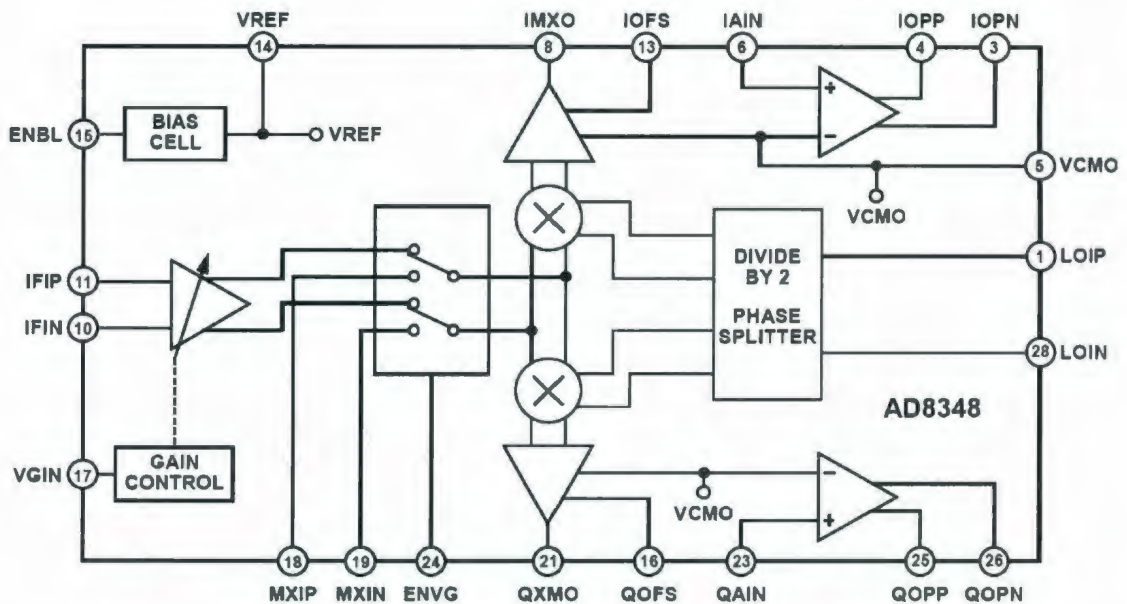


Figure 4-19: Demodulator Block Diagram (©2006 Analog Devices)

Other forms of receiver architectures can be employed in a radar design. For example, direct down-conversion, or zero-IF (ZIF), is gaining in popularity due to a reduction in complexity in the analog front-end, which in turn provides cost savings. However, for low volume, the magnitude of these cost savings is not worthwhile since the direct down-conversion design does make certain compromises. For instance, because the local oscillator (LO) is at the carrier frequency, LO leakage and self-mixing will cause DC offsets that may saturate the input to the ADC. Also, flicker noise is known to be more pronounced in ZIF designs. However, because such methods employ IQ demodulators, the ADC sample rate can be halved for a fixed bandwidth—or conversely, the bandwidth doubled for a fixed sample rate.

Another increasingly popular receiver architecture uses band-pass sampling, whereby the IF band can be sampled directly by exploiting aliasing to fold the IF to baseband using an appropriate selection of an IF band and sample rate. Like ZIF, this method can reduce component count by simplifying the receiver front-end, but at a cost. Sample jitter has a more prominent effect at higher input frequencies due to the higher

slew rate associated with these frequencies. This can have the effect of degrading SNR and reducing the SFDR of the receiver.

Finally, a double-conversion super-heterodyne, uses two IFs and three mixers. This design philosophy combines the benefits of selecting a low IF for superior selectivity and a high IF to reduce image responses resulting from mixing. However, for a single channel non-tunable design, channel selectivity is not a constraint; the double conversion design adds more components and complexity to the design; and, the inclusion of more LOs in the design increases the number of inter-modulation products that may result in unwanted spurious responses.

4.3.7 Digitizer

The radar prototype used an off-line processing method, rather than real-time. This means that a single coherent SFM multi-cycle waveform was transmitted with a fixed antenna orientation, and the return was digitized and placed in non-volatile storage (hard disk). The ambiguity response was then calculated on a personal computer (PC) platform. A PCI-based adaptor card was a convenient choice for the ADC function. This allowed the digitized data to be readily stored to hard disk and subsequently processed with PC-based S/W. A 16-bit 10 MHz digitizer was chosen, which provided more than sufficient bandwidth to capture the smallest anticipated pulse, 1 μ s in duration.

For future consideration of a real-time scanning radar, the use of a PC-based acquisition card will require careful consideration to ensure the throughput can be sustained. The PCI bus is particularly limited, not only in the sustainable throughput, but more importantly, with respect to the predictability of data throughput. The PCI bus is a shared system bus; therefore, other system resources can unexpectedly burden the bus and cause an overflow of data from the acquisition card. A dedicated bus for data acquisition can ensure no loss of data (or in this case coherency), but is usually an expensive option, possibly requiring custom hardware development. Fortunately, since constructing the prototype, newer general purpose PC-based buses have evolved that run at much higher speeds; for example, PCI-E (or PCI-Express) boasts multi-lane serial communications with aggregate transfer rates up to 8GB/s.

For future prototypes, the choice of digitizer and supporting communications will be dictated by the signal bandwidth (and thus sample rate), antenna scanning rate, the azimuth resolution, and operating range.

4.3.8 Signal Processor

As discussed in the previous section, the prototype engaged a PC to perform off-line signal analysis on the captured data. Scientific computing software (Matlab™) was used for this purpose, and readily available signal processing libraries (Matlab™ Signal Processing Toolbox). Section 4.4 will present the processing algorithms developed for the prototype.

Akin to the discussion in the previous section, future consideration of a real-time scanning radar will also require careful analysis of the processing platform. For off-line processing, the platform was not under any severe constraints for processing bandwidth (other than user patience). However, the continuous flow of data from an operational, scanning radar requires substantial processing bandwidth so that the return from each signal transmission is processed and stored, or rendered to the user, before the next signal transmission. This will be put in more concrete terms by way of example in Section 6.

4.3.9 Controller

Although the DDS can autonomously produce an SFM waveform using its ramp capability, it is not well-suited to producing a multi-cycle waveform. For this reason, an embedded controller was employed to reinitiate the DDS in a synchronous manner to produce multiple cycles of the same waveform. Although it is not the original motivation, the controller also provides a means to arbitrarily program the frequency and phase of each pulse within the SFM waveform. This can provide, for example, a means to explore the effects of non-linear frequency steps; although, this was not explored in the study.

4.3.10 Antenna

For the study, the antenna was intended to be in a fixed orientation (i.e., not scanning) in order to evaluate the proposed coherent techniques. A slotted waveguide

antenna was the simplest and most cost effective solution for these purposes, as compared, for instance, to a phased array. However, slotted waveguides are resonant antennas with a relatively narrow operating bandwidth; so the antenna, not the electronics hardware, was the limiting factor in determining the range resolution of the prototype.

The antenna construction is depicted in Figure 4-20 (a picture taken during field deployment is shown in Figure 4-22). A radiating element, internal to the waveguide, is externally attached to a coaxial feed. The radiator launches the electromagnetic wave within the waveguide, which in turn is radiated externally through the slots. The slot dimensions, slot spacing and waveguide dimensions combine to determine the resonance and beam-pattern of the antenna. Tuning screws are used to fine-tune the center frequency and reduce the voltage standing-wave-ratio (VSWR) within the radiation bandwidth. Reduction of the standing wave ratio minimizes the reflected power from the antenna back towards the power amplifier, thereby maximizing the radiated power. The tuning is accomplished by connecting the antenna directly to a network analyzer that sweeps a signal of known power across the bandwidth of interest into the antenna and measures the reflected power across the same bandwidth¹. The tuned VSWR response of the prototype antenna is shown in Figure 4-23. A VSWR of 2 represents an efficiency of just under 90 percent. Taking these points as the band extremities, the tuning of the antenna yielded a bandwidth of approximately 35 MHz. This corresponds to a range resolution of 4.3m.

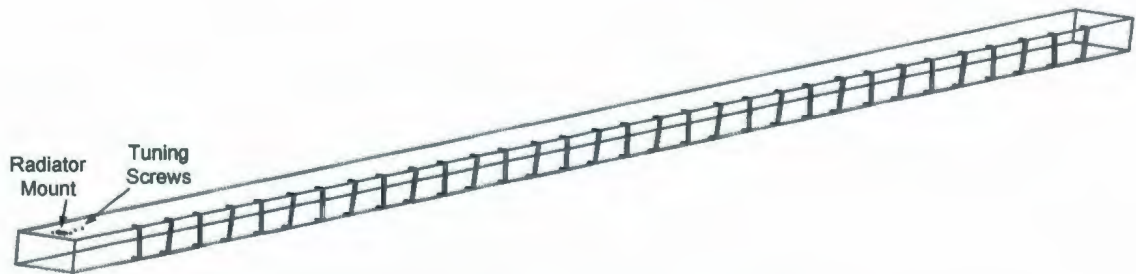


Figure 4-20: Slotted Waveguide Antenna

¹ Reflected power is the S_{11} term of a four-port network.

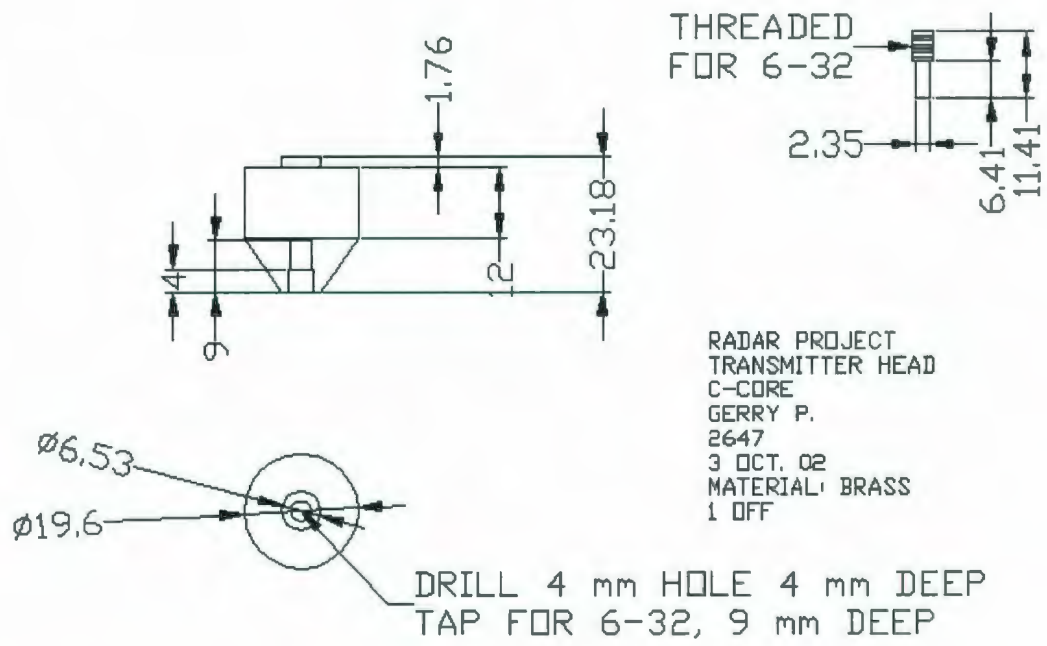


Figure 4-21: Antenna Radiator



Figure 4-22: Field Deployment of Antenna

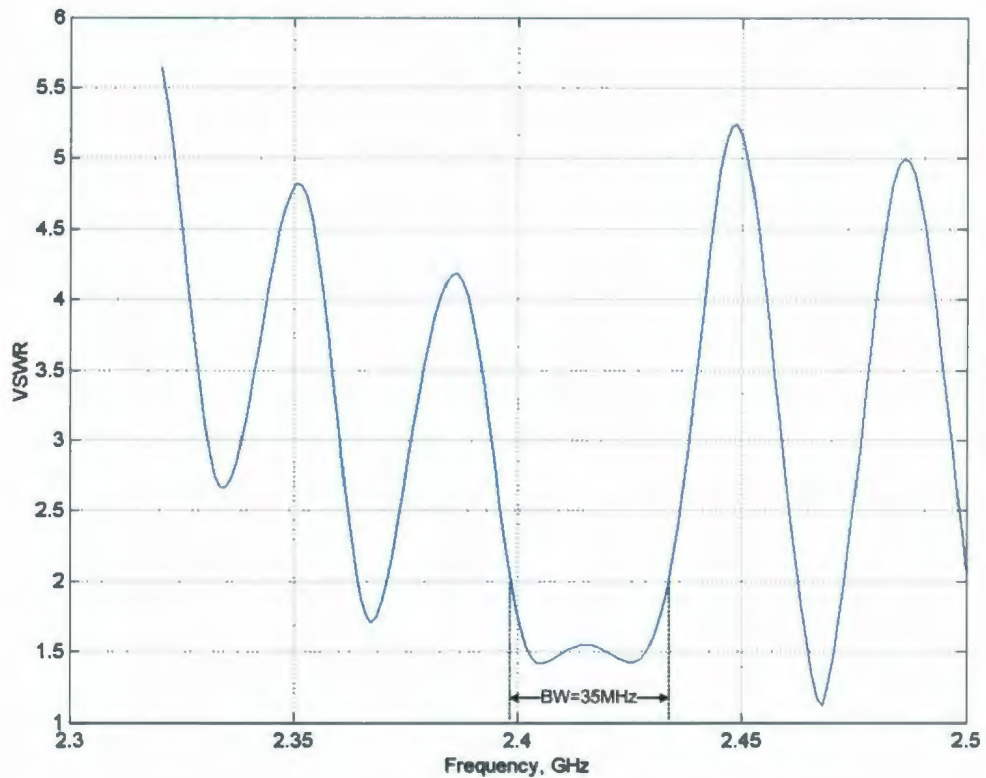


Figure 4-23: Antenna VSWR

A waveguide antenna, comprising many radiating slots, relies upon the interference pattern of the combined radiation from each slot, or radiator, to create a resultant radiation pattern. At close range to the antenna, or the region known as the *near field*, this interference pattern is very complex. At some range, the pattern converges to a deterministic form, representative of the designed beam pattern. This range, known as the *far field*, begins at range R_{ff} , denoted as

$$R_{ff} = \frac{2L^2}{\lambda} \quad (4-8)$$

where

L is the length of the antenna and λ is the wavelength.

A range of $R_{ff}/2$ is usually sufficient to accommodate beam pattern measurements and calibration. The antenna employed by this study was ~ 3 m in length; therefore, the

signal wavelength and antenna aperture length required that measurements of radiated power be conducted at a minimum distance of 75 m to ensure a far field assessment and thus produce a beam pattern truly representative of the antenna. This dimension precludes the use of an anechoic chamber; therefore, the supporting instrumentation was brought to an open field to conduct a verification of the antenna design. The method devised for this *calibration* is depicted in Figure 4-24. A stepper motor rotates the waveguide antenna while a signal generator (Rohde & Schwatz SML03) transmits a continuous wave (CW) signal at 2.425 GHz (center of band) through the antenna. A calibrated antenna (Aaronia AG HyperLOG 4060) receives the signal and a spectrum analyzer (Rohde & Schwatz FSP7) measures the received power. By setting a known angular velocity of the motor and a known sweep rate of the analyzer (used in “zero-span” with center frequency equal to 2.425 GHz), a precise radiation beam pattern of the antenna was acquired. The open-field setup is pictured in Figure 4-25 and Figure 4-26. The results of the calibration are shown in Figure 4-27.

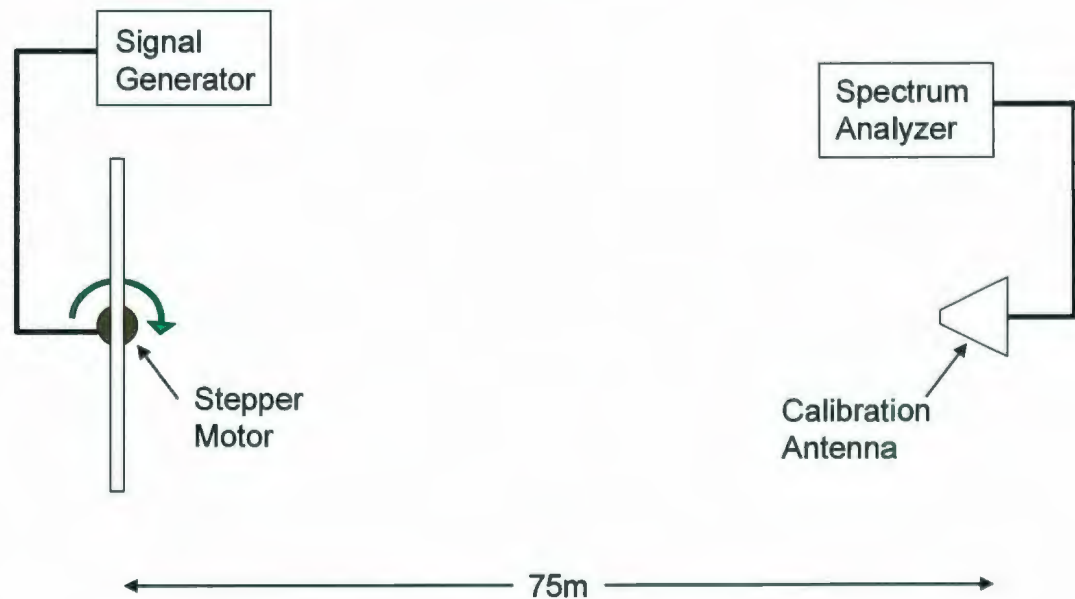


Figure 4-24: Antenna Calibration Field Set-up



Figure 4-25: Open Field Site (Calibration Antenna in Foreground)



Figure 4-26: Field Site (Antenna and Stepper Motor Configuration)

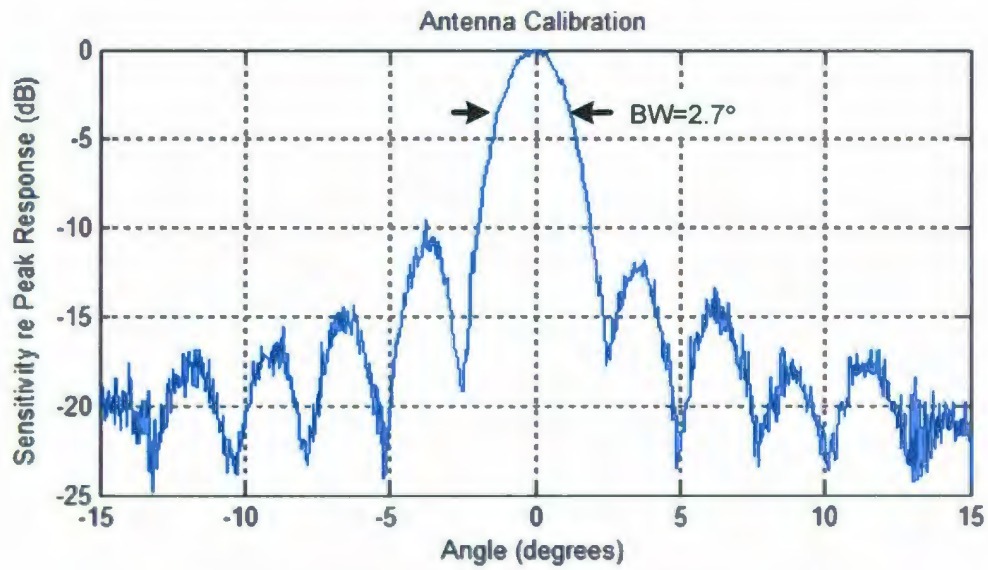


Figure 4-27: Antenna Calibration Results

The theoretical azimuthal beamwidth of the antenna, determined by its length and the nominal signal wavelength, is $3 \times 10^8 \text{ m/s} \div 2.45 \times 10^9 \text{ Hz} \div 3.08 \text{ m} \times 360^\circ \div 2\pi = 2.3^\circ$. The measured beamwidth of 2.7° is reasonably close to this ideal. The first sidelobe for a uniformly tapered antenna is theoretically -13 dB. For this prototype, one sidelobe met this ideal; however, the other sidelobe was measured to be 11 dB. This is a reasonable result, with the slight shortcoming most likely due to variances between design and fabrication. The operational specifications of the antenna are summarized in Table 4-4.

Table 4-4: Antenna Specifications

Specification	Value	Units
Length	3.08	Meters
Bandwidth (VSWR 2:1)	35	MHz
Bandwidth (VSWR 3:1)	43	MHz
Beamwidth	2.7	°
Gain	13.6	dB
Maximum Sidelobe Level	-10	dB

4.4 Processing Algorithms

As previously discussed, the processing component of the prototype was implemented off-line. Accordingly, processing bandwidth was not a limiting criterion. Methods to implement efficient processing algorithms on real-time platforms were outside the scope of this study. The method of data analysis was to compute, in a *brute force* manner, the ambiguity response associated with the radar return from any given complete transmitted signal.

Because of the narrowband nature of the receiver, equations (2-14), (2-15), and (2-16) cannot be used directly to compute the response. These equations assume the received signal sweeps the entire band of frequencies comprising the SFM waveform. However, as noted in Section 4.3, the receiver maps each received frequency step to a common IF prior to digitization. Therefore, these equations cannot be directly used to compute the ambiguity response. Instead, the isomorphic matched filter method presented in Section 3.8 is used. Note that Section 3.8 provides the mathematical foundation for computation, under the narrow-band constraint, of the matched filter (where the domain comprises only the range), rather than the ambiguity response (where the domain comprises both range and velocity). The implementation discussed below extends the technique from Section 3.8 to include the velocity component, thereby rendering the complete ambiguity response.

Figure 4-28 illustrates the signal transformations from transmission through to the matched filter output. Figure 4-28(a) is the transmitted SFM waveform. Figure 4-28(b) is representative of the received waveform reflected from a point target, where the original signal is delayed (this is an idealized case—in reality, the waveform is subject to propagation phenomena such as multipath and dispersion which will corrupt the waveform envelope). Figure 4-28(c) shows the IF resulting from mixing the received signal with a stepped LO—this waveform is digitized and becomes the input to the algorithm described below.

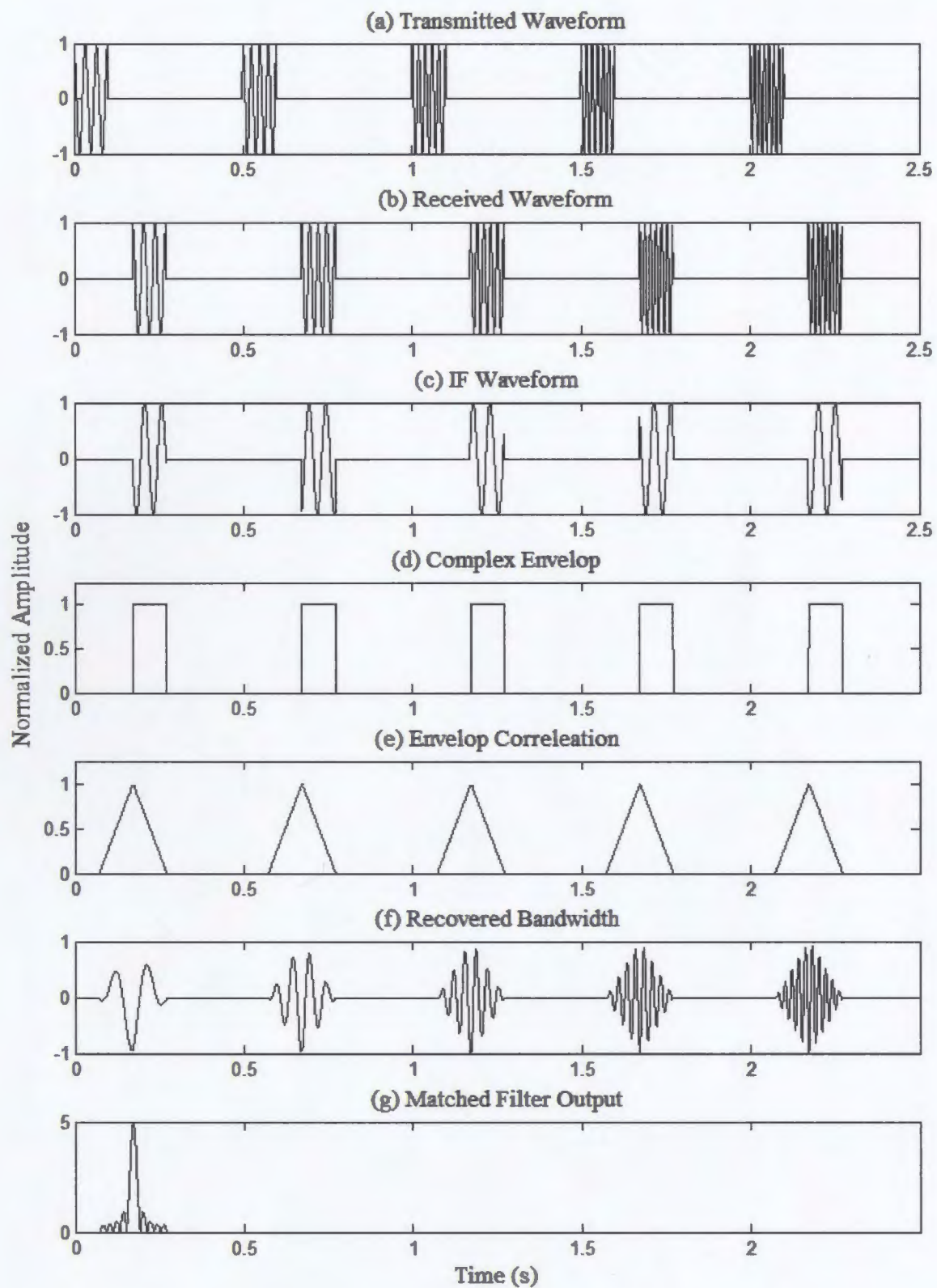


Figure 4-28: Waveform Transformations

4.4.1 Main Functional Elements

The core of the processing algorithm comprises four essential steps derived from Section 3.8; these are as follows:

1. Doppler Frequency Modification
2. Complex Envelope Formation
3. Correlation
4. Bandwidth Recovery
5. Accumulation

These steps are executed iteratively in a triple-nested-loop fashion—the inner loop executed for N_p pulses, the middle loop executed for N_c cycles, and the outer loop executed for investigated Doppler frequency. A flowchart is provided in Figure 4-29 for clarification. Further discussion of each step follows.

4.4.1.1 Doppler Frequency Modification

Each outer loop of the process generates a Doppler reference signal in the form of a complex exponential—a portion of which is multiplied by the digitized IF (Figure 4-28(c)) within each pulse response of the inner loop. A unique Doppler reference frequency is chosen for each iteration of the outer loop so that the inner loops calculate the matched filter response for each Doppler frequency, over a range of frequencies wide enough to capture all anticipated target velocities. The modification, if matched to the target velocity, reverts the Doppler effect on the echo from a moving target and produce an optimal matched filter response. Thus, the outer loop provides the velocity domain of the ambiguity response.

It is important that the Doppler reference signal for each iteration of the inner loop be derived from a time-continuous complex exponential function over the entire duration of the multi-cycle waveform; otherwise, the phases from pulse-to-pulse and cycle-to-cycle will not be representative of a moving target, thereby rendering an incorrect ambiguity response.

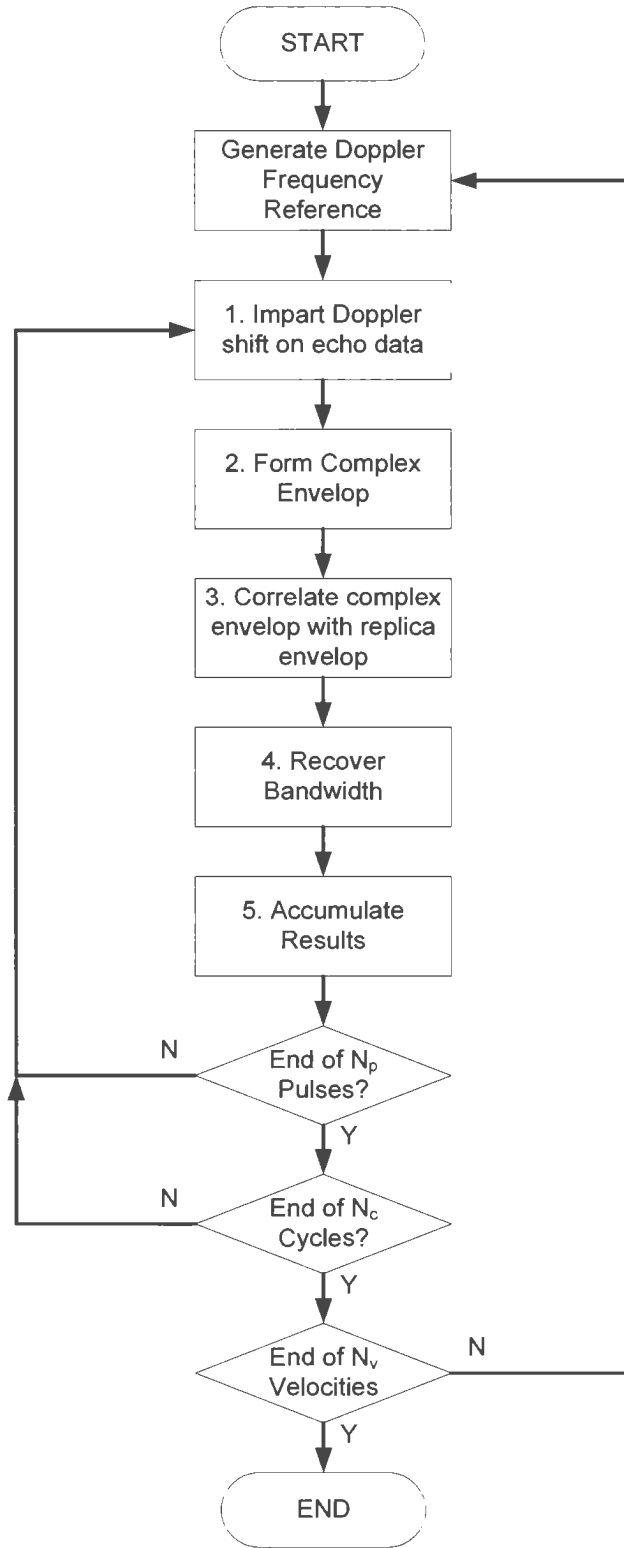


Figure 4-29: Core Processing Algorithm Flowchart

4.4.1.2 Complex Envelope Formation

The complex envelope formation creates the $m'_s(t)$ term in equation (3-30). For an ideal echo, the complex envelope would appear as shown in Figure 4-28(d).

4.4.1.3 Correlation

The correlation block computes the correlation between the complex envelope from the previous step and the envelope of the transmitted signal, which is simply a rectangular pulse train. This computation is represented by those elements to the right of, and including, the integral in equation (3-30). For an ideal echo, the output of the correlation would appear as shown in Figure 4-28(e).

4.4.1.4 Bandwidth Recovery

This step is represented by the exponential term to the left of the integral in equation (3-30). Following the correlation, what remains is essentially the complex envelope of the matched filter output for each pulse. The collective bandwidth, which was reduced during down-conversion to a common IF, must be re-introduced prior to integrating all of the pulse responses together. This is accomplished by up-converting each response by successive frequency offsets that match the frequency steps in the SFM waveform. For an ideal echo, the output of this step would appear as shown in Figure 4-28(f).

4.4.1.5 Accumulation

The final step simply sums all of the responses derived from the last step, rendering the pulse-compressed cumulative response shown in Figure 4-28(g).

4.4.2 Implementation

The algorithm described above was implemented in Matlab™ script. The script provided the facility to carry out processing on either real data obtained from the prototype, or simulated data, generated within the script. This provided a means to draw comparisons between real and simulated data. Example 5 shows a comparison between simulated data and real data; the matched filter outputs are shown in Figure 4-30 and Figure 4-31, respectively. For this case, the real data was obtained in the lab, where the

propagation delay was realized using a spool of fiber optic cable and an optical transmitter/receiver pair. This sort of set-up is vital to validating radar performance prior to field deployment.

Example 5: Simulated and Real Data Comparison	
T_s	100 μ s
τ_p	5 μ s
B	35 MHz
Δf	0.2 MHz
N_p	176

There are a couple of important consistencies between the simulated and real outputs. First, the main lobe of the response is similar in width and shape, and in both cases, the predicted range resolution is achieved. Second, the first sidelobe levels are similar (approximately -13 dB). The real data is subject to noise, which is evident in the output for this case. (The main lobe range positions are slightly different between the figures because the target position configured for simulation was not identical to that of the real experiment.)

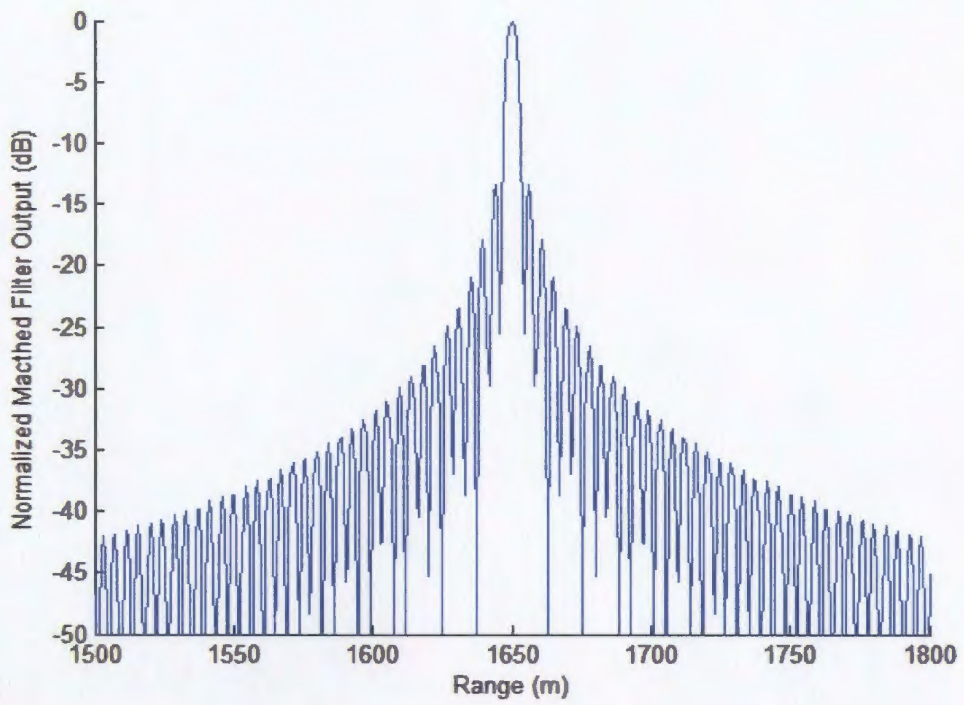


Figure 4-30: Matched Filter Output – Simulated Data (Example 5)

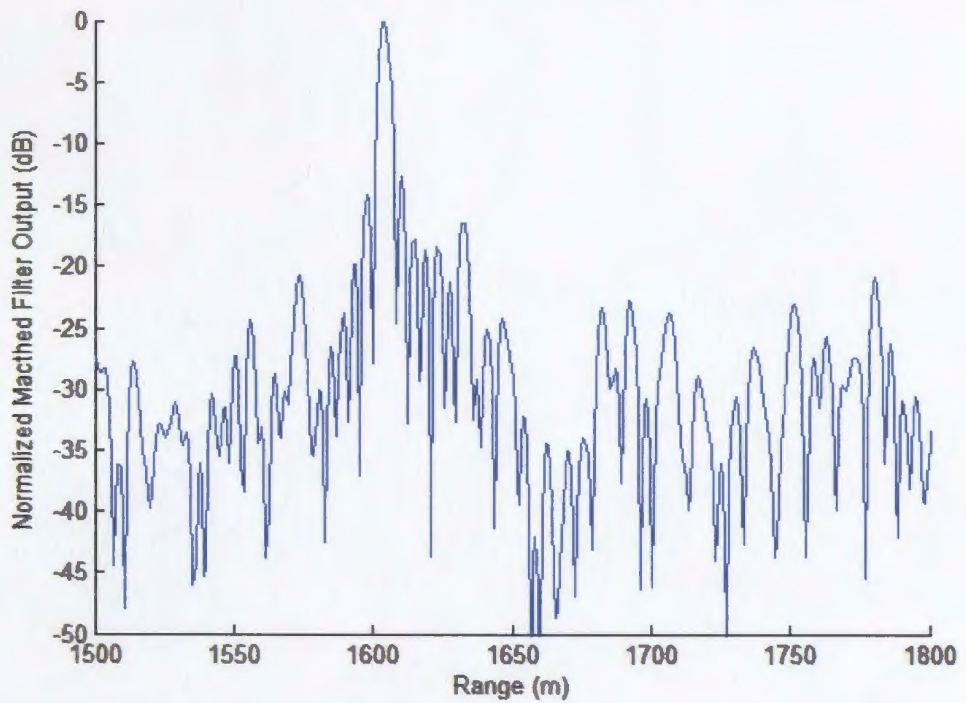


Figure 4-31: Matched Filter Output – Real Data (Example 5)

5. Experimental Data

A field program was conducted at C-CORE to evaluate the radar prototype. This section discusses the applied methodologies, study locations, experimental objectives and the outcomes, which are also documented in [25].

5.1 Methodology

The intent of the field program was to quantitatively assess the performance of the radar in a real ocean environment while exercising as much experimental control as possible. Standard targets are widely used in radar calibrations to provide a fixed and known reflector reference. A standard target provides a known, fixed and often isotropic radar signal reflectivity, or radar cross-section (RCS); therefore, for a given radar configuration and a given physical geometry of the antennae and target, the performance of the radar can be predicted and compared to actual measured results.

This study used a Lunberg Lens as a standard target. The Lunberg Lens is a novel design that provides an omni-azimuthal response over a vertical beamwidth of $\pm 10^\circ$. It is pictured in Figure 5-1. The Lunberg Lens acquired for this study was designed for X-band radar (9.4 GHz) with an RCS of 10 m^2 . However, at 3 GHz (S-band), the manufacturer (Luntech, in France) claimed a reduced RCS of approximately 1 m^2 . Theoretically, the RCS is inversely proportional to the wavelength; therefore, the theoretical RCS of this lens at S-band is indeed 1 m^2 , as suggested by the manufacturer. For an operating frequency of 2.425 GHz, the predicted RCS of the lens is 0.66 m^2 .

5.2 Study Areas

Three main field sites were chosen for the field program—a large target site, a frozen lake site and an exposed bay site. These sites are all in close proximity to St. John's, NL, as shown in Figure 5-2. Successively, each site was chosen as the study progressed from a system verification phase to a performance evaluation phase.



Figure 5-1: Lunberg Lens

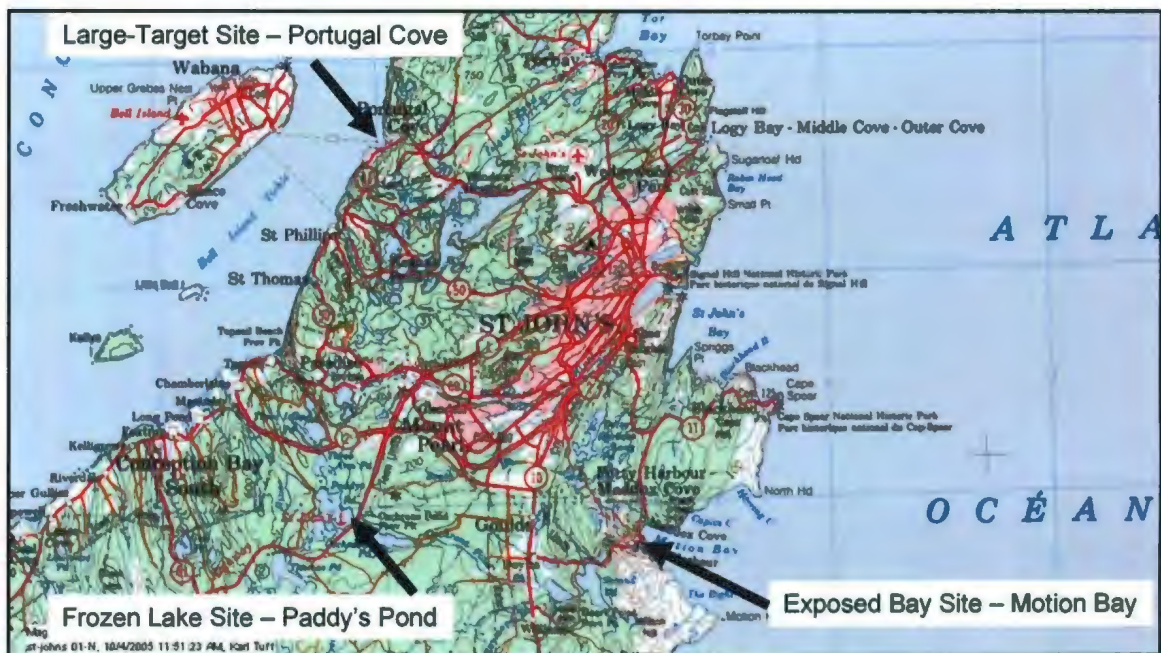


Figure 5-2: Annotated Map of Relative Locations of Field Sites

5.2.1 Large Target Site

The large target site was chosen to verify and assess the basic functionality of the radar, while taking advantage of very large targets to produce high signal-to-clutter ratios. Portugal Cove breakwater was chosen for this purpose as it was in close proximity to

C-CORE and provided two large targets—Bell Island and the ferry. The antenna set-up at this site is pictured in Figure 5-3. A map of the study area is shown in Figure 5-4.



Figure 5-3: Antenna Configuration—Portugal Cove Field Site



Figure 5-4: Annotated Map of Portugal Cove Field Site

5.2.2 Frozen Lake Site

A frozen lake was chosen as a convenient means to establish a virtually clutter-free environment for small targets. This provided a controlled situation to debug and fine-tune the system using a standard target as a reference. Paddy's Pond, just west of St. John's and adjacent to the Trans Canada Highway, was chosen due to its proximity to C-CORE and because it provided a large area over which the target could be placed. A minimum range of 750 m is required using a 10 μ s pulse, and 75 m using a 1 μ s pulse, to ensure targets are not obscured by the direct coupling between the transmitter and receiver as the pulse is emitted; this site provided 1.8 km of useful range—which was quite adequate. A map of the study area is shown in Figure 5-5.

The standard target was mounted atop a surveyor's tripod and elevated to a height of about 2 m for the experiment as shown in Figure 5-6. A 0.86 m corner reflector (RCS=146 m²) was deployed as an auxiliary target, as seen in the background of this picture. The radar itself was located in a cube van fitted with a propane heat source to protect the equipment and personnel from the environment (see Figure 5-7).

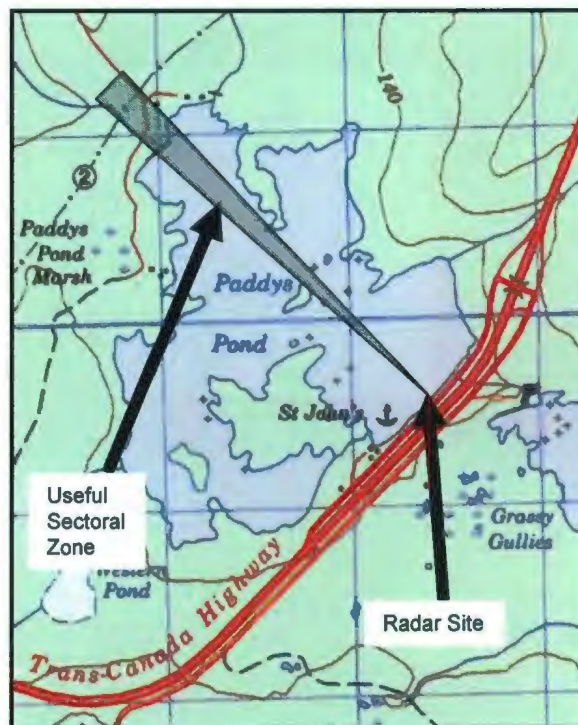


Figure 5-5: Annotated Map of Paddy's Pond Field Site



Figure 5-6: Standard Target (Lunberg Lens) with Tripod Configuration



Figure 5-7: Radar Shelter and Working Quarters

5.2.3 Exposed Bay Site

An exposed bay was chosen to provide significant ocean clutter conditions. Motion Bay, just south of St. John's and outside Petty Harbour was chosen as a site that was easily accessible by land and one that provided a wide view of the ocean from a reasonably high vantage point (>10 m elevation). A map of the study area is shown in Figure 5-8.

The standard target was mounted atop an Ottawa River Type (ORT) buoy for this experiment. This buoy was chosen for its portability and stability. As the Lunberg Lens can only tolerate $\pm 10^\circ$ of tilt before its reflective property is severely compromised, it was important to maintain a vertical position while being subject to the ocean's wave energy. The buoy configuration is pictured in Figure 5-9. Weights were applied to bottom of the assembly for ballast and to achieve the desired draft. Ideally, the Lens should have been placed as close to the water line as possible to simulate a target sitting directly on the water; however, concerns over having little reserve buoyancy to prevent loss of the package resulted in a choice of ballast that left the target sitting approximately 1.5 m above the water line.



Figure 5-8: Annotated Map of Motion Bay Field Site



Figure 5-9: ORT Buoy / Lunberg Lens Configuration

The radar was located near the roadside beneath Skinner's Hill, between Petty Harbour and Maddox Cove (Figure 5-8). The site is pictured in Figure 5-10.

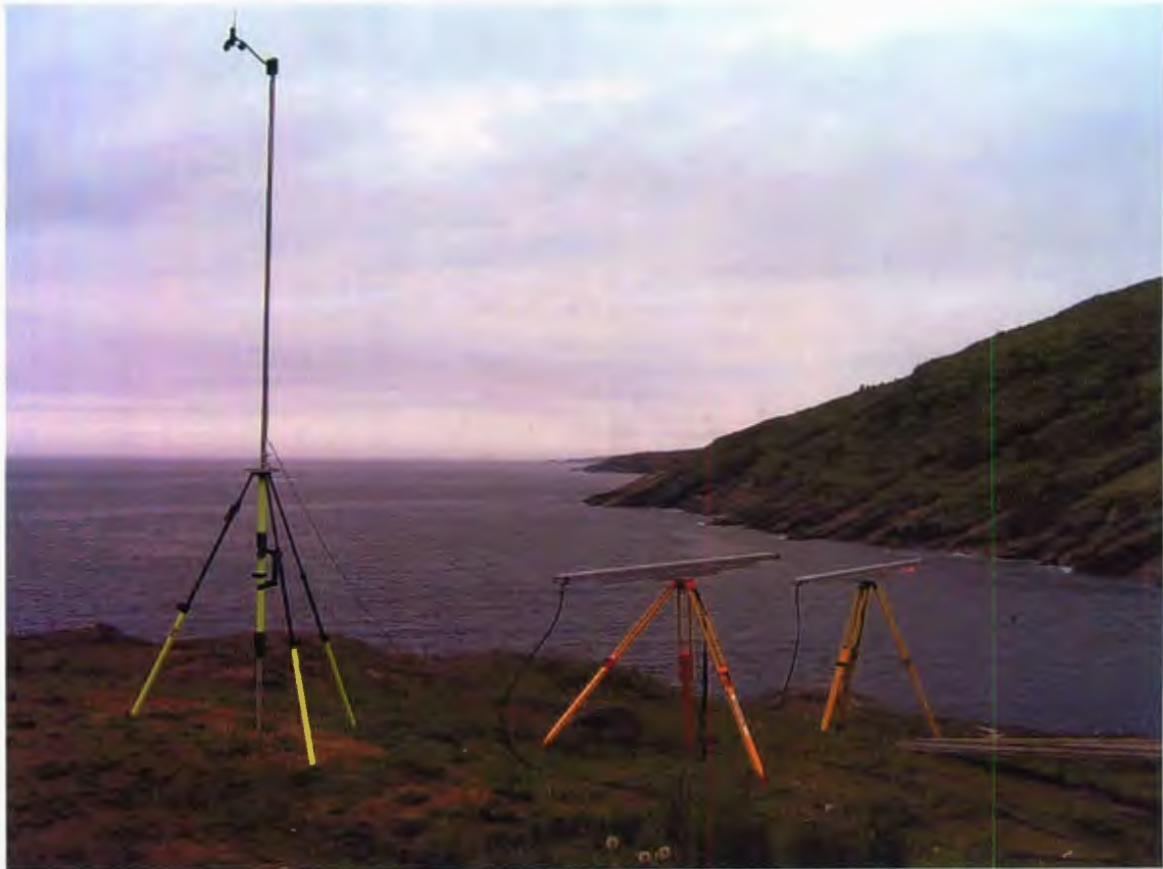


Figure 5-10: Motion Bay Radar Site

5.3 Objectives

The main objectives of this field study are outlined as follows:

1. Assess the operational condition of the radar as part of finalizing the design and establishing a robust platform for further extensive field work.
2. Assess the resolution capability (range and Doppler) of SFM resulting from pulse compression compared with theoretical benchmarks.
3. Assess the processing gain of SFM resulting from pulse compression compared with theoretical benchmarks.
4. Assess the capability of the radar to suppress ocean clutter through consideration of the Doppler domain.
5. Identify benefits and constraints in applying this technology to commercial applications.

5.4 Experimental Results

5.4.1 Operational Test—Portugal Cove

The Portugal Cove field site was used to carry out an assessment of the operational condition of the radar, and to accommodate the identification and remedy of hardware and software bugs. A sample of data is given in Figure 5-11 that confirms the system was operational and in good condition to proceed with further experimentation. There are several important features in this figure, discussed below.

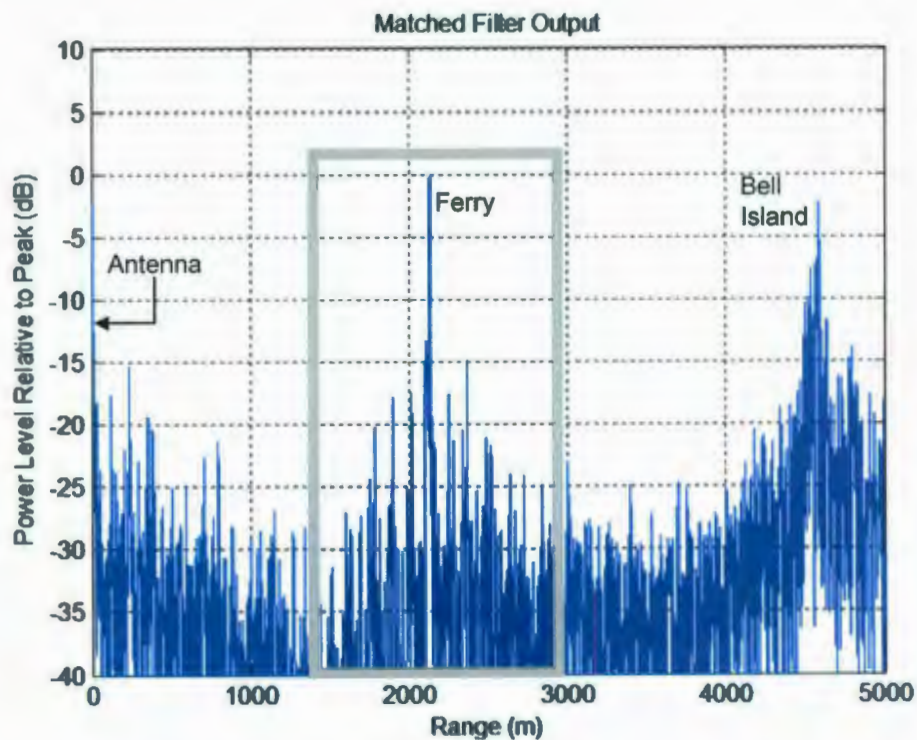


Figure 5-11: Radar Output for Bell Island and Bell Island Ferry

Bell Island is a very obvious target in this data set—as it should be, since the perimeter of Bell Island is a steep cliff. However, because the shoreline is irregular and the radar beam illuminates about 200 m of this shoreline (at 4500 m range, assuming a 2.7° beamwidth), the reflection is very diffuse, or comprises many overlapping signal returns. Therefore, Bell Island does not appear as a very distinct target.

The ferry on the other hand, is a much more distinct target than Bell Island, appearing as a spike. However, close inspection of Figure 5-12 reveals that even the

ferry does not have a distinct response. This is because the length of the ferry, about 50 m, is much longer than the radar resolution of 4.3 m—so the signal return from the ferry essentially comprises reflections from many range bins. The figure also shows that most of the energy is contained over a range of about 50 m, coinciding with the dimensions of the target vessel. This example demonstrates that high-resolution radar is not only useful in resolving separate targets in close proximity, but is also useful in identifying the physical size of a target.

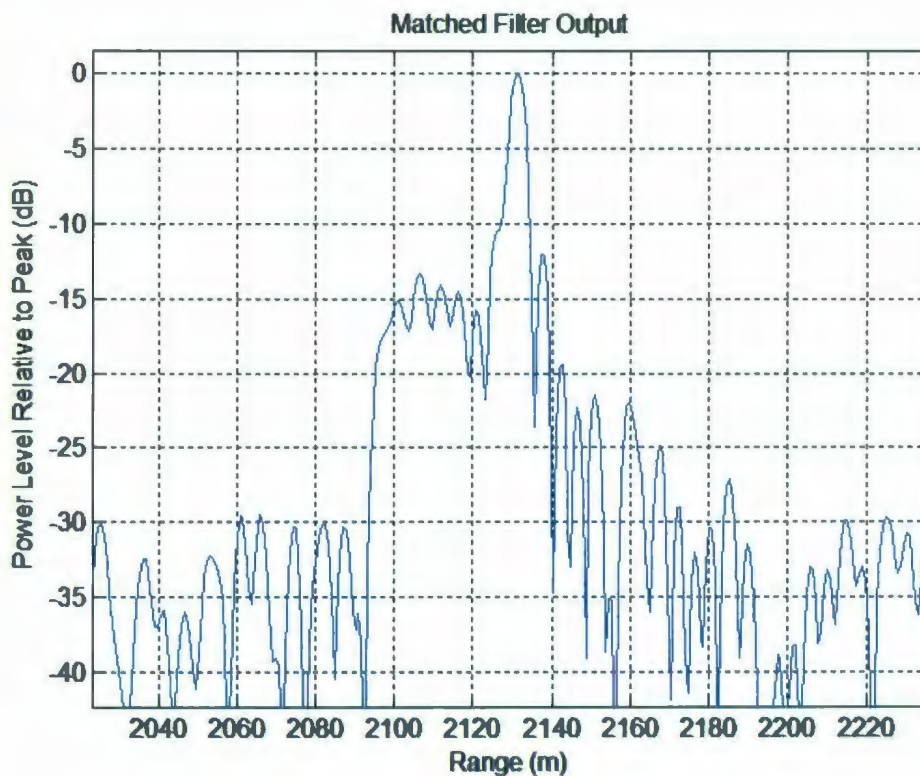


Figure 5-12: Radar Response for Bell Island Ferry (Zoomed)

Two system artifacts are also evident in Figure 5-11. The first is the spike that appears at range 0m. This is due to the energy that is reflected from the antenna back into the receiver due to transmitter-antenna mismatch (an inherent quality of all transmitter-antenna combinations). This is a very useful quality actually as it provides a 0m reference that would otherwise be difficult to isolate in the presence of system propagation delays.

The other artifact is manifested by the energy surrounding the ferry target, highlighted by the grey rectangle. The transmitted pulse is actually 1500 m in length. Due to the nature of the pulse compression algorithm, sidelobes result in the output on either side of the peak response over a range equal to the pulse width, or 750 m on either side of the peak. This artifact highlights an important constraint of systems that use pulse compression to achieve high resolution. Small targets in the vicinity of large targets can be obscured by the large target sidelobe energy. Also, sidelobe energy can sometimes be misinterpreted as a real target. In this particular case, the sidelobe energy is more severe than that of a specular target because of the diffuse nature of the signal return. Furthermore, because this is a moving target, the sidelobe energy is distributed differently from that of a static target. These issues will become more evident in further sections—this example simply serves to highlight the issues. It's important to realize that issues related to sidelobe energy can be dealt with to avoid misinterpretation, through appropriate post-processing of the output (for example through consideration of the composite of many signal returns).

5.4.2 Standard Target Assessment—Paddy's Pond

The Paddy's Pond field site served to assess the methodology proposed for the ocean phase involving the use of a Lunberg Lens as a standard target. Before configuring the Lens for an ocean environment, it was important to learn whether the radar could *see* this target under a very controlled environment provided by the frozen lake.

The early work at Paddy's Pond failed in providing detection of the Lens (but for good reason, as clarified later). The Lens (or target) was placed at a range of 1.86 km from the radar, about 200 m from the opposite side of the pond. Data averaged over 10 cycles is shown in Figure 5-13, where clearly there is no distinguishable target at 1.86 km. However, other distinguishing features of this data warrant discussion. There was a small island about half way across the pond that is clearly seen at 900 m. The pond edge is just over 2 km from the radar and is clearly seen in the data. Beyond the pond are mostly heavy trees, with the exception of a transmission line right-of-way void of trees, as indicated in the figure; this region is arguably visible in the data. In the distance, a

hillside rises above the foreground, detected by the radar as shown. The last target is a water tower installation in Conception Bay South (CBS); this being a large steel structure, it presents itself as a very strong target. One other target is evident at about 500 m. Even though there was no physical target in boresight at this range, there were several large buildings about 90 degrees from boresight, and it was verified these targets in the data are a consequence of scatter received from an antenna sidelobe.

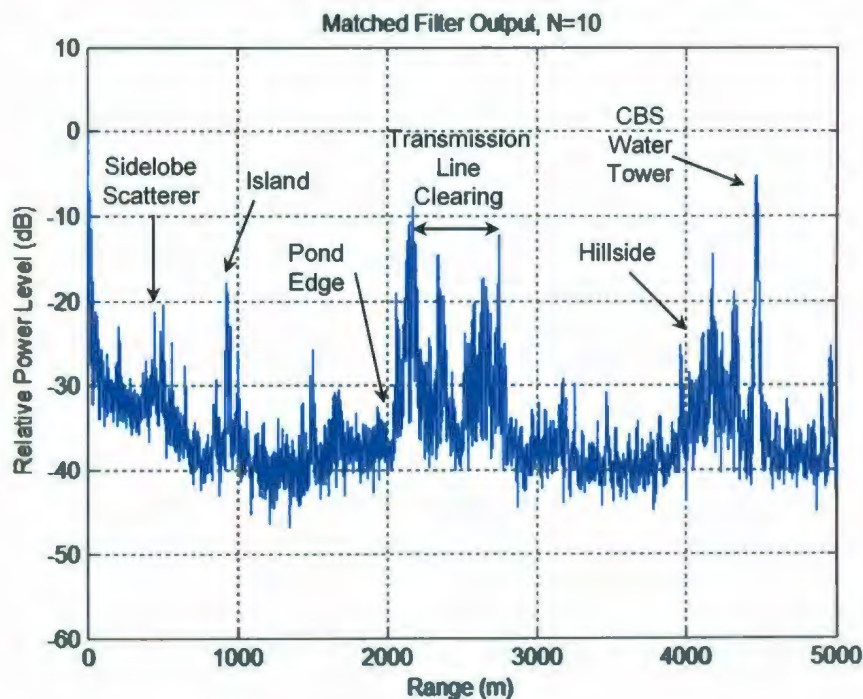


Figure 5-13: Paddy's Pond Data with Various Targets

One other notable observation is illustrated by Figure 5-14 and Figure 5-15, which shows data sets (zoomed in range) for the radar pointed towards a steel support structure on the transmission line right-of-way and pointed just away from this structure, respectively. The support structure is clearly detectable by comparing these two data sets.

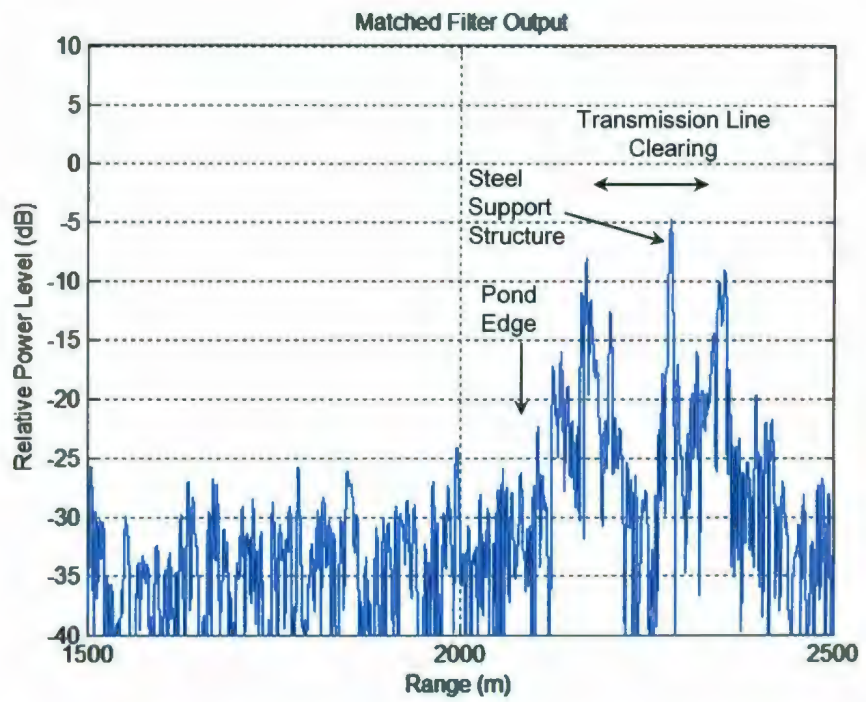


Figure 5-14: Paddy's Pond Data with Power Line Structure at Boresight

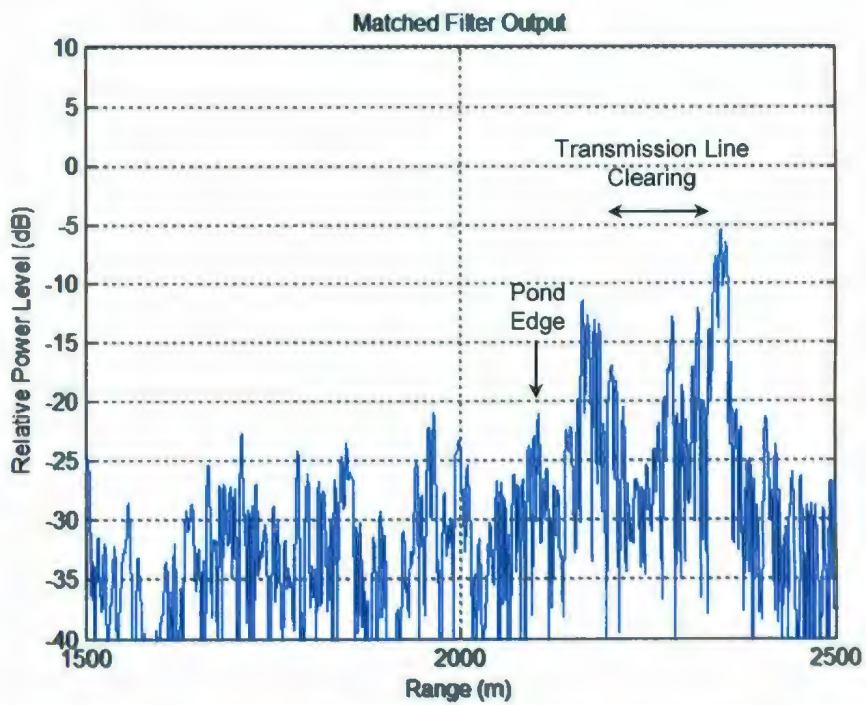


Figure 5-15: Paddy's Pond Data with Power Line Structure outside Boresight

After careful analysis it became clear that the target (the Lunberg Lens) was not visible due to a near-far phenomenon. Because the target was placed in close proximity to the pond edge and associated vegetation—well within a pulse length—reflected energy from the pond edge overlapped that of the target. The pond edge forms a large target because the radar illuminates approximately 150 m of the shoreline at 2 km range. The sidelobe energy resulting from the matched filter is therefore significant enough to mask out the relatively small target response of the Lens. To test this hypothesis, the target was moved to a location in the pond that was clear of any potential sidelobe effects of nearby targets. This could only be accomplished with a short pulse width (1 μ s) and the target was positioned much closer to the radar to make up for the lower energy associated with the narrow pulse width.

A data set corresponding to a target range of 575 m and a pulse width of 1 μ s is shown in Figure 5-16. The standard target is very clear in this particular result. The sidelobes are also very well defined—almost ideal. This response exemplifies a specular reflector—one that produces a single reflection (analogous to the surface of a mirror).

The theoretical range resolution of any radar (described earlier) is related to its bandwidth, and in this case can be predicted as follows:

$$\Delta R = \frac{c}{2 \cdot BW} = 3 \times 10^8 \text{ m/s} / 2 \times 35 \text{ MHz} = 4.3 \text{ m}$$

As Figure 5-17 shows, the radar yields a range resolution that nearly identically matches the theoretical resolution of 4.3 m. This measurement is taken at the -3 dB level as shown. The first sidelobes for the signal design employed by the radar should appear at -13 dB; this result shows the sidelobes to be within 1.5 dB of this level.

One particular interesting result from this phase of experimentation is shown in Figure 5-18. Here, the standard target remains at 575 m, as in the previous example. However, a field technician positioned himself about 50 m in front of the target. His reflection is very clear in the figure.

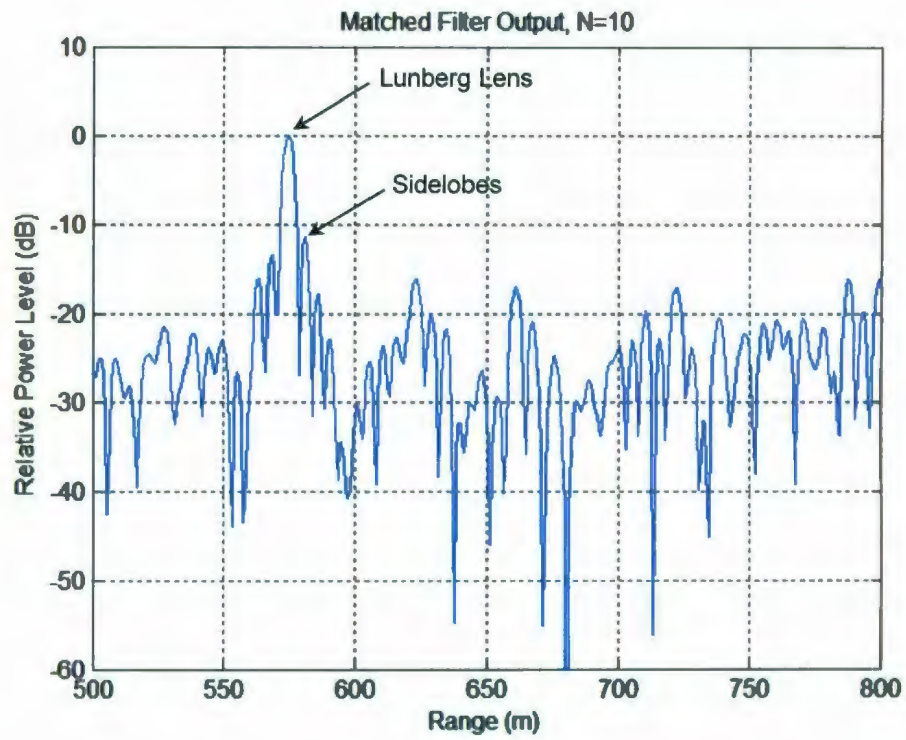


Figure 5-16: Lunberg Lens at 575 m, Pulse Width 1 μ s

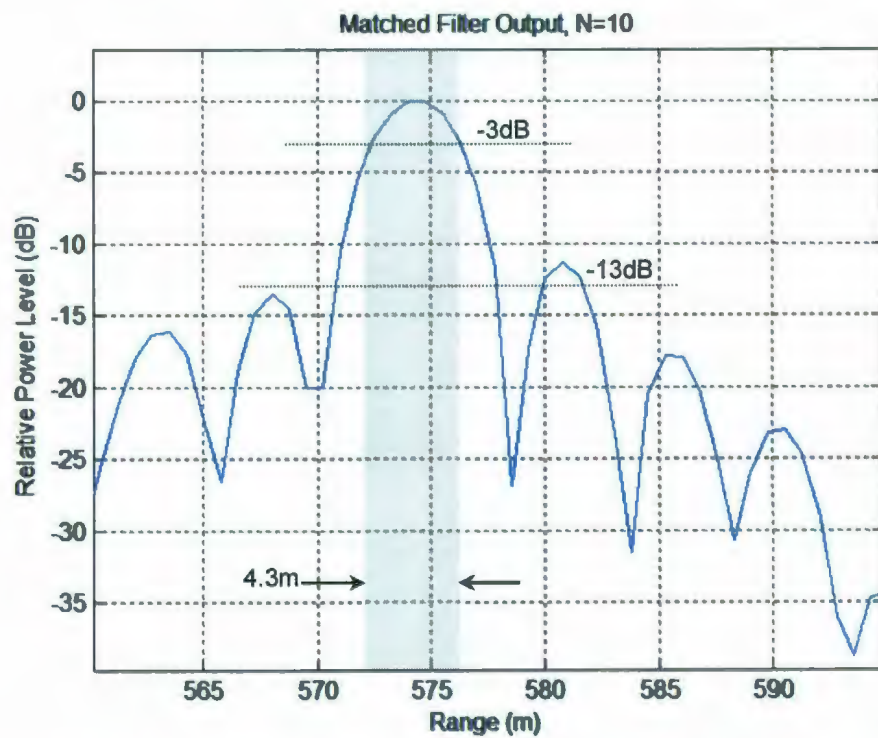


Figure 5-17: Range Resolution Illustration (Figure 5-16 Zoomed)

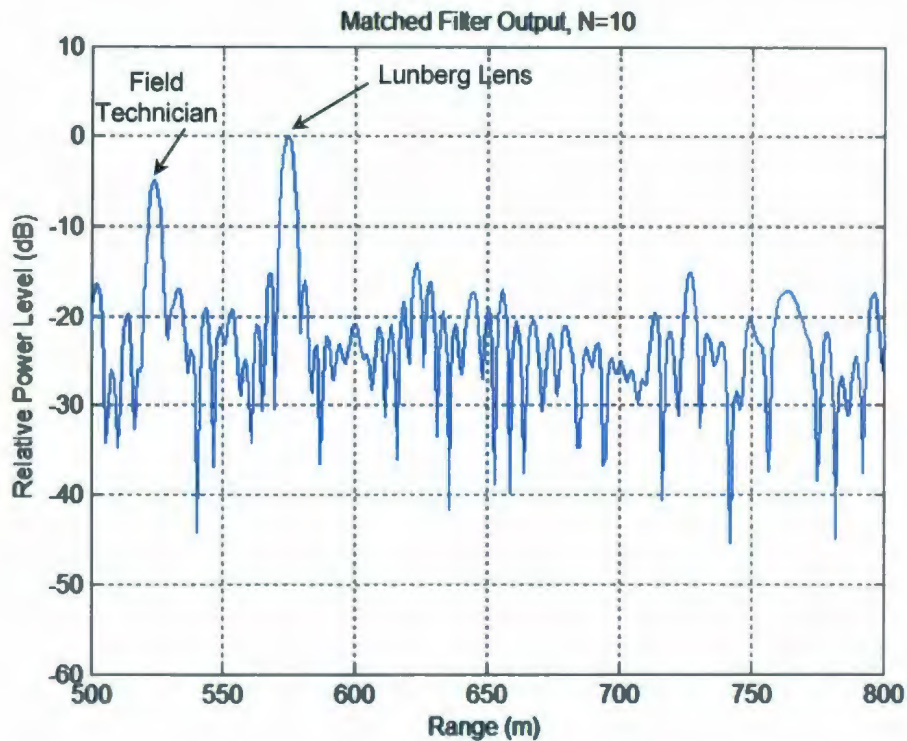


Figure 5-18: Radar Data Showing a Person Standing near Standard Target

The last activity at the Paddy's Pond site was an investigation into the detection of target velocity. To facilitate this experiment, a field technician held the reflector in his hands and proceeded to walk towards the radar. The pseudo-color plots shown in Figure 5-19 through Figure 5-22 show the Range-Doppler response of the target as it progresses from a stationary position to progressively increasing velocities while approaching the radar. These velocities are consistent with those observed by the technician on a hand-held GPS receiver.

The radar parameters were as follows: pulse width, $\tau_p=1 \mu\text{s}$; pulse period, $T_p=100 \mu\text{s}$; number of pulses, $N_p=36$; number of cycles, $N_c=10$; and bandwidth, $B=35\text{MHz}$. These figures also exemplify the velocity resolving capability of the radar. From the discussion of Section 2.2, the theoretical velocity resolution for the signal parameters applied during this experiment is 1.7 m/s. The dark red region of the target approximately represents the 3 dB boundaries that are used to characterize both range and velocity resolution. Clearly, the velocity resolution is very close to the theoretical value.

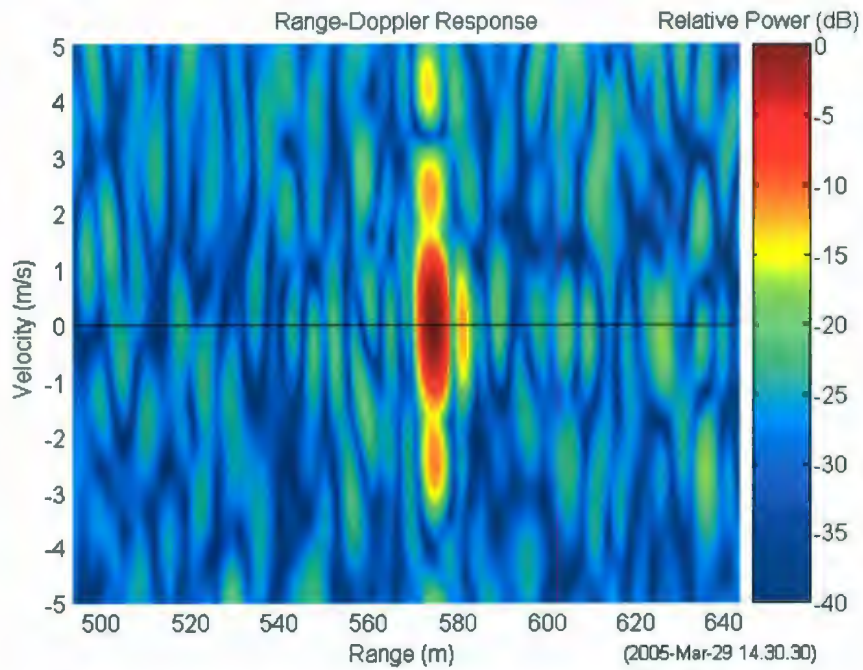


Figure 5-19: Range-Doppler Response for Stationary Target

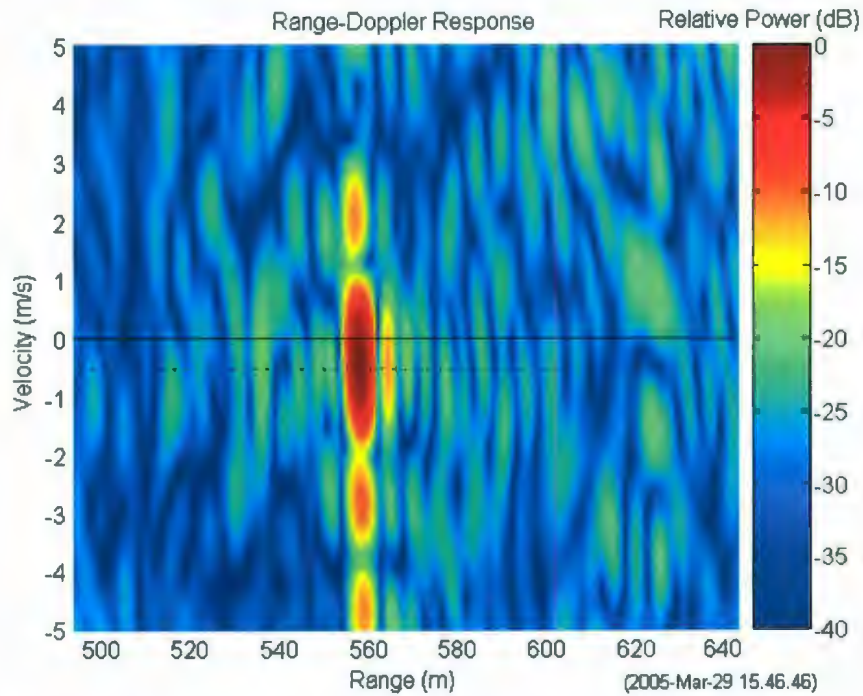


Figure 5-20: Range-Doppler Response for Moving Target (frame 1)

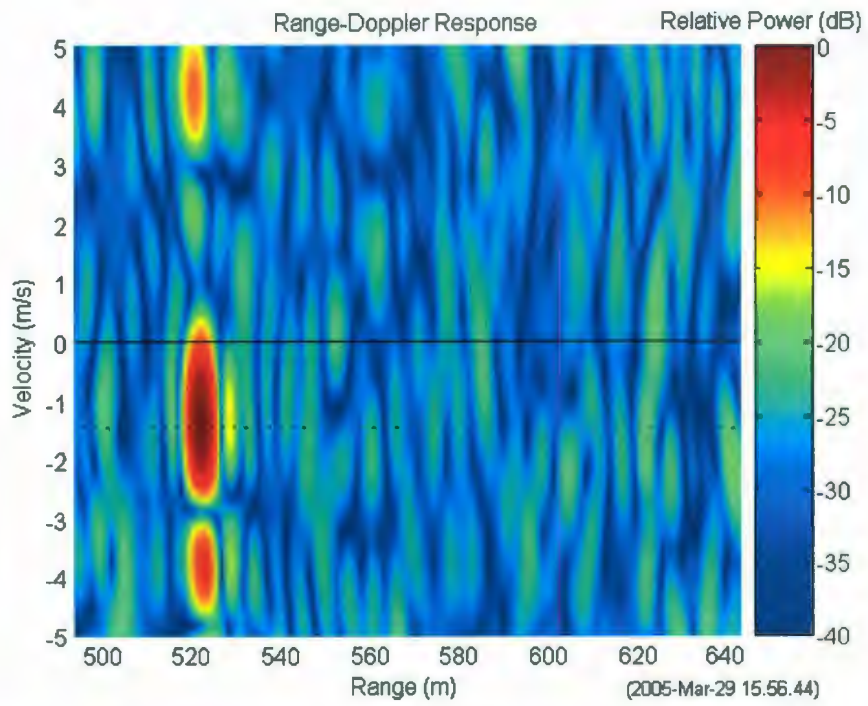


Figure 5-21: Range-Doppler Response for Moving Target (frame 2)

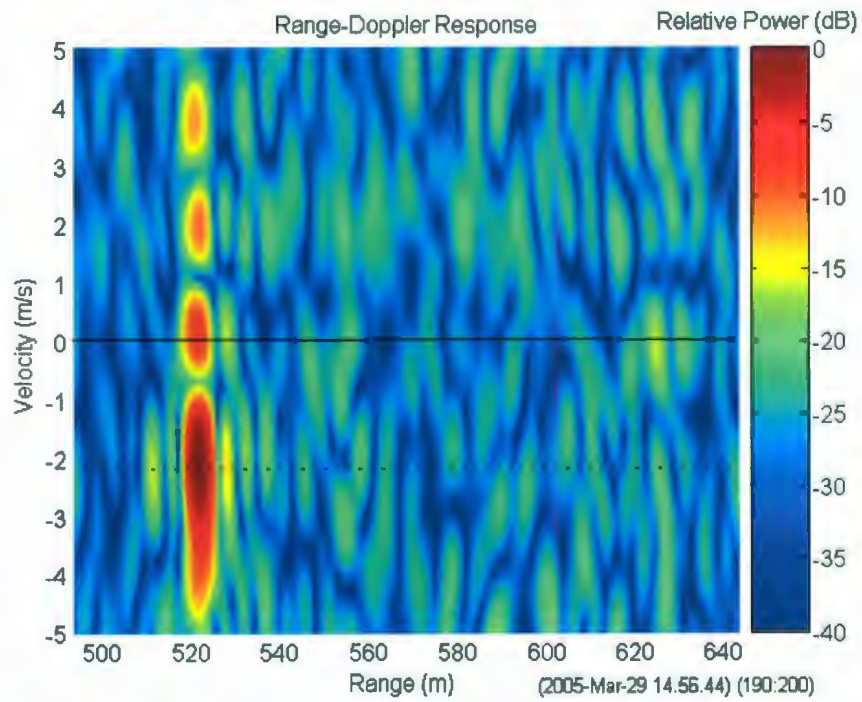


Figure 5-22: Range-Doppler Response for Moving Target (frame 3)

5.4.3 Ocean Evaluation

The ocean component of the field work, which took place in Motion Bay, used the Lunberg Lens configured atop an ORT buoy and placed in the ocean at a range of approximately 1800 m from the radar site. The first attempt at target detection was carried out unsuccessfully from the Petty Harbour breakwater, where an antenna height above sea level of just 3 m affected target visibility, preventing sufficient target backscatter for detect-ability. The antenna site was relocated to a position just outside the Petty Harbour entrance at approximately 20 m above sea level. From this position, the propagation problems were overcome and the target was detectable. A typical Range-Doppler profile for the target in this environment is shown in Figure 5-23, for the following radar parameters: pulse width, $\tau_p=5 \mu\text{s}$; pulse period, $T_p=100 \mu\text{s}$; number of pulses, $N_p=176$; number of cycles, $N_c=10$; and bandwidth, $B=35 \text{ MHz}$. There are a couple of noteworthy features in this figure. First, the target has a small radial component of velocity of about 0.5 m/s. This is quite real and is due to target movement induced by surface action. The figure basically represents a snapshot of the target's location and radial velocity with respect to the radar for a period of 17.6 ms. Figure 5-24 shows that another *snapshot* reveals a slightly different position and velocity, due to continued and varied target movement induced by surface action. The second noteworthy feature is that the velocity ambiguities are quite clear. What they suggest, for this particular radar configuration, is that a target moving at approximately 3.5 m/s, or any multiple thereof, can not be distinguished from a stationary target. This exemplifies the need for selecting radar parameters specific to the application. For instance, if it is known that all freely floating targets have velocities less than 3 m/s, then these ambiguities are irrelevant. Otherwise, other information such as target tracking from successive detections can help resolve velocity ambiguities.

Comparing both figures, a final observation is that the background noise and/or clutter appear to be weaker in the second image. This is actually an artifact of the manner in which the data is presented. The data is plotted as a *relative* power level with respect to the maximum signal level in the image. Therefore, the second figure doesn't have lower background noise/clutter, but instead has a stronger peak response from the target.

Variability in target response can be expected in such a dynamic environment where the target is being subjected to wave motion. In this situation, the target experiences rapidly changing accelerations; whereas, the best target response is elicited from situations where the target velocity is constant (including, but not limited to being stationary). So in essence, the coherence of the target breaks down, or in other words, the target looks very different from pulse to pulse, causing the integration of many pulses to be sub-optimal.

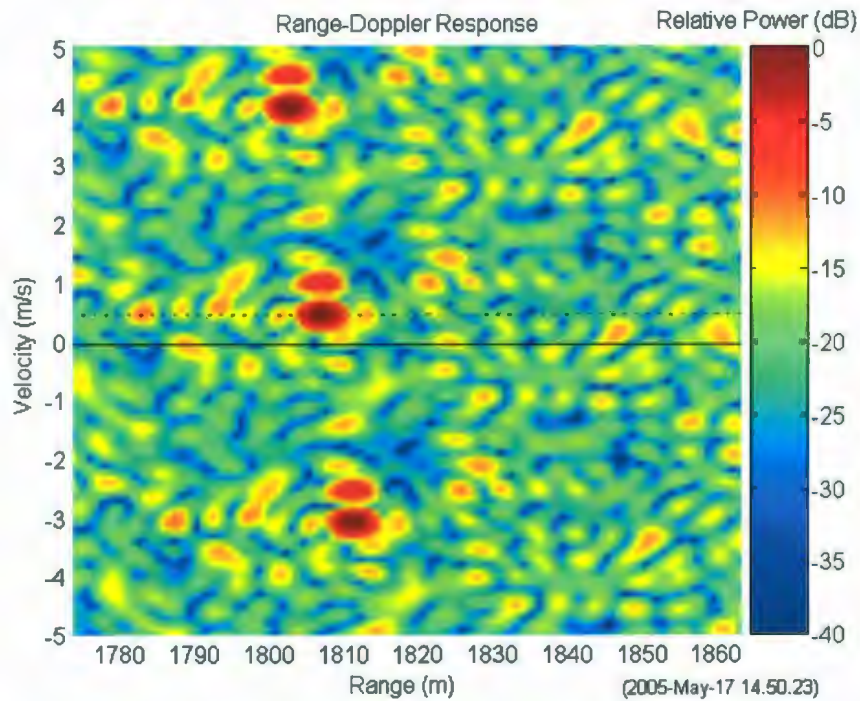


Figure 5-23: Typical Range-Doppler Response for Moored Target

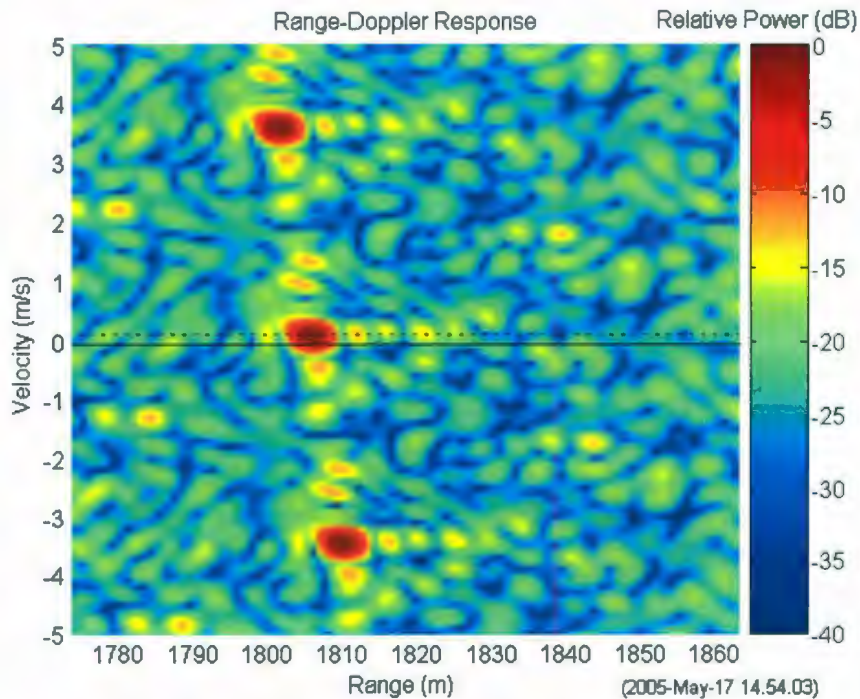


Figure 5-24: A Second Range-Doppler Response for Moored Target

Figure 5-25 shows a result obtained when two fishing vessels happened to cross over the path of the radar beam. This example demonstrates the utility of Range-Doppler processing for distinguishing between static and moving targets. This particular plot is thresholded at -20 dB to mask much of the clutter. It's easily seen that the radial component of velocity of the vessels is about 1 m/s and 2 m/s, for vessel #1 and vessel #2, respectively. The absolute response levels of each of the vessels appear to be weak relative to the Lens; this is simply because the vessels were not in the radar beam center at the time of acquisition. Also evident in the figure are the Doppler ambiguities at approximately -2.5 m/s and -1.5 m/s. In fact it's not clear whether these are indeed the actual radial velocities of the vessels. It's important then to understand the expected velocity extent of targets under consideration and the ambiguities associated with the chosen radar signal parameters so that ambiguities can be reconciled.

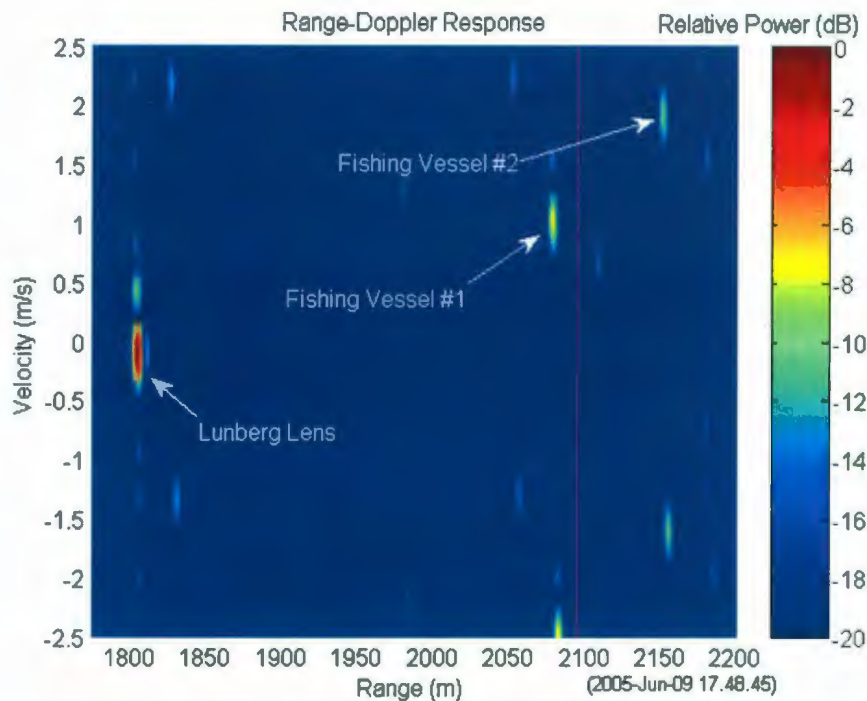


Figure 5-25: Range-Doppler Response with Two Fishing Vessels in Background

The ocean environment presents a drastically different situation for target detection than the environment of the previous section. Two factors weigh heavily into detection performance—sea clutter and target movement. Sea clutter, although not noise-like, degrades the sensitivity of the radar receiver to real targets in much the same way that noise can mask a real signal. Target movement presents a problem that is rather unique to coherent radar. Coherent integration, be it pulse averaging or pulse compression, relies upon consistent signal phase throughout each pulse and from pulse to pulse. When the target is subjected to surface action, it experiences various radial accelerations with respect to the radar. These accelerations result in phase inconsistencies that degrade the integrated output of the detection process. This factor is exemplified in Figure 5-26. Here, the nominal velocity of the target was determined from a Range-Doppler plot to be 0.15 m/s, and the matched filter response for this particular velocity is shown for each of ten cycles. The coherent (complex) sum of the ten cycles is represented by the red line. The variability in both amplitude and phase is evident—a perfectly stationary target would exhibit matching phase across all ten cycles.

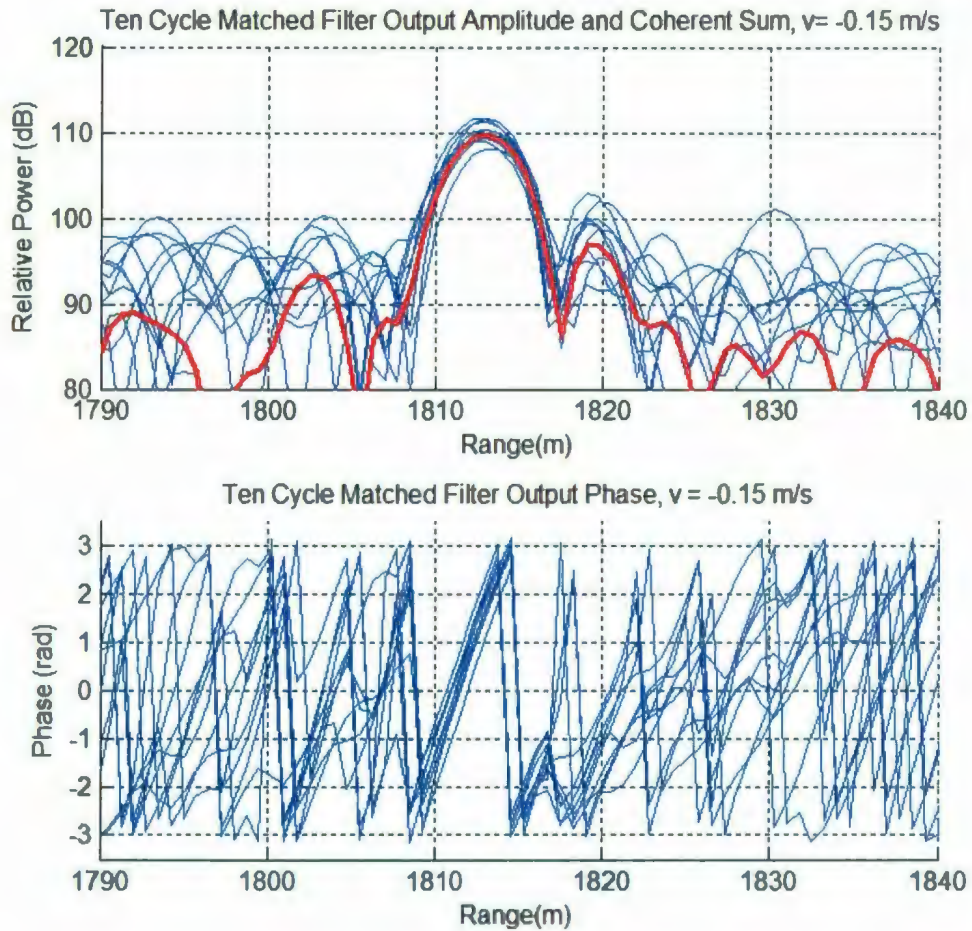


Figure 5-26: Multi-Cycle Response from Moored Target

Figure 5-27 shows the effect of processing the matched filter assuming an erroneous target velocity of -2.0 m/s. It is seen here that the phases are not matched from cycle to cycle, which results in a substantial decrease in the coherent sum. The individual cycle responses, however, are very similar to the previous case. The reason for this is that over the duration of a single cycle, the Doppler resolution is very poor (approximately 17 m/s); therefore, there is no appreciable change in response from -0.15 m/s to -2.0 m/s.

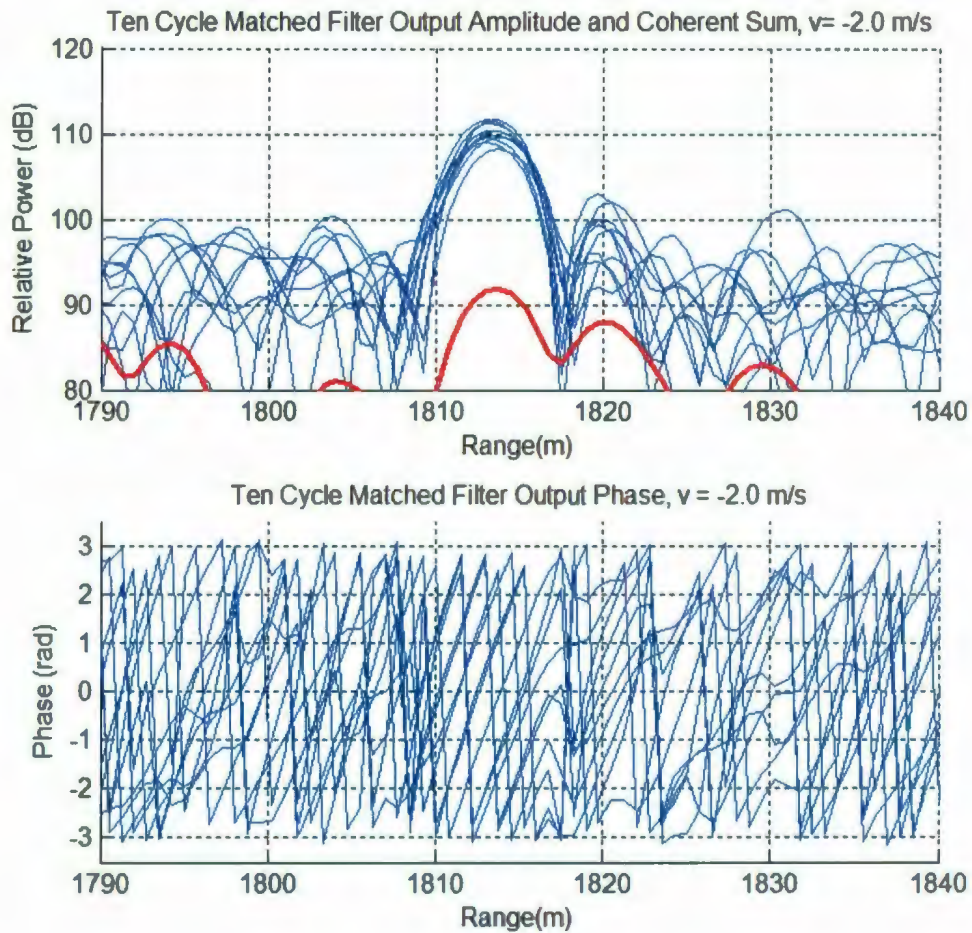


Figure 5-27: Multi-Cycle Response from Moored Target w/ Velocity Error

There are two further points to be made with respect to the above figures. First, these figures exemplify the degree of control over phase that is required in operational coherent radar. The total duration of this 10-cycle data set is 36 ms. Phase must be controlled and known over this time period in order to correctly integrate the data to produce the pulse compression evident in the figures. Second, Figure 5-26 shows the improvement in SNR resulting from the integration of multiple cycles. Because the noise is uncorrelated from cycle to cycle, the coherent sum of 10 cycles should result in an improvement in SNR of $10\log(10)$, or 10 dB, which is approximately the case in this example. Note that the range resolution is a function of bandwidth, which does not change by introducing multiple cycles.

6. Considerations for an Operational Coherent Radar

Commercial opportunities exist for moderate cost, high performance radar. Breaking into the low-cost commercial navigational radar market is very challenging, where economies of scale make it a very competitive arena. In the short term, the more promising opportunities possibly exist in non-traditional markets—for example, detection of small-scale navigational hazards (such as ice), search and rescue, and security surveillance. As discussed earlier, and demonstrated by this research program, high performance is attainable by utilizing emerging technologies—most notably, medium-power linear power amplifiers (100-watt class), ultra-stable frequency synthesizers, high-bandwidth processing platforms, and improved microwave devices.

The existing prototype was designed to validate specific qualities of coherent radar, such as range and Doppler resolution, in a focused manner that did not place any consideration on specific applications. In order to move the research presented in this thesis towards a commercial presence, a prototype is required that can be placed in real operational scenarios and evaluated by real users and applications. This effort will require the following major elements, not present in the existing prototype:

1. support for a scanning antenna;
2. an integrated transceiver; and,
3. a real-time processing platform.

This chapter briefly discusses recommended approaches and anticipated challenges for each of these elements. This is followed by an analysis of radar parameters in the context of an operational system.

6.1 *Element of an Operational Radar*

6.1.1 Antenna Scanning

Whereas the current prototype supports only a single, manually configurable, look direction, most operational radars require broad spatial coverage that is generally provided by a rotating, or scanning, antenna. This presents a number of design issues and trade-offs that must be considered. The antenna beamwidth governs the azimuth resolution, which increases with increasing range. The wider the beamwidth, the coarser

the azimuth resolution, the larger the temporal spacing between transmissions, and the faster the antenna can scan. Conversely, the narrower the beamwidth, the finer the azimuth resolution, the smaller the temporal spacing between transmissions, and the slower the antenna can scan. Some of the associated trade-offs will become evident in Section 6.2.

The antenna type is a second consideration. The slotted waveguide design in the current prototype is one possibility—adapted to a rotating platform. Alternatively, the antenna may comprise an array of electrically-fed radiating elements. In both cases, each slot or radiating element may be *weighted* in such a way as to provide some desired beam-shape and sidelobe structure. The narrowest beamwidth is governed by the overall length of the antenna aperture according to the approximation in equation (6-1). The electrically fed elements provide a convenient means of modifying the beam-pattern dynamically to accommodate different operational scenarios.

$$BW_{3dB} \approx \lambda/L \quad (6-1)$$

where

L is the length of the antenna or antenna array.

A third possibility for an antenna is a fixed array of electrically fed radiating elements, whereby scanning is accomplished through electronically steering the array (commonly called a *phased array*). This approach eliminates much of the mechanical complexity and maintenance of a rotating platform, but generally, the spatial coverage is limited to much less than 360°. Furthermore, phased arrays have sidelobe structures that are not fixed, but vary according the beam direction. As the beam is steered away from broadside, a large artifact in the sidelobe structure will begin to appear, known as a *grating lobe*.

There are significant performance and cost trade-offs associated with the antenna types discussed above—well beyond the scope of this thesis. Suffice to say, a trade-off analysis will become a critical component of the design specification for an operational prototype.

Antenna scanning not only places requirements on the antenna, but also places severe demands on the back-end data paths and processor(s) to sustain data flow and calculate the ambiguity responses for each and every signal transmission. This will be a major component of the investigative phase for an operational radar.

6.1.2 Integrated Transceiver

The current radar prototype was constructed purely from connectorized modular components in order to speed up development and provide flexibility in debugging and modifying the design. This is not cost-effective for a commercial design; therefore, the operational radar should, to a large extent, be integrated. A proposed structure is shown in Figure 6-1. This structure is similar in function to that presented in Figure 4-11, but demonstrates the portion of the design that is proposed to be implemented in a highly integrated manner on a printed circuit board (PCB) (or boards). The PCB would comprise all clock-generation elements, the DDS and the microcontroller—essentially all baseband elements and those just bridging the gap into the microwave domain. To mitigate development risk for a first commercial release, microwave amplifiers, filters, mixers and other specialized microwave devices, would remain in original equipment manufactured (OEM) connectorized format. In the long term, a manufacturer may also consider integrating these components as well to improve profitability, but the proposed structure is deemed suitable to initially enter certain identified markets.

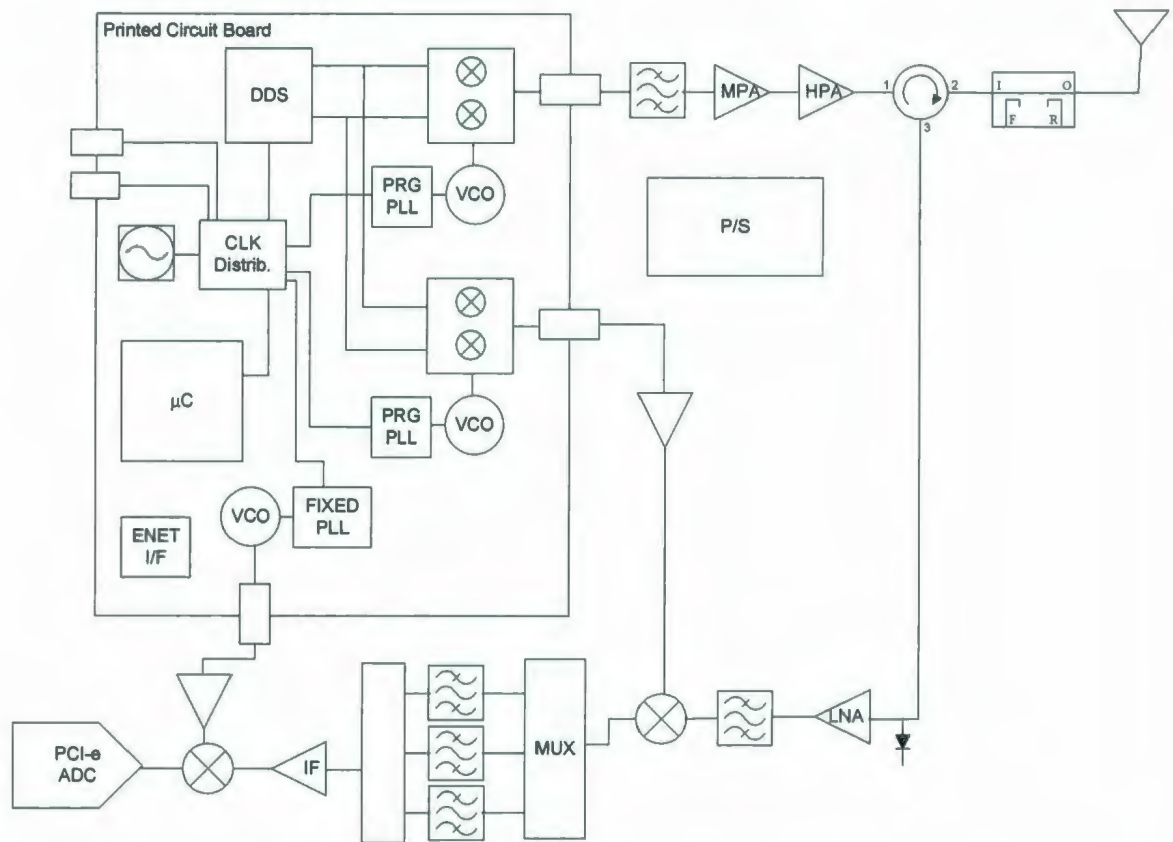


Figure 6-1: Commercial Coherent Radar Concept

6.1.3 Real-Time Processing Platform

Most operational radars require real-time, or near-real-time rendering of detected output to the user. The current prototype only provides storage of digitized baseband data and uses off-line processing to compute the ambiguity response. For an operational radar, a real-time processing platform will need to be specified. The details in specifying such a platform is beyond the scope of this thesis, but one point is worth noting. Traditionally, real-time platforms for similar applications have been the exclusive domain of digital signal processing (DSP) platforms whose architectures are specifically optimized for signal processing operations such as fast Fourier transforms (FFTs). The downside of these platforms is that they are typically esoteric and algorithms implemented on one platform are rarely (at least directly) portable to another. General purpose processors such as PC platforms have been inefficient at carrying out DSP operations—until recently. Today, many arguments support the use of x86-based general

purpose processors for applications traditionally reserved for DSP [26]. One reason for this is the DSP-like enhancements that have been made to the x86 such as superscalar execution (parallel execution units) and pipelining. To make an appropriate architecture choice for DSP, four design principles, besides raw speed, must be addressed: scalability, versatility, density and programmability—all of which can result in favoring the use of a PC. Furthermore, PCs have traditionally been inadequate for moving large amounts of data, from the perspective of both speed and predictable latencies. However, the current trend is towards high-speed serial, multi-lane, point-to-point communications fabrics, such as PCI Express. Such enhancements to the PC provide a much more viable general-purpose platform than previously possible.

6.2 Analysis of Radar Parameters

This section provides a first order analysis of how radar parameters for a scanning SFM-based coherent radar may be chosen and optimized for certain applications. This analysis is not intended to be comprehensive, but instead an example of the analytical process needed to realize an SFM-based radar for any given application.

The adage “you can’t get something for nothing” certainly applies to radar. Undoubtedly, pulse compression methods can take a signal buried in noise and render a large SNR—seemingly something for nothing. However, prior to compression, the signal is spread over a long duration in time, whereas following compression, the signal is confined to a very short time interval. The adage holds true because of conservation of energy. And energy, which is the integral of signal power over the duration of the signal, is the constant that forms the root of the analysis presented below.

This analysis is required in the interest of defining the parameters of an SFM-based radar that would provide equivalent performance to that of a pulsed magnetron radar, or some measure of improvement. The baseline of comparison is energy. The following constants are first defined and set equal across both types of radar:

Scan Rate (ψ_{rpm}): The rotation rate of the antenna, given in revolutions per minute (RPM).

Azimuth Beamwidth (θ_a): The angle between the two half-power (-3dB) points of the main lobe of the antenna in azimuth ($^\circ$).

Carrier Frequency (f_c): The frequency of the radiated waveform carrier (MHz).

Bandwidth (B): The width of the frequency range (MHz) over which the antenna radiates *most* of the power presented at its feedpoint (e.g. VSWR of the antenna is smaller than say 2).

The following two parameters are relevant only for the pulsed radar (from which energy can be computed):

Baseline Peak Power (P_b): Pulsed radar peak transmit power (kW).

Baseline Pulse Width (τ_b): Pulsed radar pulse width (μs).

The next two parameters are relevant only for the SFM-based radar:

SFM Output Power (P_o): SFM-based radar peak transmit power (W).

Improvement Factor (F): Ratio of signal energy in SFM-based radar compared to pulsed radar.

The following computed parameters complete the fixed parameter set used in the analysis:

Baseline Energy (E): Total energy in the pulsed radar waveform:

$$E = P_b \cdot \tau_b \quad (\text{W}) \quad (6-2)$$

Scan Rate (ψ_a): The rotational rate of the antenna expressed in degrees/s:

$$\psi_a = \psi_{\text{rpm}} \times \frac{360}{60} \quad (^\circ/\text{s}) \quad (6-3)$$

Illumination Time (T_{ii}): The duration over which the antenna will illuminate a point target while scanning:

$$T_{ii} = \frac{\theta}{\psi_a} \quad (\text{s}) \quad (6-4)$$

Doppler Resolution (Δv):

$$\Delta v = \frac{c}{2f_c T_{il}} \quad (\text{m/s}) \quad (6-5)$$

Range Resolution (Δr): (previously defined)

$$\Delta r = \frac{c}{2B} \quad (\text{m}) \quad (2-4)$$

A spreadsheet was devised to input the above parameters into a model to determine the operational parameters of an SFM-based radar for different pulse-widths (τ_p). The spreadsheet is shown in Table 6-1. The following operational parameters are computed in the spreadsheet:

Blanking Range (R_{blank}):

$$R_{blank} = \frac{c\tau_p}{2} \quad (\text{m}) \quad (6-6)$$

SFM Frequency Step (Δf):

$$\Delta f = 1/\tau_p \quad (\text{Hz}) \quad (6-7)$$

Total Number of Pulses (N_T):

$$N_T = \frac{E \cdot F}{\tau_p P_{out}} \quad (6-8)$$

Pulse Repetition Frequency (prf):

$$prf = \frac{N_T}{t_{il}} \quad (\text{pps}) \quad (6-9)$$

Number of Waveform Cycles (N_c):

$$N_c = \frac{N_T}{N_p} = \frac{N_T \Delta f}{B} \quad (6-10)$$

Maximum Range (R_{max}):

$$R_{max} = \frac{c}{2 \cdot prf} \quad (\text{m}) \quad (6-11)$$

Table 6-1: SFM Parameter Spreadsheet

Fixed Parameters	Symbol	Value	Units			
Scan Rate	Ψ_{rpm}	24	RPM			
Antenna Beamwidth	θ_a	1.9	deg			
Carrier Frequency	f_c	3	GHz			
Antenna Bandwidth	B	40	MHz			
Baseline Peak Power	P_b	30	kW			
Baseline Pulse Width	τ_b	0.5	μs			
SFM Output Power	P_o	50	W			
Improvement factor	F	1				
Calculated Parameters						
Baseline Energy	E	0.015	J			
Scan Rate	Ψ_a	144	deg/s			
Illumination Time	t_{il}	10	ms			
Doppler Resolution	Δv	5	m/s			
Range Resolution	Δr	3.75	m			
Operational Parameters						
τ_p (μs)	R_{blank} (m)	Δf (MHz)	N_T	prf (Hz)	N_c	R_{max} (m)
0.05	7.5	20	6,000	600,000	3,000.00	250
0.5	75	2	600	60,000	30.00	2,500
2	300	0.5	150	15,000	1.88	10,000
10	1500	0.1	30	3,000	0.08	50,000

For total signal energy E , and input noise power N_o , the maximum SNR at the receiver output is attainable when a matched filter is used, and is given by [19]:

$$SNR_{mf} = \frac{E}{N_o L_m} \quad (6-12)$$

where

L_m is the matching loss of the receiver.

The above relationship implies that regardless of the nature of the radar and its associated waveform, the maximum achievable SNR is fixed by the energy impinging the receiver, and the noise floor. L_m represents the reduction in SNR from the ideal when a perfect matched filter is not implemented. For an improvement factor of unity, one would expect the pulsed radar to yield the same SNR as the SFM-based radar, if the impinging energy at the receiver and the receiver noise floor is the same in both cases. However, in practice, the SFM-based radar would have a matching loss much closer to unity than the non-coherent pulsed radar, and will therefore outperform the pulsed radar for an improvement factor of unity. In the model, the improvement factor can be used to specify an SFM-based receiver that will yield an improvement in SNR equal to the improvement factor.

The example in Table 6-1 can be interpreted as follows. The fixed parameters (with the exception of SFM output power and improvement factor) are taken from a state-of-the-art pulsed-magnetron S-Band radar. The object of the analysis is to determine the parameters of an SFM-based radar that will yield equal performance—so the improvement factor is set to unity. The current state of the art in linear solid state microwave amplifiers, for reasonable cost (i.e. < \$5 K USD), is somewhere on the order of 50 W output power.

For each pulse width scenario: the frequency step (Δf) is calculated directly from the pulse-width, maintaining orthogonality; the number of pulses in the complete waveform (N_T) is determined by considering how many low power pulses are needed to generate total energy equivalent to the pulsed radar; the pulse repetition frequency (prf) is determined by fitting N_T pulses into the illumination period (t_{il}); and, the number of

waveform cycles (N_c) is simply the number of waveform cycles required to generate a total of N_T pulses.

A very important factor that is exemplified in this analysis is the trade-off between blanking range and maximum range. If a short pulse length is chosen to shorten the blanking range (or to see close-in targets), more pulses are required within the illumination period to generate the required energy; therefore, the *prf* increases and the maximum range (R_{max}) decreases. Conversely, if long-range is required, then the *prf* must be reduced, thereby necessitating a longer pulse width to maintain the same energy. So the parameter set must be chosen to meet the specific target detection requirements. Notice in this example that to obtain a range of 50 km, only a fraction (0.08) of a complete waveform cycle can be transmitted. This effects an additional cost in terms of resolution, since the entire bandwidth is not transmitted.

One last note about regarding this specific example is that although the two radars under comparison are equal in terms of energy (and thus signal detectability), they are not equal in terms of bandwidth (or equivalently, range resolution).

7. Conclusions and Recommendations

As stated in the introduction, this thesis is intended to be a single reference in which future development of an SFM-based coherent radar, and possibly commercialization, can be rooted. To this end, five major areas have been treated as follows: basic radar fundamentals that are relevant to SFM-based coherent radar development; an introduction and detailed assessment of multi-cycle SFM waveforms, with much emphasis on the ambiguity responses associated with various parameter sets; a presentation of design details and signal processing algorithms for a functional coherent radar prototype; experimental data obtained in the field with the prototype; and, a discussion of considerations relevant to bringing all of the above efforts into a new radar prototype that is in operational form, suitable for commercial exploitation.

The detailed treatment of multi-cycle SFM waveforms in Chapter 3 provides much-needed insight into applying these waveforms in practice. A pulse-magnetron radar only has the flexibility to modify pulse width, but the SFM approach offers the flexibility to modify pulse width, pulse repetition interval, cycle iterations and bandwidth, resulting in diverse signal set. This may add an extra level of complexity when put in commercial form, but such diversity carries the benefit of improving detection probabilities and providing a system that can adapt to many different environments and applications. The ambiguity diagrams provided in this thesis, particularly the generalized forms, provide a tool for sorting through this complexity and understanding the implications of modifying each parameter. Undoubtedly, the manifestation of a commercial SFM-based radar may be significantly different than conventional radar; so, understanding the trade-offs within waveform design is paramount to rendering a useable form of the radar to users.

Chapter 4 clearly shows that in coherent radar hardware design, careful attention must be paid to sources of phase noise. It was demonstrated that while phase noise can degrade the ambiguity response from its ideal and diminish SNR, device specifications and design principals can be readily applied to yield deterministic performance predictions. The hardware, also presented in Chapter 4, was a successful implementation that needs little modification at the high architectural level. At a lower level of detailed design however, future design iterations should pay attention to the following points:

1. DDS technology provides a very powerful and highly integrated form of signal synthesis that is an extremely good fit for multi-cycle SFM generation. Over recent years (and since this particular radar prototype was developed) a plethora of new DDS devices have become available, all of which should be explored in the next design iteration. Programmability on-the-fly will remain an important feature to provide a means of exploring new waveform designs. A DDS that provides a gated output would also be of significant benefit to eliminating carrier feed-through while the radar is not transmitting.
2. It was found that for a single antenna circulator-based radar, a gated power amp would be very beneficial so that noise originating from the power amp is not coupled into the receiver path through the circulator, thereby compromising sensitivity.
3. To accommodate a diverse signal set where, among other parameters, the pulse width is varied, a bank of IF filters may be considered to optimize the sensitivity for each pulse width.
4. The demodulator block in the receiver path provides an option to employ I and Q generation in the analog domain. While not as *perfect* as that which can be generated in the digital domain, it does reduce the processing burden in the digital domain, and although a second ADC is needed, each ADC operates at one-half the rate required for a single channel acquisition.
5. Recent advances in PC-bus technology—specifically PCIexpress—are enabling the possibility of using PC platforms for real-time scanning radar platforms. Because of the versatility and broad support associated with the PC, this platform should be given serious consideration in future design iterations.
6. An operational radar will require near-real-time processing in order to render meaningful output to the user. Such processing was not a subject of this study, but will require serious consideration for the implementation of an operation form of coherent radar.
7. A custom antenna was designed for the prototype; however, this was largely done to accommodate working in the ISM band (2.4 GHz). Future development is

anticipated in marine S-Band (3.1 GHz), and it is very likely that readily available commercial scanning antennas would be utilized.

The field program, presented in Chapter 5, was successful in that the resolution capability of the radar, both with respect to range and Doppler, matched the predictions from both theory and simulation. The study highlighted the importance of maintaining a high degree of coherence across the system to achieve these performance objectives. Specifically it was shown in real field data how phase information must be consistent from pulse to pulse, and cycle to cycle, to maximize the integrated response of the target. Furthermore, it was illustrated that target coherence is also a contributing factor to the integrated target response. Understanding the nature of the target dynamics is important for selecting signal parameters. For instance, selecting parameters associated with very high velocity resolution (i.e. a long duration signal) may be detrimental in cases where the target is unable to maintain coherence over a long time interval. For the purposes of a life-craft search for instance, target velocity is of little importance compared with target detection, and signal parameters should be chosen only to optimize detection.

Finally, Chapter 6 emphasizes that an operational form of the coherent radar prototype will require substantial design effort, particularly with respect to azimuth scanning, integration, and real-time processing. The model presented in Chapter 6 is a useful tool for understanding the tradeoffs and limitations associated with SFM-based radar. One particularly interesting outcome of the modeling example is that the SFM waveform does not lend itself, simultaneously, to target detection at both short range and long range, and that the signal parameters can only be optimized for one or the other. Operationally, this implies that if both near range and far range data is needed, strategies must be decided upon to render such data to the user (e.g., alternate the parameter set in successive scans).

The prototype developed during this study was specifically geared towards answering certain research questions; consequently, many features typical of an operational radar were omitted. To move the coherent radar concept presented in this thesis into the commercial realm, a number of objectives should be addressed, as follows:

1. A field trial is needed comprising real targets and extreme environments to provide tangible feedback as to the utility of the coherent radar in specific applications under a wide variety of sea conditions. Ryan [27] is an excellent source of guidance on the assessment of radar performance against varying sea states and grazing angles (albeit based on non-coherent data).
2. Currently, the pulse-compression algorithm is a post-processed event. In order to realize a commercial product, an investigation is needed into the real-time processing requirements of this algorithm to match the scan and update rates of an operational system.
3. A new iteration of the prototype is needed in near-commercial form—ideally in a form that can be placed in real applications as a demonstration. Elements of this design will likely include: highly integrated transmitter and receiver boards (as opposed to the current modular prototyping approach); operation at marine radar S-band (3.05 GHz); compliance with emerging (International Electrotechnical Commission) IEC standards for shipborne radar; azimuth scanning; and a new direct digital synthesis (DDS) device with a gated output capability to eliminate carrier coupling between the transmitter and receiver.
4. To complete a new design iteration, a detailed requirements specification must be generated that considers both the needs of the market and the unique advantages and constraints of a coherent radar utilizing pulse-compression. The requirements specification should define the radar's operating characteristics, the form factor, the user interface, and performance objectives.
5. Should commercially available scanning antennas prove to be either inadequate or uneconomical, further investigation into the antenna design may be required. One focal point for this investigation should be the minimization of sidelobes. Suitable simulation software should be acquired for this purpose as the current design was based purely on theory without the benefit of heuristic methods.
6. An investigation into other signal design techniques might prove beneficial to specific applications by controlling undesired artifacts such as correlation sidelobes, and range and Doppler ambiguities. Such techniques might include

phase coding methods, pseudo-random frequency assignments and non-linear modulation.

Traditionally, coherent radars have been the exclusive domain of high-end, expensive, and purpose-built systems—often military. However, this study demonstrates that technologies supporting economical, but high performance radar have come of age. These technologies will undoubtedly bring the benefits of coherent radar to mainstream applications such as navigation and surveillance. The research provided by this thesis is an important stepping stone towards this realization.

Bibliography

- [1] Barton, David K. "A Half Century of Radar." IEEE Transactions on Microwave Theory and Techniques, Vol. MTT-32, No. 9, September, 1984.
- [2] P. Malloy, "The TWT Amplifier: A Broadband Note," Microwave Product Digest, August, 2002, Available: <http://www.mpdigest.com/Articles/2002/August2002/ampresearch/Default.htm>.
- [3] Wehner, D.R. "High Resolution Radar—Second Edition." Artech House, Inc., Boston, 1995.
- [4] Scheer, J.A., Kurtz, J.L., Editors "Coherent Radar Performance Estimation." Artech House, Inc., Boston, 1993.
- [5] Haykin, S., Krasnor, C., Nohara, T., Currie, B., and Hamburger, D. "A Coherent Dual-Polarized Radar for Studying the Ocean Environment." IEEE Transactions on Geoscience and Remote Sensing, Vol. 29, No. 1, January, 1991.
- [6] Moore, R.K., Raju, G., Xin, W., Davis, C., Demarest, K.R. and Rummer, D.I. "A 150-MHz Coherent Radar System." Proceedings of the 1989 IEEE National Radar Conference, pp 42-47, March 1989.
- [7] Peebles, P.Z. "Radar Principles." John Wiley & Sons, Inc., New York, 1998.
- [8] Lamont-Smith, T., Shepherd, P.W., and Gates, M.R. "Scattering Components from Low Grazing Angle Sea Clutter." 1st EMRS DTC Technical Conference – Edinburgh 2004.
- [9] Chan, H.C. "Evaluation of the FMICW Waveform in HF Surface Wave Radar Applications." Defense Research Establishment Ottawa, Report No. 1219, Ottawa, January 1994.
- [10] Haykin, S. "Communication Systems, Second Edition." John Wiley & Sons, New York, 1983.
- [11] Mohamed, N.J. "Carrier-free radar signal design with MTI Doppler processor." IEE Proceedings-Radar Sonar Navigation, Vol. 141, No. 1, February 1994.
- [12] Mozeson, E., and N. Levanon. "Diverse Radar Pulse-Train with Favourable Autocorrelation and Ambiguity Functions." Radar 2002, pp 172-176, October 2002.
- [13] Zejak, A.J., Simic, I.S., and B.M.Zmic. "Chirp Radar Ambiguity Function Shaping." EUROCON'2001, International Conference on Trends in Communications, pp325-328, Vol. 2, 2001.
- [14] Musa, M., and Salous, S. "Ambiguity elimination in HF FMCW radar systems." IEE Proceedings – Radar, Sonar and Navigation, pp 182-188, Vol. 147, August 2000.
- [15] Mahafza, B.R. "Radar Systems Analysis and Design Using MATLAB®." Chapman & Hall/CRC, Boca Ranton, FL, 2005.

- [16] Curry, G.R. "Radar System Performance Modeling—Second Edition." Artech House, Inc., Norwood, 2005.
- [17] Nathanson, F.E. "Radar Design Principles—Second Edition." McGraw-Hill, Inc., New York, 1991.
- [18] Khan, R.H. and Mitchell, D.K. "Waveform Analysis for High Frequency FMICW Radar." IEE Proceedings-F, Vol. 138, No. 5, October 1991.
- [19] Barton, D.K. "Radar System Analysis and Modelling." Artech House, Inc., Boston, 2005.
- [20] Levanon, N. "Stepped-frequency pulse-train radar signal." IEE Proceedings-Radar Sonar Navigation, Vol. 149, No. 6, December 2002.
- [21] Scheer, J. "Coherent System Performance Estimation." IEEE International Radar Conference. Record of the IEEE 1990 International Radar Conference, pp 125-128, May 1990.
- [22] Khitrovskiy, V.A. "Circuitry and Technological Aspects of Frequency Synthesizers Design for Modern Radar." MSMW'04 Symposium Proceedings, Kharkov, Ukraine, June 21-26, 2004.
- [23] A. Bur-Guy, "add_phase_noise.m," Version 1.5, October 2005, Available: http://www.mathworks.com/matlabcentral/files/8844/add_phase_noise.m.
- [24] Dawood, M. and Narayanan, R.M. "Generalized wideband ambiguity function of a coherent ultrawideband random noise radar." IEE Proceedings-Radar Sonar Navigation, Vol. 150, No. 5, October 2003.
- [25] Rowsell, D., Tarrant, S. (2006). "Coherent UHF Radar for Small Target Detection", Contract Report R-05-013-258, v1.0, April, 2006.
- [26] Peebles, B. "DSP and x86—Getting Past the Hype in Processor Architecture." RTC Magazine, July 2007.
- [27] Ryan, J., and Johnson, M. "Radar Performance Prediction for Target Detection at Sea." Radar 92. International Conference, pp 13-17, October 1992.

Appendix A: Derivations

Appendix A.1: Correlation function derivation for a simple pulse.

$$\begin{aligned}
 \chi(\tau, \omega_d) &= \int_{-\infty}^{\infty} \text{Rect}\left(\frac{t}{\tau_p}\right) \text{Rect}\left(\frac{t-\tau}{\tau_p}\right) \exp(j\omega_d t) dt \\
 &= \int_{-\frac{\tau_p}{2}}^{\frac{\tau_p}{2}} \text{Rect}\left(\frac{t-\tau}{\tau_p}\right) \exp(j\omega_d t) dt \\
 &= \begin{cases} \int_{\frac{-\tau_p}{2}}^{\frac{\tau_p}{2}+\tau} \exp(j\omega_d t) dt & ; -\tau_p \leq \tau \leq 0 \\ \int_{\frac{-\tau_p}{2}+\tau}^{\frac{\tau_p}{2}} \exp(j\omega_d t) dt & ; 0 \leq \tau \leq \tau_p \end{cases} \\
 &= \begin{cases} \frac{1}{j\omega_d} \left[\exp(j\omega_d t) \right]_{\frac{-\tau_p}{2}}^{\frac{\tau_p}{2}+\tau} & ; -\tau_p \leq \tau \leq 0 \\ \frac{1}{j\omega_d} \left[\exp(j\omega_d t) \right]_{\frac{-\tau_p}{2}+\tau}^{\frac{\tau_p}{2}} & ; 0 \leq \tau \leq \tau_p \end{cases} \\
 &= \begin{cases} \frac{1}{j\omega_d} \left[\exp\left(\frac{j\omega_d \tau_p}{2}\right) \exp(j\omega_d \tau) - \exp\left(\frac{-j\omega_d \tau_p}{2}\right) \right] & ; -\tau_p \leq \tau \leq 0 \\ \frac{1}{j\omega_d} \left[\exp\left(\frac{j\omega_d \tau_p}{2}\right) - \exp\left(\frac{-j\omega_d \tau_p}{2}\right) \exp(j\omega_d \tau) \right] & ; 0 \leq \tau \leq \tau_p \end{cases}
 \end{aligned}$$

Multiply numerator and denominator by $\exp\left(\frac{-j\omega_d \tau}{2}\right)$ to produce:

$$\chi(\tau, \omega_d) = \begin{cases} \frac{1}{j\omega_d} \exp\left(\frac{j\omega_d \tau}{2}\right) \left[\exp\left(\frac{j\omega_d(\tau_p + \tau)}{2}\right) - \exp\left(\frac{-j\omega_d(\tau_p + \tau)}{2}\right) \right] & ; -\tau_p \leq \tau \leq 0 \\ \frac{1}{j\omega_d} \exp\left(\frac{j\omega_d \tau}{2}\right) \left[\exp\left(\frac{j\omega_d(\tau_p - \tau)}{2}\right) - \exp\left(\frac{-j\omega_d(\tau_p - \tau)}{2}\right) \right] & ; 0 \leq \tau \leq \tau_p \end{cases}$$

Comparing the limits on the right-hand side to the sign of τ , the above relationship can be expressed in term of $|\tau|$:

$$\begin{aligned}
 \chi(\tau, \omega_d) &= \frac{1}{j\omega_d} \exp\left(\frac{j\omega_d \tau}{2}\right) \left[\exp\left(\frac{j\omega_d(\tau_p - |\tau|)}{2}\right) - \exp\left(\frac{-j\omega_d(\tau_p - |\tau|)}{2}\right) \right] \text{rect}\left(\frac{\tau}{2\tau_p}\right) \\
 &= \frac{2}{\omega_d} \exp\left(\frac{j\omega_d \tau}{2}\right) \sin\left(\frac{\omega_d(\tau_p - |\tau|)}{2}\right) \text{rect}\left(\frac{\tau}{2\tau_p}\right) \\
 &= (\tau_p - |\tau|) \exp\left(\frac{j\omega_d \tau}{2}\right) \text{Sinc}\left(\frac{\omega_d(\tau_p - |\tau|)}{2}\right) \text{rect}\left(\frac{\tau}{2\tau_p}\right)
 \end{aligned}$$

Appendix A.2: Correlation function derivation for pulsed linear FM.

$$\chi(\tau, \omega_d) = \int_{-\infty}^{\infty} \text{Rect}\left(\frac{t}{\tau_p}\right) \text{Rect}\left(\frac{t-\tau}{\tau_p}\right) \exp(j\pi\alpha t^2) \exp(-j\pi\alpha(t-\tau)^2) \exp(j\omega_d t) dt$$

$$= \int_{\frac{-\tau_p}{2}}^{\frac{\tau_p}{2}} \text{Rect}\left(\frac{t-\tau}{\tau_p}\right) \exp(j\pi\alpha t^2) \exp(-j\pi\alpha(t-\tau)^2) \exp(j\omega_d t) dt$$

$$= \begin{cases} \int_{\frac{-\tau_p}{2}}^{\frac{\tau_p}{2}+\tau} \exp(j\pi\alpha t^2) \exp(-j\pi\alpha(t-\tau)^2) \exp(j\omega_d t) dt & ; -\tau_p \leq \tau \leq 0 \\ \int_{\frac{-\tau_p}{2}+\tau}^{\frac{\tau_p}{2}} \exp(j\pi\alpha t^2) \exp(-j\pi\alpha(t-\tau)^2) \exp(j\omega_d t) dt & ; 0 \leq \tau \leq \tau_p \end{cases}$$

$$= \begin{cases} \int_{\frac{-\tau_p}{2}}^{\frac{\tau_p}{2}+\tau} \exp j(\pi\alpha t^2 - \pi\alpha(t-\tau)^2 + \omega_d t) dt & ; -\tau_p \leq \tau \leq 0 \\ \int_{\frac{-\tau_p}{2}+\tau}^{\frac{\tau_p}{2}} \exp j(\pi\alpha t^2 - \pi\alpha(t-\tau)^2 + \omega_d t) dt & ; 0 \leq \tau \leq \tau_p \end{cases}$$

$$= \begin{cases} \exp(-j\pi\alpha\tau^2) \int_{\frac{-\tau_p}{2}}^{\frac{\tau_p}{2}+\tau} \exp j(2\pi\alpha t + \omega_d) dt & ; -\tau_p \leq \tau \leq 0 \\ \exp(-j\pi\alpha\tau^2) \int_{\frac{-\tau_p}{2}+\tau}^{\frac{\tau_p}{2}} \exp j(2\pi\alpha t + \omega_d) dt & ; 0 \leq \tau \leq \tau_p \end{cases}$$

$$\begin{aligned}
\chi(\tau, \omega_d) &= \begin{cases} \frac{\exp(-j\pi\alpha\tau^2)}{j(2\pi\alpha\tau + \omega_d)} [\exp j(2\pi\alpha\tau + \omega_d)\tau]^{\frac{\tau_p + \tau}{2}} & ; -\tau_p \leq \tau \leq 0 \\ \frac{\exp(-j\pi\alpha\tau^2)}{j(2\pi\alpha\tau + \omega_d)} [\exp j(2\pi\alpha\tau + \omega_d)\tau]^{\frac{\tau_p}{2}} & ; 0 \leq \tau \leq \tau_p \end{cases} \\
&= \begin{cases} \frac{\beta}{j\gamma} [\exp j\gamma\tau]^{\frac{\tau_p + \tau}{2}} & ; -\tau_p \leq \tau \leq 0 \\ \frac{\beta}{j\gamma} [\exp j\gamma\tau]^{\frac{\tau_p}{2}} & ; 0 \leq \tau \leq \tau_p \end{cases} \\
&= \begin{cases} \frac{\beta}{j\gamma} \left[\exp\left(j\frac{\gamma\tau_p}{2}\right) \exp j\gamma\tau - \exp\left(-j\frac{\gamma\tau_p}{2}\right) \right] & ; -\tau_p \leq \tau \leq 0 \\ \frac{\beta}{j\gamma} \left[\exp\left(j\frac{\gamma\tau_p}{2}\right) - \exp\left(-j\frac{\gamma\tau_p}{2}\right) \exp j\gamma\tau \right] & ; 0 \leq \tau \leq \tau_p \end{cases} \\
&= \begin{cases} \frac{\beta}{j\gamma} \exp\left(j\frac{\gamma\tau}{2}\right) \left[\exp\left(j\frac{\gamma\tau_p}{2}\right) \exp\left(j\frac{\gamma\tau}{2}\right) - \exp\left(-j\frac{\gamma\tau_p}{2}\right) \exp\left(-j\frac{\gamma\tau}{2}\right) \right] & ; -\tau_p \leq \tau \leq 0 \\ \frac{\beta}{j\gamma} \exp\left(j\frac{\gamma\tau}{2}\right) \left[\exp\left(j\frac{\gamma\tau_p}{2}\right) \exp\left(-j\frac{\gamma\tau}{2}\right) - \exp\left(-j\frac{\gamma\tau_p}{2}\right) \exp j\frac{\gamma\tau}{2} \right] & ; 0 \leq \tau \leq \tau_p \end{cases} \\
&= \begin{cases} \frac{\beta}{j\gamma} \exp\left(j\frac{\gamma\tau}{2}\right) \left[\exp\left(j\frac{\gamma(\tau_p + \tau)}{2}\right) - \exp\left(-j\frac{\gamma(\tau_p + \tau)}{2}\right) \right] & ; -\tau_p \leq \tau \leq 0 \\ \frac{\beta}{j\gamma} \exp\left(j\frac{\gamma\tau}{2}\right) \left[\exp\left(j\frac{\gamma(\tau_p - \tau)}{2}\right) - \exp\left(-j\frac{\gamma(\tau_p - \tau)}{2}\right) \right] & ; 0 \leq \tau \leq \tau_p \end{cases} \\
&= \frac{\beta}{j\gamma} \exp\left(j\frac{\gamma\tau}{2}\right) \left[\exp\left(j\frac{\gamma(\tau_p - |\tau|)}{2}\right) - \exp\left(-j\frac{\gamma(\tau_p - |\tau|)}{2}\right) \right] \text{Rect}\left(\frac{\tau}{2\tau_p}\right) \\
&= \frac{2\beta}{\gamma} \exp\left(j\frac{\gamma\tau}{2}\right) \sin\left(\frac{\gamma(\tau_p - |\tau|)}{2}\right) \text{Rect}\left(\frac{\tau}{2\tau_p}\right)
\end{aligned}$$

$$\begin{aligned}
&= (\tau_p - |\tau|) \beta \exp\left(j \frac{\gamma \tau}{2}\right) \text{Sinc}\left(\frac{\gamma(\tau_p - |\tau|)}{2}\right) \text{Rect}\left(\frac{\tau}{2\tau_p}\right) \\
&= (\tau_p - |\tau|) \exp(-j\pi\alpha\tau^2) \exp\left(j \frac{(2\pi\alpha\tau + \omega_d)\tau}{2}\right) \text{Sinc}\left(\frac{(2\pi\alpha\tau + \omega_d)(\tau_p - |\tau|)}{2}\right) \text{Rect}\left(\frac{\tau}{2\tau_p}\right) \\
&= (\tau_p - |\tau|) \exp\left(j \frac{\omega_d \tau}{2}\right) \text{Sinc}\left(\left(\pi\alpha\tau + \frac{\omega_d}{2}\right)(\tau_p - |\tau|)\right) \text{Rect}\left(\frac{\tau}{2\tau_p}\right)
\end{aligned}$$

Appendix B: Device Specifications

Appendix B.1: OXCO Specification

(© 2000 Wenzel Associates, Inc.)

OUTPUT

Frequency

10 MHz

Level

+13 dBm ±2dB into 50 ohms

STABILITY

Aging

1×10^{-6} per day

after 30 days operating, typical

Phase Noise L(f)

10 Hz -130 dBc/Hz

100 Hz -158 dBc/Hz

1 kHz -172 dBc/Hz

10 kHz -172 dBc/Hz

Temperature Stability

$\pm 5 \times 10^{-6}$, 0° to +50°C (Ref +25°C)

MECHANICAL

Dimensions

1.75 x 2.94 x 1"

Connectors

SMA on side and solder pins on base

Packaging

Sealed steel can

POWER REQUIREMENTS

Warm-Up Power

5 Watts for 5 minutes

Total Power

2.5 Watts at +25°C

Supply Voltage

+15 VDC

ADJUSTMENT

Mechanical Tuning

$\pm 1 \times 10^{-6}$

Electrical Tuning

$\pm 2 \times 10^{-7}$, ±5 VDC

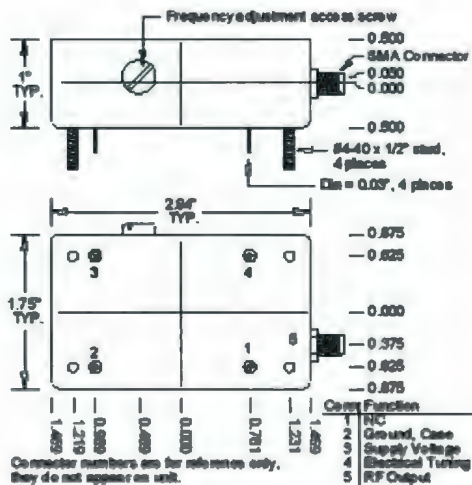
Negative slope

CRYSTAL

Type

10 MHz SC-cut

REV	DATE	REVISION RECORD	DWN	AUTH
-	10-27-95	Draw	BH	
A	09-21-99	Temperature Stability	BH	
B	10-29-99	Tuning Hole	KP	BH
C	09-19-00	Correct ET on Drawing	KP	KW
D	10-11-00	Correct Drawing	KP	KW
E	10-09-00	1 and 10kHz noise	KW	



W Wenzel Associates, Inc. Austin, Texas				
Standard 10 MHz-SC Ultra Low Noise Crystal Osc.				
Part No.	Rev	Date	Drawn	Ref
801-04537	E	10-09-00		
Frequency (actual or stated)	1.000 Dec	1.000 Dec	FORM	Page 1 of 1
Dimensional Tolerance	±0.030"	±0.010"	62821	

Appendix B.2: DDS Specification

(© 2007 Analog Devices, Inc.)



CMOS 300 MSPS Quadrature Complete DDS

AD9854

FEATURES

- 300 MHz internal clock rate
- FSK, BPSK, PSK, chirp, AM operation
- Dual integrated 12-bit digital-to-analog converters (DACs)
- Ultrahigh speed comparator, 3 ps rms jitter
- Excellent dynamic performance
- 80 dB SFDR at 100 MHz (± 1 MHz) A_{out}
- 4x to 20x programmable reference clock multiplier
- Dual 48-bit programmable frequency registers
- Dual 14-bit programmable phase offset registers
- 12-bit programmable amplitude modulation and on/off output shaped keying function
- Single-pin FSK and BPSK data interfaces
- PSK capability via input/output interface
- Linear or nonlinear FM chirp functions with single-pin frequency hold function
- Frequency-ramped FSK
- <25 ps rms total jitter in clock generator mode

- Automatic bidirectional frequency sweeping
- Sin(x)/x correction
- Simplified control interfaces
- 10 MHz serial 2- or 3-wire SPI compatible
- 100 MHz parallel 8-bit programming
- 3.3 V single supply
- Multiple power-down functions
- Single-ended or differential input reference clock
- Small, 80-lead LQFP or TQFP with exposed pad

APPLICATIONS

- Agile, quadrature LO frequency synthesis
- Programmable clock generators
- FM chirp source for radar and scanning systems
- Test and measurement equipment
- Commercial and amateur RF excitors

FUNCTIONAL BLOCK DIAGRAM

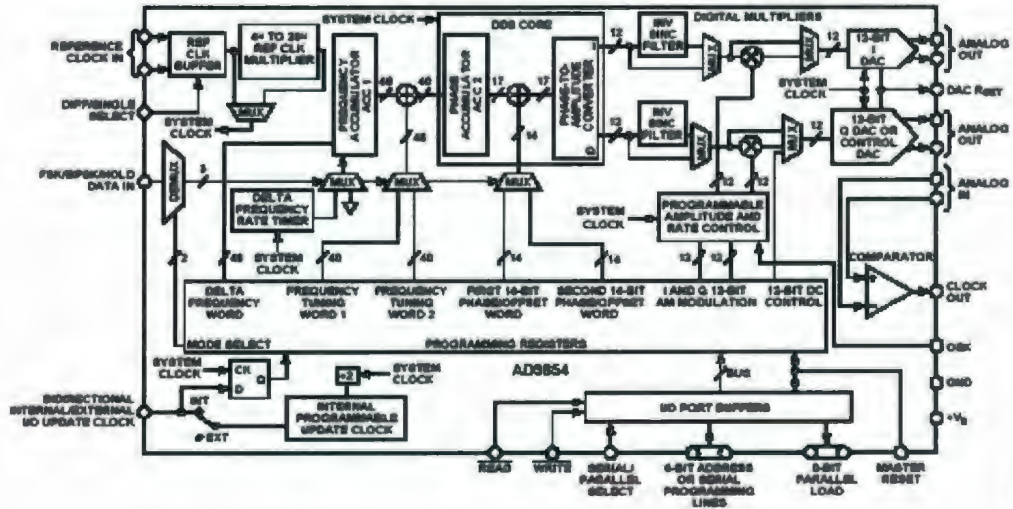


Figure 1.

Rev. E
Information furnished by Analog Devices is believed to be accurate and reliable. However, no responsibility is assumed by Analog Devices for its use, nor for any infringements of patents or other rights of third parties that may result from its use. Specifications subject to change without notice. No license is granted by implication or otherwise under any patent or patent rights of Analog Devices. Trademarks and registered trademarks are the property of their respective owners.

One Technology Way, P.O. Box 9106, Norwood, MA 02062-9104, U.S.A.
Tel: 781.329.4700 www.analog.com
Fax: 781.461.3113 ©2002-2007 Analog Devices, Inc. All rights reserved.





